

Dissertation

**Pilot Pattern Optimization for Doubly-Selective
MIMO OFDM Transmissions**

ausgeführt zum Zwecke der Erlangung des akademischen Grades
eines Doktors der technischen Wissenschaften

eingereicht an der Technischen Universität Wien
Fakultät für Elektrotechnik und Informationstechnik

von

Michal Šimko

geboren am 1. Oktober 1985 in Bratislava
Matrikelnummer: 0425054

Wien, im Mai 2013

1. Advisor:

Univ. Prof. Dr.-Ing. Markus Rupp
Institute of Telecommunications
Vienna University of Technology
Austria

2. Advisor:

Prof. Paulo S. R. Diniz, PhD.
Signal Processing Laboratory
Federal University of Rio de Janeiro
Brazil

I hereby certify that the work reported in this thesis is my own,
and the work done by other authors is appropriately cited.

Michal Šimko
Vienna, May 15, 2013

Abstract

Current wireless transmission systems are far from their theoretically achievable performance bounds. The main reason behind this is a conservative approach of the standardization organizations. Most current standards for wireless communication employ Multiple-Input Multiple-Output (MIMO) Orthogonal Frequency-Division Multiplexing (OFDM) modulation as it offers a high spectral efficiency. These systems require the insertion of at the receiver known symbols in order to estimate the transmission channel. These so-called pilot-symbols consume available resources such as power and bandwidth, and therefore effectively decrease spectral efficiency. This thesis deals with pilot pattern optimization for MIMO OFDM transmission systems.

First, an optimal power distribution among pilot- and data-symbols is considered. The post-equalization Signal to Interference and Noise Ratio (SINR) is maximized in order to deliver optimal performance. The optimal power offset between the pilot- and data-symbols depends on the ratio between the number of pilot- and data-symbols, and on the distinct performance of the utilized channel estimator. The achievable gains by the optimal power distribution depend on the operational point. Throughput gains up to 10% can be achieved.

Furthermore, this thesis proposes a framework for optimal pilot pattern design for MIMO OFDM systems under doubly selective channels. An upper bound of the constrained channel capacity including channel estimation errors is provided. This allows to find an optimal pilot pattern for a given Signal to Noise Ratio (SNR), channel correlation, and channel estimator. Significant throughput gains can be achieved by employing the optimal pilot patterns compared to transmission systems with standardized fixed pilot patterns. The throughput gains can reach up to 850% when comparing with a 4×4 Long Term Evolution (LTE) system.

In this thesis, I propose solutions how to approach the theoretically achievable performance bounds. The proposed solutions can easily be implemented into the future standards for wireless communication, and significantly improve their throughput.

Kurzfassung

Heutige Mobilfunkstandards liegen weit hinter ihren theoretischen Leistungsgrenzen. Der Hauptgrund dafür liegt in der konservativen Vorgangsweise der Standardisierungsorganisationen. Die neuesten Mobilfunkstandards setzen wegen ihrer hohen spektralen Effizienz auf MIMO OFDM Modulation. Solche Systeme erfordern den Einsatz von beim Empfänger bekannter Signale, um den Übertragungskanal zu schätzen. Diese so-genannten Pilotsymbole konsumieren allerdings verfügbare Ressourcen wie Leistung und Bandbreite und vermindern damit die spektrale Effizienz.

Zunächst wird eine optimale Leistungsverteilung zwischen Daten und Pilotsymbolen betrachtet. Das Post-Entzerrer SINR wird maximiert, um optimale Leistungsfähigkeit zu gewährleisten. Der optimale Leistungsabstand zwischen Pilot und Datensymbolen hängt von dem Verhältnis der Pilot und Datensymbole sowie dem Vermögen des verwendeten Kanalschätzers ab. Der durch optimale Leistungsverteilung erreichbare Gewinn hängt vom Arbeitspunkt ab. Durchsatzerhöhungen von 10% können erreicht werden.

Darüberhinaus schlägt die vorliegende Arbeit eine Methodik zur optimalen Gestaltung von Pilotmuster für MIMO OFDM Übertragungen über doppelt selektive Kanäle vor. Eine obere Grenze der bedingten Kanalkapazität, die Kanalschätzfehler mit berücksichtigt, wird angegeben. Dies erlaubt es, optimale Pilotmuster für gegebenes SNR, Kanalkorrelation und Kanalschätzer zu berechnen. In Vergleich zu standardisierten Pilotsequenzen können nun optimale Sequenzen verwendet werden, die signifikante Durchsatzverbesserungen erreichen. Diese Verbesserungen können bis zu 850% groß sein, wenn ein 4×4 LTE System zugrunde gelegt wird.

In der vorliegenden Arbeit schlage ich Lösungen vor, die theoretisch erreichbare Grenzen annähern. Die vorgeschlagenen Lösungen lassen sich leicht in zukünftige Standards einbauen und erhöhen den Datendurchsatz signifikant.

Acknowledgements

I owe my deepest gratitude to my supervisor Markus Rupp. His trust, support, and the freedom he gave me have been essential for the creation of this work.

I am equally grateful to Paulo S. R. Diniz for all the support and a great deal of input I have received, as well as for his hospitality and friendliness during my stay at UFRJ in Brazil.

Christoph F. Mecklenbräuer deserves a special mention. Thank you for asking simple questions.

This dissertation would not have been possible without the financial support of the Christian Doppler Gesellschaft. I would like to express my gratitude especially towards A1 Telekom Austria AG and KATHREIN-Werke KG.

Special thanks belong to people who have stayed in the MIMO lab during my studies. Thank you Sebastian for introducing me to the group. Thank you Christian for the guidance at the beginning of my studies. Thank you Qi for always listening to my endless questions. Thank you Josep for making the MIMO lab a nicer place to work at.

I will always be grateful to people I met during my research stays in Sweden and in Brazil, who shared their time with me. Thank you Dan, Michaela, Andi, Maria, Megan, and Rachel.

I also owe a great debt of gratitude to my friend Martin, who has always been there for me. Thank you for your support and time. I would like to show my gratitude to Cyril. Thank you for standing close to my family when most needed. I am truly indebted and thankful to Michal, who has always been there to encourage me, Maria who has always been ready to listen, and Miška for all her creative inspirations. I owe my sincere and earnest thankfulness to my grandfather Daniel, who has been the biggest fan and supporter of my research.

Lastly, and most importantly, I would like to thank my parents, especially my mom. Without them I just would not be the person I am. Thank you for everything.

Contents

1	Introduction	1
1.1	Motivation	2
1.2	Scope of the Work	2
1.3	Chapter Overview	4
1.4	Related Publications	5
2	Link Level Simulation Methodology	7
2.1	UMTS Long Term Evolution	7
2.1.1	Multicarrier Technology	8
2.1.2	Multiple Antenna Technology	11
2.2	Vienna Long Term Evolution Simulator	15
2.2.1	Structure	17
2.2.2	Complexity	20
2.3	Transmission Model	21
2.4	Summary	23
3	Receiver Performance Modeling	25
3.1	Channel Estimation	25
3.1.1	Least Squares Channel Estimation	26
3.1.2	Linear Minimum Mean Squared Error Channel Estimation	31
3.1.3	Intercarrier-Interference Estimation	34
3.2	Post-equalization SINR	38
3.3	Summary	42
4	Pilot-Symbol Power Allocation	45

4.1	Optimal Power Allocation	46
4.2	Power Efficient Power Allocation	52
4.3	Summary	59
5	Optimal Pilot-Symbol Pattern Design	63
5.1	Optimal Pilot-Symbol Patterns	64
5.1.1	Unit Power Distribution	70
5.1.2	Optimal Power Distribution	79
5.2	Adaptive Pilot-Symbol Patterns	93
5.3	Summary	97
6	Summary	99
6.1	Contributions	99
6.2	Outlook	100
A	Interpolation Error Lower Bound	103
B	Two-Dimensional Linear Interpolation	105
C	MSE Parameter Approximation for LMMSE	107
D	ZF Post-equalization SINR	109
E	Constrained Capacity Upper Bound	113
F	AWGN-equivalent SNR Definition	115
	Acronyms	117
	Bibliography	121

1 Introduction

Communication, as exchange of information, is one of the pillars of humanity. People not only need to communicate in order to perform basic tasks, but they also desire to communicate as an expression of their social nature. Independent of the motivation and the form, undoubtedly, communication is an inseparable part of our daily life.

From a technological point of view, a personal, face to face communication can be classified as the simplest way to convey information from one point to another. As people required to extend the communications distance, they came up with simple signalling methods such as fires, smoke signals, and horns. These methods enabled to extend the distance, however, the message content was strongly limited. Mail and pigeon post allowed to extend the message content and even further extend the distance between the communication participants at the cost of losing the possibility of a real-time interaction. It was the electric telegraph that first allowed to transmit, with help of the Morse code, information from one point to another with a small delay. The telegraph required to build a wired infrastructure. From a communication point of view, the next step came less than four decades later, a telephone; a device that allowed a real-time human voice interaction over long distances. As in the case of the telegraph, a wire infrastructure was required.

The next step in the evolution of communications, was brought by famous Nikola Tesla, who demonstrated a wireless telegraph [1]. This invention was soon followed by the radio that allowed to transmit sound over the air. Typically, this type of communication was only from one point to another, therefore not allowing for any interaction. Not long after, the first mobile telephone systems were introduced beginning with a simple analog transmission of voice, soon followed by digital transmission of various types of information not being limited only to voice data.

Today, technology further extends the communication distance, extends the com-

munication participants from people to machines, and modifies the communication media.

1.1 Motivation

In the past decades, wireless communication has literally revolutionized the way we communicate. What may have looked like a dream couple of years ago, has recently become daily reality, beginning with voice services, ending with wireless broadband connections. The amount of data transmitted via air has been growing and it is expected to keep the trend. According to the latest report by Ericsson [2], wireless data traffic is doubling every year (see Figure 1.1). Such a high demand imposes a huge burden especially on researchers and engineers, who have an unenviable responsibility to come up with enabling technologies. In order to convey the desired

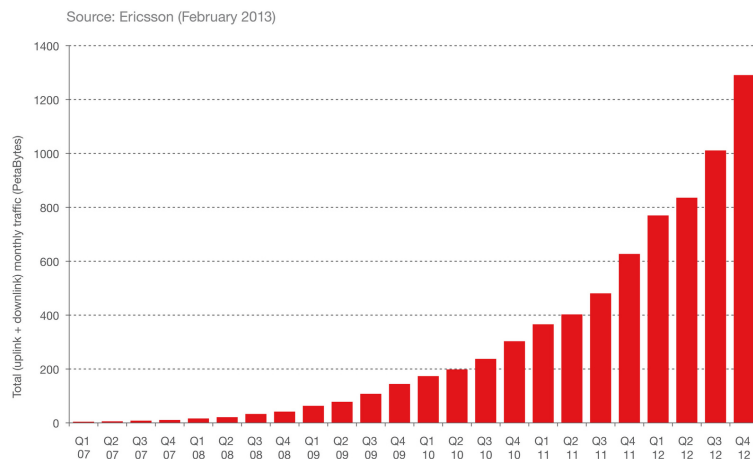


Figure 1.1: Wireless data traffic growth: the traffic is approximately doubling every year. The rapid growth is expected to continue even further. One PetaByte corresponds to 10^{15} Bytes.

amount of information wirelessly, only limited resources are available. Naturally, it is desired to utilize these resources in the most efficient way. Because otherwise the availability of the communication might suffer or a cost boost might occur.

1.2 Scope of the Work

This thesis deals with coherent wireless transmission systems, as it is currently the most utilized transmission technology. In coherent transmission systems, in order to successfully detect the transmitted data-symbols, the transmission channel needs to be estimated. Different types of approaches exist, such as pilot-assisted channel estimation, blind channel estimation, and semi-blind channel estimation. Mainly due

to its high performance and low complexity, the pilot-assisted approach dominates as the chosen approach in the current standards for wireless communication.

However, pilot-assisted channel estimation requires insertion of, at the receiver known, reference symbols, so-called pilot-symbols, that cannot be utilized for data transmission. Thus, pilot-assisted channel estimation decreases spectral efficiency by occupying a portion of the transmission bandwidth by the pilot-symbols. Additionally, these pilot-symbols consume available transmission power and therefore effectively decrease transmission power available for the data-symbols.

The purpose of this thesis is to provide a general framework for pilot-symbol pattern optimization for Multiple-Input Multiple-Output (MIMO) Orthogonal Frequency-Division Multiplexing (OFDM) transmission systems under the general case of doubly-selective channels. In particular, I investigate an optimal power distribution among pilot- and data-symbols and the influence of such a power distribution on the performance of the transmission system. Further, I study optimal pilot-symbol placement within the time-frequency grid as a function of Signal to Noise Ratio (SNR) and channel correlation, and examine the performance improvement when designing the pilot-symbol patterns in an optimal manner. The topic of interest in this thesis is of high importance for wireless communications in general but in order to stress the gravity of the considered scope, let me name a couple current applications:

- car to car communications,
- high speed train communications,
- underwater communications,
- wireless broadband internet,
- machine to machine communications.

The first three applications have in common a highly time-variant channel. A recent standard designed to cope also with highly time-variant channels is called Long Term Evolution (LTE), defined by 3rd Generation Partnership Project (3GPP). This standard intends to support users moving with velocities up to 500 km/h. Although LTE brought a revolution into wireless communications, further improvements are required in order to perfect wireless communications under time-variant channels.

The last two provided applications are intended for rather low mobility scenarios, but due to multi-path propagation, systems applied in such scenarios have to be able to cope with frequency-selective channels. OFDM as widely utilized modulation technique outperforms other modulation techniques experiencing frequency-selective channels. However, the standardization organizations, typically, provide overdimensioned pilot patterns in order to support a wide range of operation at the cost of performance limitation.

It seems natural that the wireless data connection provides the same quality either at home or on the move. With improving technology, also the range of applications and use scenarios of wireless communications widens, which naturally requires further improvement of mobile technologies.

1.3 Chapter Overview

This thesis is structured as follows:

In Chapter 2, I describe the physical layer of an LTE downlink transmission. In the description, the focus lies on the main enabling technologies such as OFDM and MIMO transmission. Furthermore, the simulation tool, the Vienna LTE simulator, is introduced and its principal parts are explained. In the same chapter, I give a mathematical model of a generic MIMO OFDM transmission system that is used throughout this thesis.

In Chapter 3, I derive analytical models for the performance of an MIMO OFDM receiver. The focus lies on the channel estimation, Intercarrier Interference (ICI) modeling, and linear equalization. I derive the Mean Squared Error (MSE) of a general linear channel estimator. The MSE can be divided into a noise-dependent and a noise-independent part. Furthermore, I introduce the concept of a Basis Expansion Model (BEM) for ICI modeling including Discrete Prolate Spheroidal (DPS) and orthogonalized polynomials. Last but not least, I derive the post-equalization Signal to Interference and Noise Ratio (SINR) of a Zero Forcing (ZF) equalizer including channel estimation errors.

Chapter 4 deals with optimal power allocation among pilot- and data-symbols. In the first section of the chapter, I concentrate on the case when the whole available power is consumed for the transmission. In this case, the optimal solution is obtained via maximization of the post-equalization SINR including channel estimation errors. In the second section, I investigate a power efficient solution of the power allocation problem. In that case, instead of maximizing the post-equalization SINR, I rather minimize the transmission power while constraining the post-equalization SINR.

In Chapter 5, I investigate an optimal pilot-symbol design for doubly-selective channels. In the first step of the analysis, I consider solely the pilot-symbol design. In the next step, I also include optimal power distribution into the presented optimal pilot-symbol framework. For the mentioned optimization problems, I utilize an upper bound of the constrained channel capacity as the cost function. Last, but not least, I introduce a concept of adaptive pilot-symbol patterns that are adjusting to varying channel conditions. By utilizing such adaptive pilot patterns, considerable gains of the system performance can be achieved.

Chapter 6 provides a summary of the main contributions of this thesis.

In Appendix A is shown that the interpolation error is always positive. Appendix B shows how to obtain interpolation weights following a two-dimensional linear interpolation strategy. Appendix C shows how to obtain an approximation for the MSE of the Linear Minimum Mean Squared Error (LMMSE) channel estimator. In Appendix D and Appendix E, post-equalization SINR for a ZF equalizer and an upper bound of the constrained capacity are derived, respectively. Last but not least, Appendix F explains Additive White Gaussian Noise (AWGN) equivalent SNR.

1.4 Related Publications

The content of this thesis is to some extent based on the following peer-reviewed publications:

- [1] C. Mehlführer, J. C. Ikuno, M. Šimko, S. Schwarz, M. Wrulich, and M. Rupp, “**The Vienna LTE Simulators - Enabling Reproducibility in Wireless Communications Research,**” *EURASIP Journal on Advances in Signal Processing*, July 2011.
- [2] M. Šimko, Q. Wang, and M. Rupp, “**Optimal Pilot Symbol Power Allocation under Time-Variant Channels,**” *EURASIP Journal on Wireless Communications and Networking*, July 2012.
- [3] S. Schwarz, J. C. Ikuno, M. Šimko, M. Taranetz, Q. Wang, and M. Rupp, “**Pushing the Limits of LTE: A Survey on Research Enhancing the Standard,**” *IEEE Access*, 2013.
- [4] M. Šimko, P. S.R. Diniz, Q. Wang, and M. Rupp, “**Adaptive Pilot-Symbol Patterns for MIMO OFDM Systems,**” *IEEE Transactions on Wireless Communications*, 2013.
- [5] M. Šimko, C. Mehlführer, M. Wrulich, and M. Rupp “**Doubly Dispersive Channel Estimation with Scalable Complexity,**” in Proc. of *International ITG Workshop on Smart Antennas (WSA 2010)*, Bremen, Germany, Feb. 2010.
- [6] M. Šimko, D. Wu, C. Mehlführer, J. Eilert, and D. Liu “**Implementation Aspects of Channel Estimation for 3GPP LTE Terminals,**” in Proc. of *17th European Wireless Conference (EW2011)*, Vienna, Austria, Apr. 2011.
- [7] J. C. Ikuno, S. Schwarz, and M. Šimko, “**LTE Rate Matching Performance with Code Block Balancing,**” in Proc. of *17th European Wireless Conference (EW2011)*, Vienna, Austria, Apr. 2011.
- [8] M. Šimko, C. Mehlführer, T. Zemen, and M. Rupp “**Inter-Carrier Interference Estimation in MIMO OFDM Systems with Arbitrary Pilot Structure,**” in Proc. of *73rd IEEE Vehicular Technology Conference (VTC 2011-Spring)*, Budapest, Hungary, May 2011.
- [9] S. Schwarz, M. Šimko, and M. Rupp “**On Performance Bounds for MIMO OFDM Based Wireless Communication Systems,**” in Proc. of *IEEE Workshop on Signal*

- Processing Advances in Wireless Communications (SPAWC 2011)*, San Francisco, California, USA, June 2011.
- [10] M. Šimko, S. Pendl, S. Schwarz, Q. Wang, J. C. Ikuno, and M. Rupp, “**Optimal Pilot Symbol Power Allocation in LTE**,” in Proc. of *IEEE 74th Vehicular Technology Conference (VTC2011-Fall)*, San Francisco, California, USA, Sep. 2011.
- [11] Q. Wang, M. Šimko, and M. Rupp, “**Modified Symbol Timing Offset Estimation for OFDM over Frequency Selective Channels**,” in Proc. of *IEEE 74th Vehicular Technology Conference (VTC2011-Fall)*, San Francisco, California, USA, Sep. 2011.
- [12] M. Šimko and M. Rupp, “**Optimal Pilot Symbol Power Allocation in Multi-Cell Scenarios of LTE**,” in Proc. of *Forty-fifth Asilomar Conference on Signals, Systems and Computers*, Pacific Grove, California, USA, Nov. 2011.
- [13] Q. Wang, M. Šimko, and M. Rupp, “**Performance Analysis of LTE Downlink under Symbol Timing Offset**,” in Proc. of *16th International ITG Workshop on Smart Antennas (WSA2012)*, Dresden, Germany, Mar. 2012.
- [14] J. C. Ikuno, S. Pendl, M. Šimko, and M. Rupp, “**Accurate SINR Estimation Model for System Level Simulation of LTE Networks**,” in Proc. of *IEEE International Conference on Communications (ICC 2012)*, Ottawa, Canada, June 2012.
- [15] M. Šimko, P. S.R. Diniz, Q. Wang, and M. Rupp, “**Power Efficient Pilot Symbol Power Allocation under Time-Variant Channels**,” in Proc. of *IEEE 76th Vehicular Technology Conference (VTC2012-Fall)*, Quebec, Canada, Sep. 2012.
- [16] M. Šimko, Q. Wang, P. S.R. Diniz, and M. Rupp, “**Inter-Carrier Interference Mitigation by Means of Precoding**,” in Proc. of *IX. International symposium on Telecommunications (BIHTEL 2012)*, Sarajevo, Bosnia and Herzegovina, Oct. 2012.
- [17] M. Meidlinger, M. Šimko, Q. Wang, and M. Rupp, “**Channel Estimators for LTE-A Downlink Fast Fading Channels**,” in Proc. of *17th International ITG Workshop on Smart Antennas 2013 (WSA 2013)*, Stuttgart, Germany, Mar. 2013.
- [18] F. Kadrija, M. Šimko, and M. Rupp, “**Iterative Channel Estimation in LTE Systems**,” in Proc. of *17th International ITG Workshop on Smart Antennas 2013 (WSA 2013)*, Stuttgart, Germany, Mar. 2013.
- [19] M. Šimko, P. S.R. Diniz, Q. Wang, and M. Rupp, “**New Insights in Optimal Pilot Symbol Patterns for OFDM Systems**,” in Proc. of *IEEE Wireless Communications and Networking Conference (WCNC 2013)*, Shanghai, China, Apr. 2013.
- [20] M. Šimko, Q. Wang, and M. Rupp, “**Optimal Pilot Pattern for Time Variant Channels**,” in Proc. of *IEEE International Conference on Communications (ICC 2013)*, Budapest, Hungary, June 2013.
- [21] M. Šimko, P. S.R. Diniz, Q. Wang, and M. Rupp, “**Design Requirements of Adaptive Pilot-Symbol Patterns**,” in Proc. of *ICC Workshop: Beyond LTE-A*, Budapest, Hungary, June 2013.

2 Link Level Simulation Methodology

This chapter describes all for this thesis relevant aspects of the UMTS Long Term Evolution (LTE) standard and explains Multiple-Input Multiple-Output (MIMO) Orthogonal Frequency-Division Multiplexing (OFDM) systems in general, highlighting the concepts utilized in this thesis. In order to show how the proposed optimizations perform in a standardized transmission system, I use exemplarily an LTE transmission system as it is currently being deployed in many countries. Furthermore, this chapter describes a simulation tool utilized during this work, namely the Vienna LTE Simulator. Last but not least, a mathematical description of the MIMO OFDM transmission model, that is applied throughout this thesis, is defined.

2.1 UMTS Long Term Evolution

Cell phones and cell phone based services have become parts of our daily lives. The users require faster and more reliable mobile wireless connections. LTE is one of the latest steps enabling the demand for services. LTE represents a standard from the so called fourth generation (4G) family.

The first generation of mobile wireless standards includes many different systems like Nordic Mobile Telephone (NMT), Total Access Communication System (TACS), Analogue Mobile Phone System (AMPS), and many others [3]. All these standards have one main feature in common, all of them are analog transmission systems. A big step from the first to the second generation lies in a transition from analog to digital communication. Global System for Mobile communications (GSM) as an example of the second generation family, was a very successful technology, the number of devices was rapidly growing and usage of cell phones was becoming part of our daily routine. The huge success of GSM was due to a collaborative spirit

during the development phase that resulted in a robust, interoperable and widely-accepted standard [3]. The demand for a faster wireless communication standard resulted in the definition of Universal Mobile Telecommunications System (UMTS) that represents the third generation. The main aspects of the third generation is the utilization of a larger bandwidth and the utilization of the transmission technology Wideband Code-Division Multiple Access (WCDMA).

In order to ensure the competitiveness of the fourth generation standard during a time-frame of 10 years, the standardization organization 3rd Generation Partnership Project (3GPP) defined the following requirements [3]:

- Reduced delays, in terms of connection establishment and transmission latency
- Increased user data rates
- Improved cell-edge performance
- Improved spectral efficiency
- Simplified network architecture
- Seamless mobility
- Reasonable power consumption for the mobile terminals.

In terms of user mobility, LTE systems are required to support communication with users moving at a speed of up to 350 km/h, and even up to 500 km/h depending on the frequency band.

In order to enable the standard to fulfil all above mentioned requirements, new technologies had to be utilized. From a physical layer perspective, the key technology employed by LTE is the multicarrier transmission scheme OFDM in combination with an extensive usage of multiple antennas at the transmitter and at the receiver, properly modelled as an MIMO system.

2.1.1 Multicarrier Technology

The choice of modulation and multiple-access techniques is crucial for the overall system performance. The standardization organization 3GPP for this purpose employed OFDM that divides the transmission bandwidth into a number of parallel orthogonal but overlapping channels with a smaller bandwidth, an illustrative example of which is provided in Figure 2.1. Such an approach is beneficial, since a frequency selective channel is subdivided into a number of frequency flat channels. This allows a very simple equalization of the channel at the receiver, and since no guard bands are necessary much higher spectral efficiency is achieved by employing OFDM as compared to other modulation techniques.

It was in 1966, when researchers at Bell Labs filed their first OFDM patent [4]. In 1973, Weinstein and Ebert proposed to use a Discrete Fourier Transform (DFT)

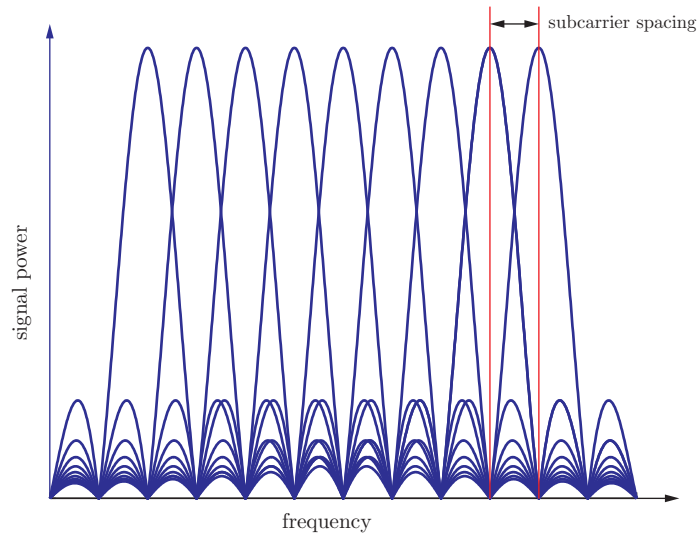


Figure 2.1: OFDM spectrum: the required transmission bandwidth is divided into a number of orthogonal and overlapping subbands with smaller bandwidth.

and guard bands, which allowed to implement the modulation technique in a cost-effective way [5]. Further cost reduction in implementation was brought by the Fast Fourier Transform (FFT) [6]. During the last decade OFDM was utilized by several transmission standards, e.g., Digital Audio Broadcasting (DAB), Digital Video Broadcasting (DVB), and Wireless Local Area Network (WLAN).

From a physical layer point of view, the benefits of OFDM can be summarized into the following points [3]:

- Simple equalization at the receiver
- Easy implementation of MIMO schemes
- Orthogonality between subchannels that results in high spectral efficiency

However, OFDM utilization is connected with the following drawbacks:

- High Peak-to-Average Power Ratio (PAPR) requiring highly linear power amplifiers
- Sensitivity to frequency offset
- Loss of orthogonality between subcarriers when experiencing time-variant channels
- Large guard-bands required to separate different OFDM signals

Let me consider a simple OFDM system, an illustrative example of a transmitter is provided in Figure 2.2. In complex baseband notation, OFDM signal in the time

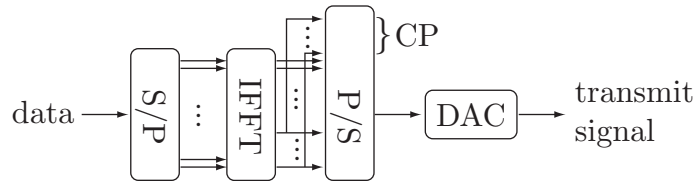


Figure 2.2: OFDM transmitter: the transmit data is (after serial to parallel conversion) transformed into the time domain via IFFT, then the CP prefix is attached and after parallel to serial conversion and conversion to analog signals, the final transmit signal is available.

domain can be expressed as

$$x[n] = \frac{1}{\sqrt{N}} \sum_{m=0}^{N-1} X[m] e^{j2\pi m \frac{n}{N}} \quad 0 \leq n \leq N-1, \quad (2.1)$$

where N denotes the number of subcarriers and $X[m]$ represents the data-symbol at the m -th subcarrier. First, data-symbols in the frequency domain are transformed via Inverse Fast Fourier Transform (IFFT) into the time domain following Equation (2.1). Afterwards, the N_{CP} last samples are attached at the beginning of the OFDM symbol as demonstrated in Figure 2.2. This part of the signal is called Cyclic Prefix (CP) and its purpose is to avoid Inter-Symbol Interference (ISI) between consecutive OFDM symbols. At the receiver side, the procedures of the receiver are reversed, the CP is removed and the FFT is performed in order to transform the received signal back into the frequency domain. Under the assumption that the CP is at least as long as the channel impulse response and that the channel is not significantly changing over the duration of an OFDM symbol, the overall system can be expressed as

$$Y[m] = H[m] X[m] + N[m], \quad (2.2)$$

where $Y[m]$ denotes the received symbol in the frequency domain located at the m -th subcarrier, $H[m]$ is the complex channel coefficient that can be obtained via the Fourier transformation of the channel impulse response and $N[m]$ represents additive noise.

The physical layer of LTE is defined in [7–9]. The standard is defined in such a way that a wide range of scenarios is supported, from indoor urban up to rural situations under low and high mobility [3]. In the time domain, the LTE downlink signal consists of frames with a duration of 10 ms. Each frame is split into ten equally long subframes and each subframe into two equally long slots with a duration of

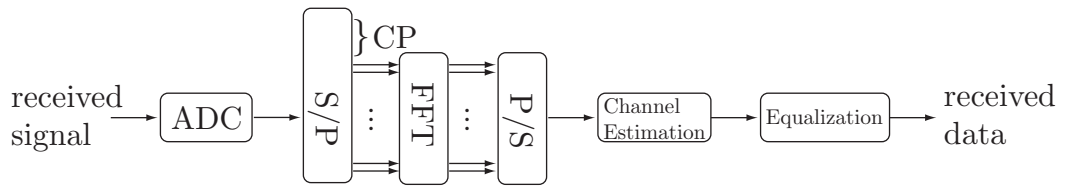


Figure 2.3: OFDM receiver: after the conversion of the received signal into the digital domain and removal of the CP, the signal is transformed into the frequency domain via FFT. Then procedures like channel estimation and equalization are performed to remove the effects of the channel.

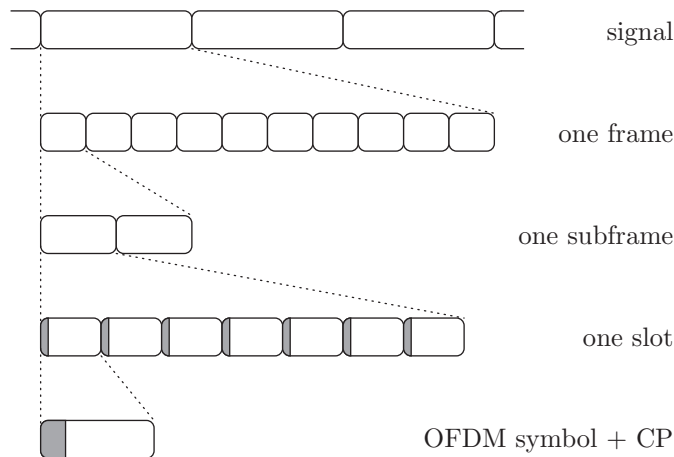


Figure 2.4: LTE signal structure: one frame has a duration of 10 ms. Each frame consists of 10 subframes, comprising 14 OFDM symbols each.

0.5 ms. With the normal cyclic prefix length, each slot consists of seven OFDM symbols; and for the extended cyclic prefix length of six OFDM symbols. In case of the normal cyclic prefix length, its duration is around $5 \mu\text{s}$, with the extended cyclic prefix length, it is $17 \mu\text{s}$. In LTE, the subcarrier spacing is fixed at 15 kHz. Twelve adjacent subcarriers in one slot are grouped into a so-called resource block. The number of resource blocks in an LTE slot ranges from 6 up to 100, corresponding to a bandwidth from 1.4 MHz up to 20 MHz; for all possibilities refer to Table 2.1.

2.1.2 Multiple Antenna Technology

Multiple antenna technology can be regarded as a set of techniques that rely on the use of multiple antennas at the receiver and/or the transmitter in combination with signal processing [10]. Its value as means to improve communications was recognized

Table 2.1: LTE bandwidth: the bandwidth utilized by LTE ranges from 1.4 MHz up to 20 MHz, corresponding to the number of data subcarriers ranging from 72 up to 1200.

Channel bandwidth [MHz]	1.4	3	5	10	15	20
Number of resource blocks	6	15	25	50	75	100
Number of subcarriers	72	180	300	600	900	1 200
FFT size	128	256	512	1 024	1 536	2 048

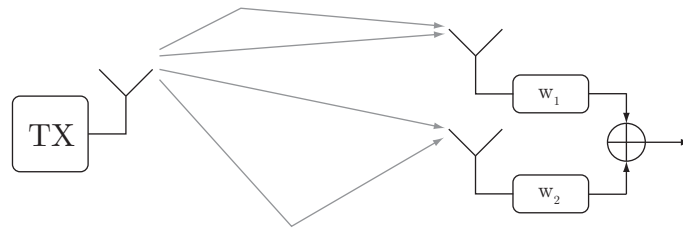


Figure 2.5: Receive diversity: the receiver is equipped with two antennas that help to improve the reliability of the transmission system.

in the very early ages of wireless transmissions [3]. A first military application can be traced back to almost 60 years ago, however in the mass market multiple antenna techniques drew attention first around the year 2000 [11].

The availability of multiple antennas opens door to three types of gains [3]:

- Diversity gain: improved ability to mitigate the effect of multipath fading by transmitting or receiving over multiple antennas at which the effect of fading is decorrelated.
- Array gain: corresponds to power gain achieved by "shaping" the overall antenna beam (beamforming).
- Multiplexing gain: refers to the ability to transmit more data streams in parallel and by doing so increase the spectral efficiency.

Historically most commonly used are multiple antennas at the receiver side, an example is shown in Figure 2.5. This multiple antenna setup is often referred to as receiver diversity [10]. At the receiver side, signals from the individual receive antennas are linearly combined. One possible strategy to combine the signals is Maximum Ratio Combining (MRC), where the phase of the signals is rotated to ensure that the signals are phase aligned and weighted in proportion to the corresponding channel gains. It results in a maximal Signal to Noise Ratio (SNR).

As an alternative to multiple receive antennas, multiple antennas at the transmitter side can be employed. Multiple transmit antennas can be used to achieve diversity and beam-forming [10]. Additionally, multiple transmit antennas shift hardware complexity from the receiver to the transmitter side, which is beneficial in systems

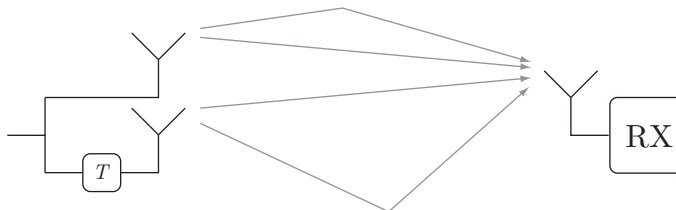


Figure 2.6: Transmit diversity: the simplest example of transmit diversity, the signal of one transmit antenna is delayed by time T compared to the other antenna. Such an approach is called delay diversity.

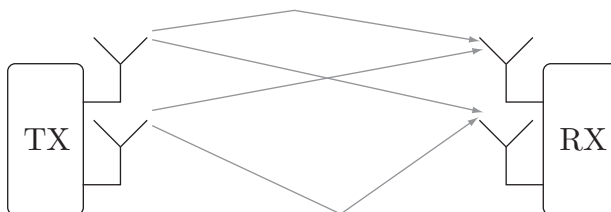


Figure 2.7: Spatial multiplexing: the technique to increase spectral efficiency by applying multiple antennas at the transmit and receiver side and transmitting data packets in parallel.

where low complexity receivers are desired. If no channel knowledge is available at the receiver, beam-forming cannot be achieved, only diversity can be utilized. The simplest example of diversity achievable by employing multiple transmit antennas is delay diversity, where both of the transmit antennas transmit the same signal, but the signal from one transmit antenna is delayed compared to the other antenna. An example is shown in Figure 2.6. A very popular technique to achieve transmit diversity is by the application of space-time block codes [10].

The application of multiple antennas at the transmitter and receiver side at the same time, allows to achieve the above mentioned transmit and receive diversity simultaneously. Additionally to these, there is also the possibility for so-called spatial multiplexing. The most important requirement for achieving a multiplexing gain is that the channels between various transmit and receive antennas are sufficiently uncorrelated [3]. An example of such a system is depicted in Figure 2.7.

LTE defines a transmit diversity scheme for two and four transmit antennas [7]. Transmit diversity is usually applied at low SNRs and in low mobility scenarios [3]. The transmit diversity mode utilizes Space-Frequency Block Codes (SFBCs). Another transmit diversity technique applied in LTE is Cyclic Delay Diversity (CDD). This technique is however not used alone, but in combination with spatial multiplexing. The basic principle of CDD is the same as in the above described time-delay diversity. More details on both diversity techniques can be found in [3].

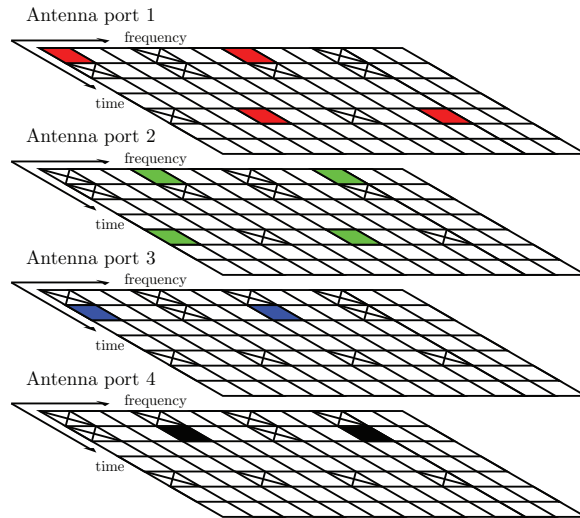


Figure 2.8: LTE pilot-symbol patterns: the colored squares correspond to pilot-symbols located in the time-frequency grid of the LTE signal at different antennas. Crossed squares correspond to silent positions within the time-frequency grid. This ensures that the pilot-symbols are orthogonal between individual antennas.

In LTE two types of spatial multiplexing are defined [7]:

- Open-loop: in this type of spatial multiplexing, the precoding matrix is circularly varied among the defined precoding matrices.
- Closed-loop: the precoding matrix is chosen from a set of predefined precoding matrices based on feedback information sent by the User Equipment (UE).

In order to cope with channel distortions, channel state information has to be obtained at the receiver side. For this purpose the LTE standard defines pilot-symbol patterns distributed over various antennas. Figure 2.8 displays the pilot-symbol pattern in LTE for four transmit antennas. The colored squares correspond to pilot-symbols. If there is a pilot-symbol inserted at a specific position in the time-frequency grid at one transmit antenna, the remaining antennas on the same position remain silent. In Figure 2.8, crosses correspond to these silent positions. The pilot patterns located on the different transmit antennas are orthogonal to each other, i.e., the transmitted pilot-symbols at a specific antenna are not disturbed from the signal transmitted at the remaining antennas. Such a pilot-symbol pattern allows to estimate an MIMO channel as a set of individual Single-Input Single-Output (SISO) channels as long as their spatial correlation is neglected. If for example only a single transmit antenna is utilized, only pilot-symbols at the first antenna are transmitted (red squares) and no positions are kept silent. Table 2.2 shows the amount of resources that are occupied by pilot-symbols using various numbers of transmit antennas.

Table 2.2: Relative pilot-symbol overhead: with an increasing number of transmit antennas, also the overhead necessary for channel estimation is increasing.

number of transmit antennas	pilot-symbol overhead [%]
1	$\approx 4,7$
2	$\approx 9,5$
4	$\approx 14,3$

2.2 Vienna Long Term Evolution Simulator

In this section, the simulation tool utilized in this thesis is introduced and its structure is explained. Furthermore, the motivation for development of such an advanced tool is provided. In 2009, at the Vienna University of Technology, a team of researchers started to implement a first version of an LTE compliant MATLAB and C based link level simulator. First results were published in [12]. With time the group around the LTE simulator grew and so did the simulator’s functionality. Around time of publishing [13], the simulator was termed Vienna LTE simulator. Its functionality was extended towards newer LTE-Advanced (LTE-A) standards as well as system level and LTE uplink. The simulator is freely available for download under an ”academic non-commercial use licence”. Until now (April 2013), the Vienna LTE link level simulator was downloaded more than 23 000 times from all over the world.

The motivation behind the development of the Vienna LTE simulator can be described by two keywords:

- Reproducibility
- Openness

Reproducibility is one of the pillars of scientific research. Whereas reproducibility has a long tradition in most nature sciences and theoretical sciences, such as mathematics, it is only recently that reproducible research becomes more and more important in the field of signal processing [14, 15]. In contrast to results in fields of purely theoretical sciences, results of signal processing research papers can only be reproduced if a comprehensive description of the investigated algorithms (including the setting of all necessary parameters), and eventually the required input data are fully available. Due to lack of space, a fully comprehensive description of the algorithm is often omitted in research papers. Even if an algorithm is explained in detail, for instance by a pseudo code, initialization values are frequently not fully defined. Moreover, it is not possible to include in a paper all necessary resources, such as data that was processed by the presented algorithms. Ideally, all resources, including the source code of the presented algorithms, should be made available for download to enable other researchers (and also reviewers of papers) to reproduce the results presented. Unfortunately, a researcher’s reality does not resemble this ideal

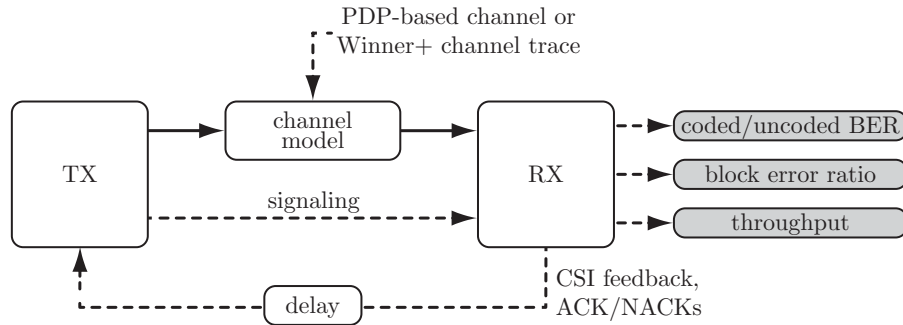


Figure 2.9: Structure of the Vienna LTE simulator: the simulator is comprised by one or more transmitter blocks, channel modeling for each link, and receiver blocks. The feedback channel is implemented as a delayed error-free signaling channel.

situation, a circumstance that has recently been complained about quite openly [16].

Therefore, the authors of the simulator decided to offer the source code of the simulator under a so called "academic non-commercial use license", allowing the research community to reproduce the published results. By doing so, not only they enabled their research results to be confronted by the research community around the world, but they also provided a platform that allows researchers from other groups to implement their algorithms which can be further tested.

The link level simulator can be divided into three basic building blocks, namely *transmitter*, *channel model*, and *receiver* (see Figure 2.9). Depending on the type of simulation, one or several instances of these basic building blocks are employed. The transmitter and receiver blocks are linked by the channel model, which is used to transmit the downlink data, while signaling and uplink feedback is assumed to be error-free. Since signaling is stronger protected than data, by means of lower coding rates and/or lower-order modulations, the assumption of error-free signaling is in fact quite realistic. Equivalently, errors on the signaling channels only occur when the data channels are already facing substantial performance degradation — a point of operation usually not targeted in investigations.

In the downlink, the signaling information passed on by the transmitter to the receiver contains coding, HARQ, scheduling, and precoding parameters. In the uplink, Channel Quality Indicator (CQI), Precoding Matrix Indicator (PMI), and Rank Indicator (RI) (all three together forming the Channel State Information (CSI)) are signaled. All simulation scenarios (see Section 2.2.2) support the feedback of CQI, PMI, and RI, although it is also possible to set some or all of them to fixed values. Such a setting is required for specific simulations, such as throughput evaluation of an individual Modulation and Coding Scheme (MCS).

2.2.1 Structure

In the following, the structure of the Vienna LTE simulator is described.

Transmitter

The layout of the LTE downlink transmitter is shown in Figure 2.10. This structure is basically a graphical representation of the transmitter description defined in the TS36' standard series [7–9]. Based on UE feedback values, a scheduling algorithm assigns Resource Blocks (RBs) to UEs and sets an appropriate MCS (coding rates between 0.076 and 0.926 with 4, 16, or 64-QAM symbol alphabet [9, 17]), the MIMO transmission mode (Transmit Diversity (TxD), Open Loop Spatial Multiplexing (OLSM), or Closed Loop Spatial Multiplexing (CLSM)), and the precoding/number of spatial layers for all served users. Such a channel adaptive scheduling allows the exploitation of frequency diversity, time diversity, spatial diversity, and multi-user diversity.

After the layer mapping, reference symbols are inserted into the precoded data stream and OFDM symbols are assembled. The structure of the reference symbols is shown in Figure 2.8. The assembled OFDM symbols are transformed via IFFT into the time domain. Afterwards, the N_{CP} last samples are attached at the beginning of each OFDM symbol. This part of the signal is called CP and its purpose is to avoid ISI between consecutive OFDM symbols.

Channel Model

The Vienna LTE Link Level Simulator supports block and fast fading channels. In the block fading case, the channel is constant during one subframe (1 ms). In the fast fading case, time-correlated channel impulse responses are generated for each sample of the transmit signal. Currently, the simulator supports the following channel models:

1. Additive White Gaussian Noise (AWGN)
2. Flat Rayleigh fading
3. Power Delay Profile-based channel models such as ITU Pedestrian B, or ITU Vehicular A [18]
4. Winner Phase II+ [19].

The most sophisticated of these channel models is the Winner Phase II+ model. It is an evolution of the 3GPP spatial channel model and introduces additional features such as support for arbitrary 3D antenna patterns.

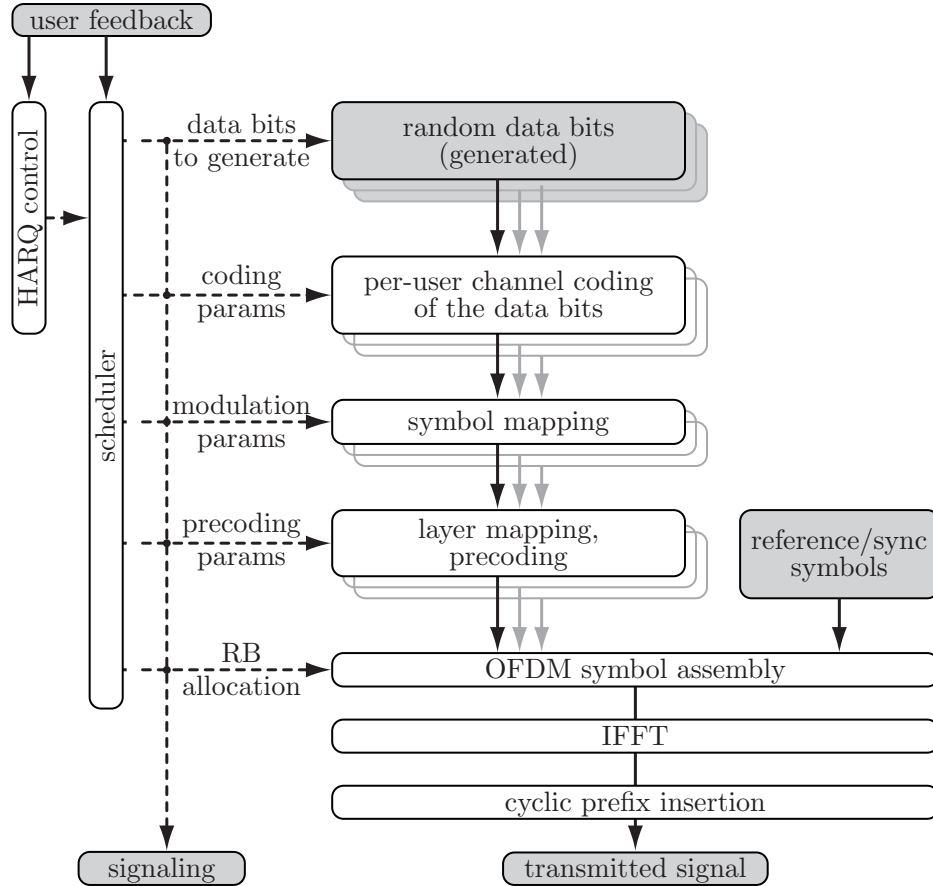


Figure 2.10: Transmitter: implementation in the Vienna LTE link level simulator, as specified in [7–9].

Receiver

Figure 2.11 shows the implementation of the UE receiver. First, the samples of CP are discarded and the remaining part of the received signal is transformed into the frequency domain using the FFT. Afterwards, reference symbols are extracted and the channel is estimated. Currently, five different types of channel estimators are supported within the simulator: (i) Least Squares (LS), (ii) Linear Minimum Mean Squared Error (LMMSE), (iii) Approximate LMMSE [20, 21], (iv) genie-driven (near) perfect channel knowledge based on all transmitted symbols, and (v) perfect channel knowledge. The estimated channel coefficients are used to calculate feedback values, in particular, the supported CQI, the optimum PMI, and the RI [22].

After disassembling the RBs according to UE resource allocation, a MIMO OFDM detection (using the estimated channel) is carried out. The simulator currently supports Zero Forcing (ZF), LMMSE, and soft sphere decoding as detection algorithms. The detected soft bits are decoded to obtain the data bits and several figures

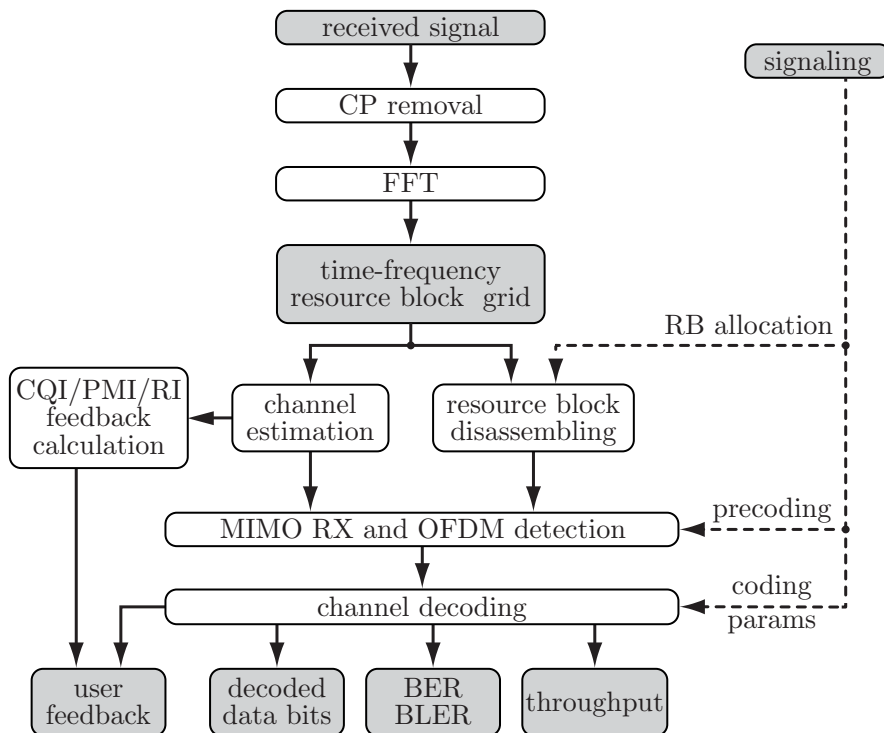


Figure 2.11: LTE downlink receiver structure, as implemented in the Vienna LTE link level simulator.

of merit, such as coded/uncoded Bit Error Ratio (BER), Block Error Ratio (BLER), and throughput.

LTE requires UE feedback in order to adapt the transmission to the current channel conditions. The LTE standard specifies three feedback indicators for that purpose, CQI, RI and PMI [7]. The CQI is employed to choose the appropriate MCS, in order to achieve a predefined target BLER, whereas the RI and the PMI are utilized for MIMO pre-processing. Specifically, the RI informs the eNodeB about the preferred number of parallel spatial data streams, while the PMI signals the preferred precoder that is stemming from a finite code book as specified in [7]. Very similar feedback values are also employed in other systems such as WiMAX and WiFi. The simulator provides algorithms that utilize the estimated channel coefficients to evaluate these feedback indicators [22]. Researchers and engineers working on feedback algorithms can implement other algorithms by using the provided feedback functions as a starting point to define their own functions.

Given this receiver structure, the simulator allows to investigate various aspects, such as frequency synchronization [23], channel estimation [20], or interference awareness [24].

2.2.2 Complexity

Link level simulators are in practice a direct standard-compliant implementation of the Physical (PHY) layer procedures, including segmentation, channel coding, MIMO, transmit signal generation, pilot patterns, and synchronization sequences. Therefore, implementation complexity and simulation time are high. To obtain a simulator with readable and maintainable code, a high level language (MATLAB) has been chosen. This choice enabled to develop the simulator in a fraction of the time required for an implementation in other languages such as C. Furthermore, MATLAB ensures cross-platform compatibility. While MATLAB is certainly slower than C, by means of code optimization (vectorization) and parallelization by the MATLAB Parallel/Distributed Computing Toolbox, simulation runtime can be greatly reduced. Severely difficult-to-vectorize and often-called functions are implemented in C and linked to the MATLAB code by means of MEX functions. Such functions include the channel coding/decoding [25], Cyclic Redundancy Check (CRC) computation [26], and soft sphere decoding.

Furthermore, it is possible to adjust the scale of the simulation to the specific needs. This is achieved by introducing three different simulation scenarios with largely different computational complexity (Figure 2.12):

Single-user Downlink

This simulation type only covers the link between one eNodeB and one UE. Such a set-up allows for the investigation of channel tracking, channel estimation [20], synchronization [27, 28], MIMO gains, Adaptive Modulation and Coding (AMC) and feedback optimization [22], receiver structures [29] (neglecting interference and impact of the scheduling¹), modeling of channel encoding and decoding [30, 31], and physical layer modeling [32], which can be used for system level abstraction of the physical layer.

Single-cell Multi-user Downlink

This simulation setup covers the links between one eNodeB and multiple UEs. This set-up additionally allows for the investigation of receiver structures that take into account the influence of scheduling, multi-user MIMO resource allocation, and multi-user gains. Furthermore, this set-up allows researchers to investigate practically achievable multi-user rate regions. In the current implementation, the simulator

¹ Note that the scheduler in a multi-user system changes the statistics of the individual user's channel, thus influencing the receiver performance.

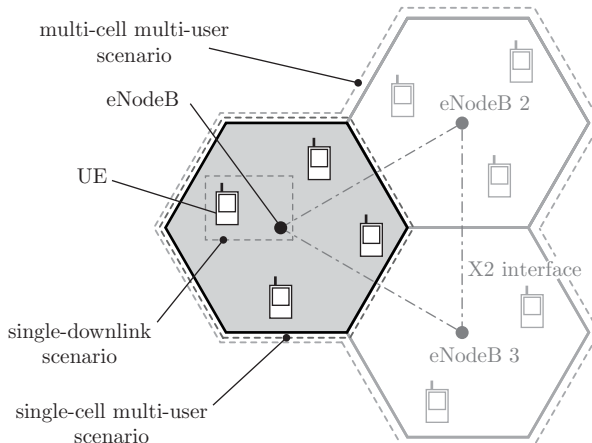


Figure 2.12: Three possible scenarios in the Vienna LTE link level simulator allow to adjust the scale of the simulation complexity: single-downlink, single-cell multi-user, and multi-cell multi-user.

fully evaluates the receivers of all users. However, if receiver structures are being investigated, the computational complexity of the simulation can considerably be reduced by only evaluating the user of interest.

Multi-cell Multi-user Downlink

This simulation scenario is by far the computationally most demanding scenario and covers the links between multiple eNodeBs and UEs. This set-up allows for the realistic investigation of interference-aware receiver techniques [33], interference management (including cooperative transmissions [34] and interference alignment [35, 36]), and network-based algorithms such as joint resource allocation and scheduling. Furthermore, despite the vast computational efforts needed, such simulations are crucial to verify system level simulations.

For most users, the simulation time is a crucial factor and depends on the desired precision and statistical accuracy of the simulation results, the selected bandwidth, the transmission mode, and the chosen modulation order. It should be noted that by a smart choice of the simulation settings, the simulation time can be decreased (e.g., when investigating channel estimation performance, the smallest bandwidth can be sufficient).

2.3 Transmission Model

In this thesis, I consider a generic model of an MIMO OFDM transmission system. A received OFDM symbol of such a system in the frequency domain at the n_r -th

receive antenna can be written as

$$\tilde{\mathbf{y}}_{n_r} = \sum_{n_t=1}^{N_t} \tilde{\mathbf{H}}_{n_t, n_r} \tilde{\mathbf{x}}_{n_t} + \tilde{\mathbf{n}}_{n_r}, \quad (2.3)$$

where $\tilde{\mathbf{H}}_{n_t, n_r} \in \mathbb{C}^{N_{\text{sub}} \times N_{\text{sub}}}$ represents a channel matrix in the frequency domain between the n_t -th transmit and n_r -th receive antennas. The transmitted signal vector is referred to as $\tilde{\mathbf{x}}_{n_t}$, the received signal vector as $\tilde{\mathbf{y}}_{n_r}$. Vector $\tilde{\mathbf{n}}_{n_r} \in \mathbb{C}^{N_{\text{sub}} \times 1}$ is additive white zero mean Gaussian noise with variance σ_n^2 on receive antenna n_r . In the case of a time-invariant channel, channel matrix $\tilde{\mathbf{H}}_{n_t, n_r}$ appears as a diagonal matrix, whereas a time-variant channel forces channel matrix $\tilde{\mathbf{H}}_{n_t, n_r}$ to become non-diagonal. The non-zero non-diagonal elements indicate that the subcarriers are not orthogonal anymore, leading to the so-called Intercarrier Interference (ICI).

Specifically, vector $\tilde{\mathbf{x}}_{n_t} \in \mathbb{C}^{N_{\text{sub}} \times 1}$ in Equation (2.3) comprises precoded data-symbols $\tilde{\mathbf{x}}_{d, n_t} \in \mathbb{C}^{N_d \times 1}$ and pilot-symbols $\tilde{\mathbf{x}}_{p, n_t} \in \mathbb{P}^{N_p \times 1}$ from the set of all possible pilot-symbols \mathbb{P} , at the n_t -th transmit antenna placed by a suitable permutation matrix \mathbf{P}

$$\tilde{\mathbf{x}}_{n_t} = \mathbf{P} [\tilde{\mathbf{x}}_{p, n_t}^T \tilde{\mathbf{x}}_{d, n_t}^T]^T. \quad (2.4)$$

Vector $\tilde{\mathbf{x}}_{n_t}$ has N_{sub} entries, corresponding to the number of non-zero subcarriers. Let me denote the number of pilot-symbols and the number of precoded data-symbols by N_p and N_d , respectively. On subcarrier k of data-symbol vector $\tilde{\mathbf{x}}_{d, n_t}$, the precoding process can be described as

$$[\tilde{x}_{d, 1, k} \cdots \tilde{x}_{d, N_t, k}]^T = \mathbf{W}_k [s_{1, k} s_{2, k} \cdots s_{N_1, k}]^T, \quad (2.5)$$

where $\tilde{x}_{d, n_t, k}$ is a precoded data-symbol at the n_t -th transmit antenna port and the k -th subcarrier, $\mathbf{W}_k \in \mathbb{C}^{N_t \times N_1}$ is a unitary precoding matrix at the k -th subcarrier, with N_1 being the number of transmission layers, and $s_{n_1, k} \in \mathbb{D}^{1 \times 1}$ is the data-symbol of the n_1 -th layer at the k -th subcarrier. Here, \mathbb{D} is the set of available modulation alphabets. A transmission layer represents an abstract concept of a spatial data stream. These spatial data streams are located before the precoder. The number of layers N_1 cannot exceed the minimum of the number of transmit and receive antennas, $N_1 \leq \min(N_t, N_r)$. In order to obtain data-symbol vectors \mathbf{x}_{d, n_t} , one has to stack data-symbols $x_{d, n_t, k}$ obtained via Equation (2.5) at a specific antenna n_t into a vector.

For the derivation of the post-equalization Signal to Interference and Noise Ratio

(SINR), I use an MIMO input-output relation at the subcarrier level, given as:

$$\mathbf{y}_k = \mathbf{H}_{k,k} \mathbf{W}_k \mathbf{s}_k + \mathbf{n}_k + \underbrace{\sum_{m \neq k} \mathbf{H}_{k,m} \mathbf{W}_m \mathbf{s}_m}_{\text{ICI}}. \quad (2.6)$$

Matrix $\mathbf{H}_{k,m} \in \mathbb{C}^{N_r \times N_t}$ denotes the MIMO channel matrix between the k -th and m -th subcarrier. MIMO channel matrix $\mathbf{H}_{k,m}$ contains appropriately ordered elements of matrices $\tilde{\mathbf{H}}_{n_t, n_r}$ located in the k -th row and m -th column. Vector \mathbf{s}_k consists of the data-symbols of all layers at the k -th subcarrier. Vector \mathbf{n}_k represents additive white zero mean Gaussian noise with variance σ_n^2 at subcarrier k . The effective channel matrix is denoted by

$$\mathbf{G}_{k,k} = \mathbf{H}_{k,k} \mathbf{W}_k. \quad (2.7)$$

Furthermore, the average power transmitted on each of the N_l layers is denoted by σ_s^2 . The total power transmitted on each data position is σ_d^2 , while that on each pilot position is σ_p^2 .

Example: When the power is evenly distributed between the data and pilot-symbols, there is:

$$\sigma_s^2 = \mathbb{E} \{ \|s_{l,k}\|_2^2 \} = \frac{1}{N_l}, \quad (2.8)$$

$$\sigma_d^2 = \frac{1}{N_d} \sum_{n_t=1}^{N_t} \mathbb{E} \{ \|\tilde{\mathbf{x}}_{d,n_t}\|_2^2 \} = 1, \quad (2.9)$$

$$\sigma_p^2 = \frac{1}{N_p} \sum_{n_t=1}^{N_t} \mathbb{E} \{ \|\tilde{\mathbf{x}}_{p,n_t}\|_2^2 \} = 1, \quad (2.10)$$

where N_d is the number of data-symbols and N_p the number of pilot-symbols.

2.4 Summary

In this chapter, a brief overview of a current state-of-the-art standard for wireless communications, namely LTE, is provided. Furthermore, the main enabling technologies of LTE at the physical layer, such as OFDM and MIMO, are explained. A simulation tool utilized throughout this thesis, the Vienna LTE simulator, was introduced and described. This simulator is freely available under a "non-commercial academic use license". One of the main motivational aspects behind creation of such a tool was reproducibility [13]. At the end of this chapter, I introduced an analytical transmission model that is utilized throughout this thesis.

The Vienna LTE simulator enables to investigate different aspects of the wireless transmission system and to propose improvements at the transmitter and receiver sides. To name couple of examples, the authors of [37] investigated iterative channel estimation for the LTE system. In [38], the authors proposed a smoothing interpolator for LTE-A system. Timing offset estimation algorithms were proposed in [39, 40].

3 Receiver Performance Modeling

Prior to the process of the design of optimal pilot patterns an accurate model of a receiver is required. With help of such a model, the influence of the changes performed in the transmitter structure on the overall system performance can be investigated. In this chapter, I derive the Mean Squared Error (MSE) for two state-of-the-art channel estimators and show that the MSE of a linear channel estimator can be decomposed into a noise dependent part and a noise independent part. Later in the chapter, the modeling of ICI that occurs in OFDM systems due to time-variant channels, is investigated. Last but not least, I show how to include channel estimation errors into account in the post-equalization SINR of a ZF equalizer and derive a simple analytical model for it.

In [41], the authors derived the MSE for an LS and an LMMSE channel estimator for a time-invariant scenario. In [42, 43], the derivation was extended for the time-variant case. In [44], the power of ICI caused by time-variant channels was derived. The authors additionally derive tight upper and lower bounds for ICI power. A typical assumption of linear channel variations was applied for ICI estimation in [45–47]. This approach was extended to a general polynomial case in [48]. However, the polynomial order is limited due to the ill-conditioning of the estimation matrix. In [41, 49], post-equalization SINR for a ZF equalizer including its channel estimation error was derived. Such an approach allows to analytically include the effect of imperfect channel knowledge on the performance of the overall system.

3.1 Channel Estimation

In the following section, I present the state-of-the-art linear channel estimators and derive analytical expressions for their MSE. The authors of [50] showed that opti-

mal performance of an MIMO channel estimator was obtained with pilot patterns that are orthogonal over individual transmit antennas. Such pilot patterns allow to estimate an MIMO channel as $N_t N_r$ individual SISO channels. Due to optimal performance of such MIMO patterns, my discussion is restricted to pilot-symbol patterns that are orthogonal over individual antennas. Note that the LTE-standard utilizes such orthogonal pilot patterns. To ease the reading, I thus simplify the notation in the following part and omit the antenna indices.

3.1.1 Least Squares Channel Estimation

The LS channel estimate at the pilot-symbol positions is obtained by solving the following minimization problem

$$\hat{\mathbf{H}}_p^{\text{LS}} = \arg \min_{\hat{\mathbf{H}}_p} \left\| \mathbf{y}_p - \hat{\mathbf{H}}_p \mathbf{x}_p \right\|_2^2, \quad (3.1)$$

where the matrix $\hat{\mathbf{H}}_p \in \mathbb{C}^{N_p \times N_p}$ is assumed to be diagonal, representing the channel only at the pilot-symbol positions. Obviously, such an estimator ignores the non-diagonal elements of the channel matrix and treats the potential ICI as noise. More details on this topic can be found in [20]. The resulting MSE at the pilot-symbol positions is given as

$$\sigma_{e,p}^2 = \frac{\sigma_n^2 + \sigma_{\text{ICI}}^2}{\sigma_p^2}. \quad (3.2)$$

By increasing the power radiated at the pilot-symbols σ_p^2 , the channel estimates at the pilot-symbols become more reliable. The channel estimates at the data positions have to be obtained by applying a two-dimensional interpolation.

Figure 3.1 shows an example of an LS channel estimate with a two-dimensional linear interpolation at a Doppler frequency of 115 Hz. The vertical lines represent the pilot-symbol positions. Note that the channel estimates at the data positions are obtained by spanning planes defined by the three nearest pilot-symbols.

In the following, I analyze performance of a general linear channel estimator in terms of MSE. A channel estimate at an arbitrary data position using a linear interpolation is given by a weighted sum of the S nearest channel estimates (in the Euclidean sense of the time-frequency grid) at pilot positions. Let me denote the channel estimate at the j -th data position by $\hat{h}_{d,j}$ and the channel estimate at the i -th pilot position by $\hat{h}_{p,i}$. The lower indices i and j are used as general description of the location in the time-frequency grid. A channel estimate at a data position j

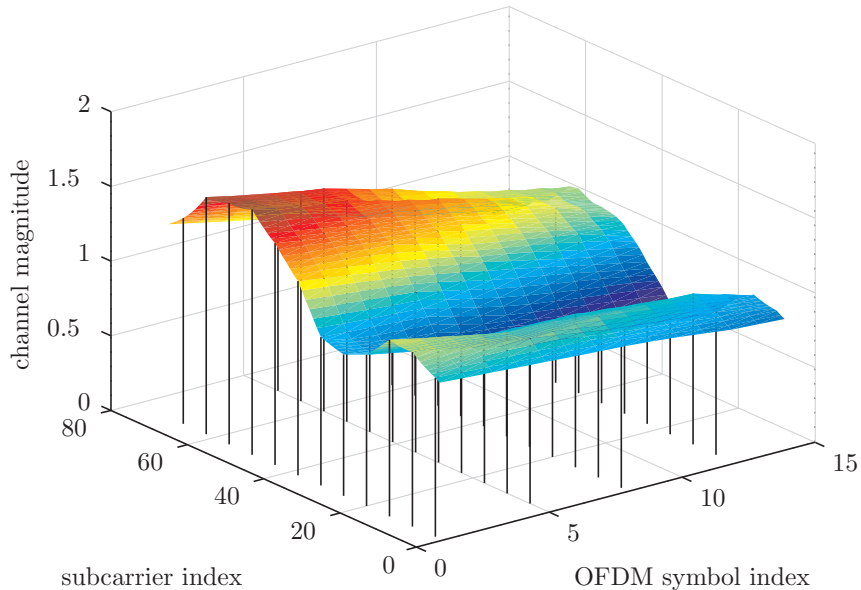


Figure 3.1: An example of the linear interpolation of a channel at a Doppler frequency of 115 Hz (user velocity of 50 km/h). Vertical lines represent positions of the pilot-symbols.

can be expressed as a weighted sum of S closest pilot-symbols

$$\hat{h}_{d,j} = \sum_{i \in \mathcal{P}_j} w_{j,i} \hat{h}_{p,i}, \quad (3.3)$$

where \mathcal{P}_j denotes a set of the S nearest pilot-symbol positions to the data position j . The weight $w_{j,i}$ is a real number that indicates how much the channel estimate at the j -th data position is influenced by the channel estimate at the i -th pilot position.

In the following, I evaluate the performance of such a linear channel estimator by analytically deriving its theoretical MSE at the data positions. Given the definition of the MSE

$$\begin{aligned} \sigma_{e,j}^2 &= \mathbb{E} \left\{ \left\| h_{d,j} - \hat{h}_{d,j} \right\|^2 \right\} \\ &= \mathbb{E} \left\{ \left\| h_{d,j} \right\|^2 \right\} - 2\Re \left\{ \mathbb{E} \left\{ h_{d,j}^* \hat{h}_{d,j} \right\} \right\} + \mathbb{E} \left\{ \left\| \hat{h}_{d,j} \right\|^2 \right\}. \end{aligned} \quad (3.4)$$

For the analytical derivation, I make the following assumptions:

- The channel power is normalized to one ($\mathbb{E} \left\{ \left\| h_{d,j} \right\|^2 \right\} = 1$).
- The channel $h_{d,j}$ at a data position j and the estimation error $n_{\text{est},i} = h_{p,i} - \hat{h}_{p,i}$ at a pilot position i are uncorrelated ($\mathbb{E} \left\{ h_{d,j}^* n_{\text{est},i} \right\} = 0$).

- The channel $h_{p,i}$ at a pilot position i and the estimation error $n_{\text{est},i'}$ at a pilot position i' are uncorrelated ($\mathbb{E}\{h_{p,i}n_{\text{est},i'}\} = 0$).

Let me analyze the three terms in Equation (3.4) individually. The first term is equal to one due to the system model $\mathbb{E}\{\|h_{d,j}\|^2\} = 1$. In the second term, $\hat{h}_{d,j}$ can be replaced by Equation (3.3)

$$\begin{aligned} \Re\left\{\mathbb{E}\left\{h_{d,j}^*\hat{h}_{d,j}\right\}\right\} &= \Re\left\{\mathbb{E}\left\{h_{d,j}^*\sum_{i\in\mathcal{P}_j}w_{j,i}\hat{h}_{p,i}\right\}\right\} \\ &= \Re\left\{\sum_{i\in\mathcal{P}_j}w_{j,i}\mathbb{E}\left\{h_{d,j}^*(h_{p,i}-n_{\text{est},i})\right\}\right\} \\ &= \sum_{i\in\mathcal{P}_j}w_{j,i}\Re\{R_{j,i}\}, \end{aligned} \quad (3.5)$$

where $n_{\text{est},i}$ represents the estimation noise at the i -th pilot position. The last step in the above equation can be justified by the assumption that the channel at the j -th data position and the estimation error at the i -th pilot position are uncorrelated. The coefficient $R_{j,i} = \mathbb{E}\{h_{d,j}^*h_{p,i}\}$ denotes the correlation between the channels at the j -th data-symbol and the i -th pilot-symbol positions.

Let me proceed with the last term of Equation (3.4), in which Equation (3.3) is inserted and consequently the equality $\hat{h}_{p,i} = h_{p,i} - n_{\text{est},i}$, which states that the channel estimate at the pilot-symbol position is given as the true channel superimposed by an estimation error. Note that due to Equation (2.10), it can be shown that the MSE of the LS channel estimator at the pilot-symbol positions is identical to the noise power divided by the power radiated at the pilot-symbols $\frac{\sigma_n^2}{\sigma_p^2}$ for time-invariant channels [41]. In the case of time-variant channels, also the ICI power has to be considered. Therefore the power of $n_{\text{est},i}$ is equal to $\frac{\sigma_n^2 + \sigma_{\text{ICI}}^2}{\sigma_p^2}$. I obtain:

$$\begin{aligned} \mathbb{E}\left\{\|\hat{h}_{d,j}\|^2\right\} &= \mathbb{E}\left\{\left\|\sum_{i\in\mathcal{P}_j}w_{j,i}(h_{p,i}-n_{\text{est},i})\right\|^2\right\} \\ &= \mathbb{E}\left\{\sum_{i\in\mathcal{P}_j}\sum_{i'\in\mathcal{P}_j}w_{j,i}w_{j,i'}(h_{p,i}-n_{\text{est},i})^*(h_{p,i'}-n_{\text{est},i'})\right\} \\ &= \sum_{i\in\mathcal{P}_j}\sum_{i'\in\mathcal{P}_j}w_{j,i}w_{j,i'}R_{i,i'} + \sum_{i\in\mathcal{P}_j}w_{j,i}^2\frac{\sigma_n^2 + \sigma_{\text{ICI}}^2}{\sigma_p^2}. \end{aligned} \quad (3.6)$$

In the last step, I applied the assumption that the estimation error and channel are

uncorrelated. To summarize, Equation (3.4) is simplified to

$$\begin{aligned}\sigma_{e,j}^2 &= \mathbb{E} \left\{ \left\| h_{d,j} - \hat{h}_{d,j} \right\|^2 \right\} \\ &= 1 - 2 \sum_{i \in \mathcal{P}_j} w_{j,i} \Re \{ R_{j,i} \} + \sum_{i \in \mathcal{P}_j} \sum_{i' \in \mathcal{P}_j} w_{j,i} w_{j,i'} R_{i,i'} + \sum_{i \in \mathcal{P}_j} w_{j,i}^2 \frac{\sigma_n^2 + \sigma_{\text{ICI}}^2}{\sigma_p^2}. \quad (3.7)\end{aligned}$$

A part of Equation (3.7) is independent of the term $\frac{\sigma_n^2 + \sigma_{\text{ICI}}^2}{\sigma_p^2}$, as it only depends on the weights $w_{j,i}$ and on the correlation matrix. The dependency of the correlation matrix can also be regarded as dependency on the maximum Doppler spread (or equivalently the user velocity) and Root Mean Square (RMS) delay spread. The second part of the MSE depends on $\frac{\sigma_n^2 + \sigma_{\text{ICI}}^2}{\sigma_p^2}$. This term is on the other hand independent of the correlation matrix. In order to obtain the overall, MSE additional averaging over all data-symbols has to be applied

$$\sigma_e^2 = \frac{1}{N_d} \sum_{j=1}^{N_d} \sigma_{e,j}^2. \quad (3.8)$$

The MSE error can be decomposed into a noise dependent part and a noise independent part

$$\sigma_e^2 = c_e \frac{\sigma_n^2 + \sigma_{\text{ICI}}^2}{\sigma_p^2} + d, \quad (3.9)$$

where c_e is a scalar depending on the weights $w_{j,i}$, given as

$$c_e = \frac{1}{N_d} \sum_{j=1}^{N_d} \sum_{i \in \mathcal{P}_j} w_{j,i}^2 \geq 0. \quad (3.10)$$

The value of the variable c_e is obtained as arithmetic average over all data-symbol positions. Its depends only on the interpolation weights $w_{j,i}$ of the estimator. The constant d is a scalar depending on the weights $w_{j,i}$ as well as the correlation matrix. In the following text, it is referred to as interpolation error (variance) d , given as

$$d = \frac{1}{N_d} \sum_{j=1}^{N_d} \left(1 - 2 \sum_{i \in \mathcal{P}_j} w_{j,i} \Re \{ R_{j,i} \} + \sum_{i \in \mathcal{P}_j} \sum_{i' \in \mathcal{P}_j} w_{j,i} w_{j,i'} R_{i,i'} \right) \geq 0. \quad (3.11)$$

In Appendix A, it is shown that the interpolation error is always greater than or equal to zero. In the proof, perfect channel knowledge at the pilot-symbol positions is assumed. The resulting MSE is equal to the interpolation error. Therefore, the interpolation error can be interpreted as the estimation error caused by the interpolation process.

The choice of the interpolation weights $w_{j,i}$ depends on the interpolation strategy. The simplest way to obtain the interpolation weights for doubly-selective channels is a two-dimensional linear interpolation. In this case, the set of S closest pilot-symbols shrinks to those three closest pilot-symbols that define a plane. Appendix B provides a simple way of obtaining the interpolation weights following a two-dimensional linear interpolation. Additionally, because of geometry reasons shown in Appendix B, the sum of the interpolation weights has to be equal to one, namely $\sum_{i \in \mathcal{P}_j} w_{j,i} = 1$. An example of a two-dimensional interpolation is provided in Figure 3.2. First, three pilot-symbols (red lines), that are closest to a data-symbol (green) line, are located. Second, a plane, that is spanned by these three pilot-symbols, is sampled at the data-symbol position. Note that due to the linear interpolation/extrapolation by a plane, some weights can become negative. More details on how to obtain the interpolation weights for the two-dimensional linear interpolation can be found in Appendix B. In this case, the interpolation weights depend solely on the location of the pilot-symbols and are independent of the noise variance and channel correlation.

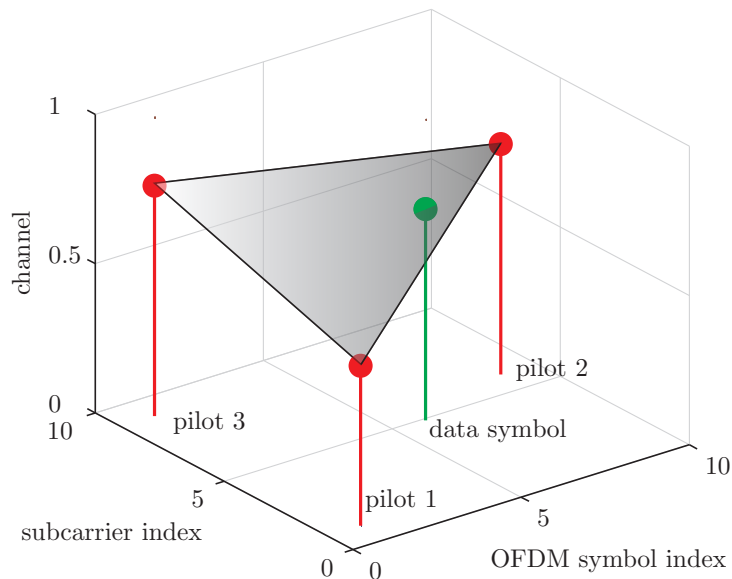


Figure 3.2: Two-dimensional linear interpolation: channel estimate at a data position (green line) is obtained by spanning a two-dimensional plane that is defined by the three closest pilot-symbols (red lines).

In the case of a two-dimensional linear interpolation, the coefficient c_e depends only on the pilot pattern. In the case of a two-dimensional linear interpolation with an LTE SISO pilot-symbol pattern using an LS channel estimator, I find $c_e = 0.6623$, evaluating Equation (3.10). Figure 3.3 shows the value of the interpolation error d versus Doppler frequency for different antenna configurations using LTE pilot-

symbol patterns. Its value grows with increasing Doppler frequency. Note that the interpolation error d in Equation (3.9) causes an error floor in the MSE as a function of SNR of any linear channel estimator. This saturation originates from a low correlation over time. Figure 3.4 shows the simulated (solid lines) and theoretical (dashed lines) MSE of an LS channel estimator, for which an excellent agreement can be found.

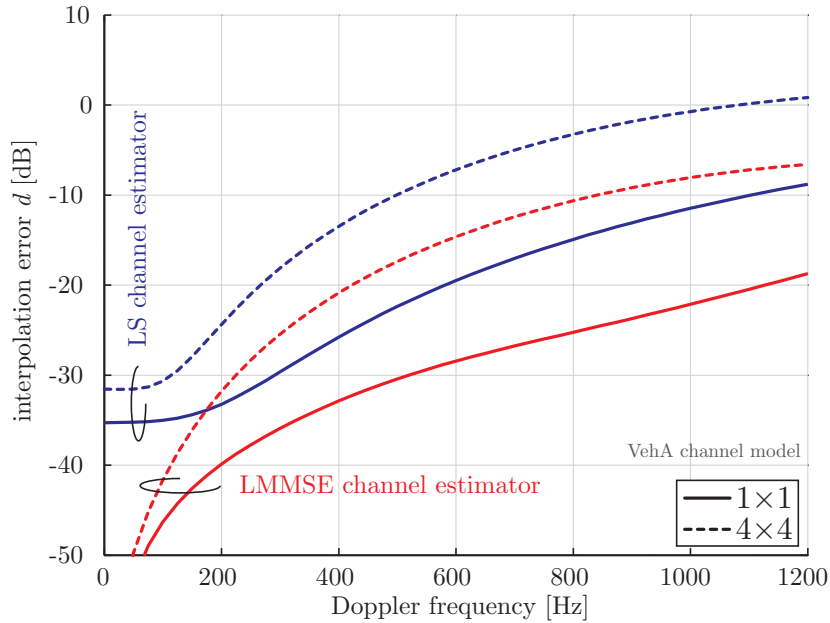


Figure 3.3: Interpolation error d plotted versus Doppler frequency for a different number of transmit antennas. The interpolation error is identical for one and two transmit antennas when utilizing LTE pilot patterns.

3.1.2 Linear Minimum Mean Squared Error Channel Estimation

The LMMSE channel estimator requires knowledge of the second order statistics of the channel and the noise. It can be shown that the LMMSE channel estimate is obtained by multiplying the LS estimate at the pilot-symbol positions with a filtering matrix $\mathbf{A}_{\text{LMMSE}} \in \mathbb{C}^{N_d \times N_p}$ [51]

$$\hat{\mathbf{h}}_d^{\text{LMMSE}} = \mathbf{A}_{\text{LMMSE}} \hat{\mathbf{h}}_p^{\text{LS}}. \quad (3.12)$$

In order to find the LMMSE filtering matrix, the MSE

$$\sigma_e^2 = \mathbb{E} \left\{ \left\| \mathbf{h}_d - \mathbf{A}_{\text{LMMSE}} \hat{\mathbf{h}}_p^{\text{LS}} \right\|_2^2 \right\}, \quad (3.13)$$

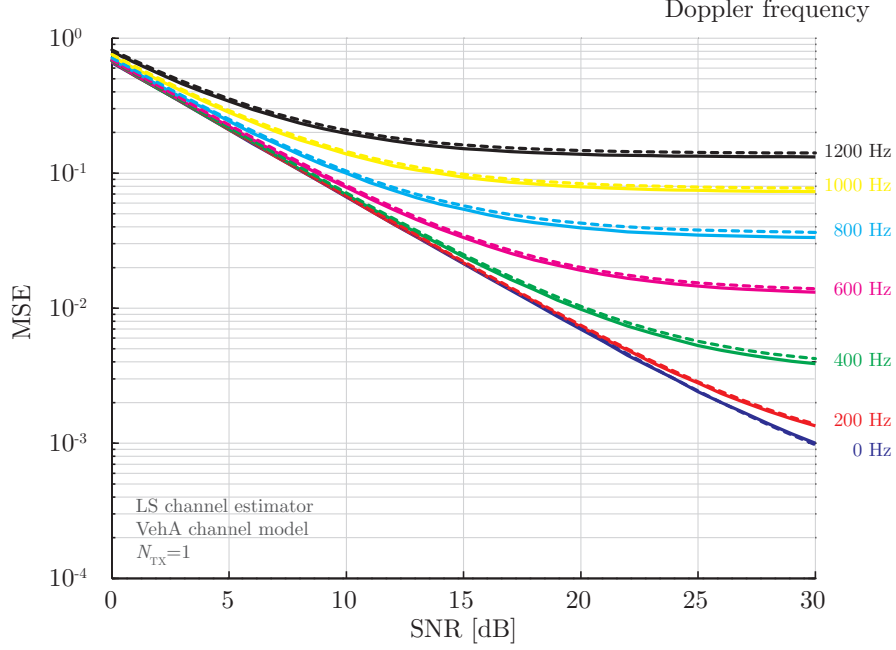


Figure 3.4: Comparison between theoretical (dashed lines) and simulated (solid lines) MSE of an LS channel estimator for a 1×1 transmission system at different Doppler frequencies.

has to be minimized, leading to

$$\mathbf{A}_{\text{LMMSE}} = \mathbf{R}_{\mathbf{h}_d, \mathbf{h}_p} \left(\mathbf{R}_{\mathbf{h}_p, \mathbf{h}_p} + \frac{\sigma_n^2 + \sigma_{\text{ICI}}^2}{\sigma_p^2} \mathbf{I} \right)^{-1}, \quad (3.14)$$

where the matrix $\mathbf{R}_{\mathbf{h}_p, \mathbf{h}_p} = \mathbb{E} \{ \mathbf{h}_p \mathbf{h}_p^H \} \in \mathbb{C}^{N_p \times N_p}$ denotes the channel correlation matrix at the pilot-symbols, and the matrix $\mathbf{R}_{\mathbf{h}_d, \mathbf{h}_p} = \mathbb{E} \{ \mathbf{h}_d \mathbf{h}_p^H \} \in \mathbb{C}^{N_d \times N_p}$ is the channel crosscorrelation matrix.

To derive the theoretical MSE, I insert Equation (3.14) into Equation (3.13):

$$\sigma_e^2 = \mathbb{E} \left\{ \left(\mathbf{h}_d - \left(\mathbf{R}_{\mathbf{h}_d, \mathbf{h}_p} \left(\mathbf{R}_{\mathbf{h}_p, \mathbf{h}_p} - \frac{\sigma_n^2 + \sigma_{\text{ICI}}^2}{\sigma_p^2} \mathbf{I} \right)^{-1} \hat{\mathbf{h}}_p^{\text{LS}} \right) \right. \right. \\ \left. \left. \left(\mathbf{h}_d - \left(\mathbf{R}_{\mathbf{h}_d, \mathbf{h}_p} \left(\mathbf{R}_{\mathbf{h}_p, \mathbf{h}_p} - \frac{\sigma_n^2 + \sigma_{\text{ICI}}^2}{\sigma_p^2} \mathbf{I} \right)^{-1} \hat{\mathbf{h}}_p^{\text{LS}} \right) \right)^H \right\}. \quad (3.15)$$

After a straightforward manipulation, the average MSE at the data subcarriers is expressed as

$$\sigma_e^2 = \frac{1}{N_d} \text{tr} \left\{ \mathbf{R}_{\mathbf{h}_d, \mathbf{h}_d} - \mathbf{R}_{\mathbf{h}_d, \mathbf{h}_p} \left(\mathbf{R}_{\mathbf{h}_p, \mathbf{h}_p} + \frac{\sigma_n^2 + \sigma_{\text{ICI}}^2}{\sigma_p^2} \mathbf{I} \right)^{-1} \mathbf{R}_{\mathbf{h}_p, \mathbf{h}_d} \right\}, \quad (3.16)$$

where N_d is the number of data-symbols.

In order to derive interpolation error d for an LMMSE channel estimator, I assume the expression $\frac{\sigma_n^2 + \sigma_{ICI}^2}{\sigma_p^2}$ being equal to zero. Such an assumption corresponds perfect knowledge of the channel estimates at the pilot-symbol positions. In this way, interpolation error d can be directly obtain from Equation (3.16) as

$$d = \frac{1}{N_d} \text{tr} \left\{ \mathbf{R}_{\mathbf{h}_d, \mathbf{h}_d} - \mathbf{R}_{\mathbf{h}_d, \mathbf{h}_p} \mathbf{R}_{\mathbf{h}_p, \mathbf{h}_p}^{-1} \mathbf{R}_{\mathbf{h}_p, \mathbf{h}_d} \right\}. \quad (3.17)$$

An alternative approach to find the LMMSE channel estimate can be obtained using Equation (3.3), where the set of pilot-symbols \mathcal{P}_j that impact the channel estimate at a specific data position is extended from the three nearest pilot-symbols to all available pilot-symbols. However, in contrast to the previously explained two-dimensional linear interpolator, the weights $w_{j,i}$ depend on the channel correlation matrix and SNR. Therefore, for the LMMSE channel estimator, SNR dependent scalars $c_e(\text{SNR})$ and $d(\text{SNR})$ can be found. In Appendix C, it is shown how to find an SNR independent approximation of the variables c_e and d .

Figure 3.5 depicts the simulated (solid line) and the analytical (dashed line) MSE of an LMMSE channel estimator for different Doppler frequencies. The simulated MSE and the analytically derived MSE show nearly perfect identity.

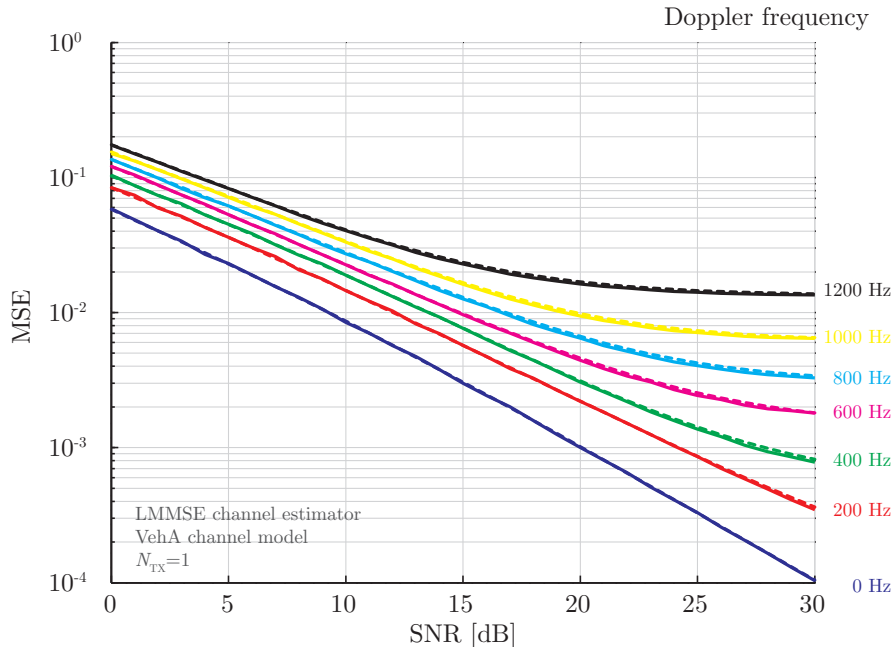


Figure 3.5: Comparison between theoretical (dashed lines) and simulated (solid lines) MSE of an LMMSE channel estimator for a 1×1 transmission system at different Doppler frequencies.

3.1.3 Inter-carrier-Interference Estimation

In scenarios with time-varying channels such as intelligent traffic systems or high speed trains, the orthogonality between subcarriers in OFDM is destroyed causing ICI. In the literature, ICI equalization algorithms have been proposed; however, they assume perfect channel knowledge at sample level. Unfortunately, existing channel estimation algorithms do not provide accurate channel estimates at high Doppler spreads, prohibiting data transmission with high spectral efficiency.

In the following, a Basis Expansion Model (BEM) utilizing a basis consisting of orthogonalized polynomial or Discrete Prolate Spheroidal (DPS) sequences is proposed. Such an approach allows to accurately model ICI at high Doppler frequencies. This is especially useful for ICI estimation algorithms [24], ICI-aware precoding [52], and ICI-aware equalization [24].

The channel matrix in the frequency domain $\tilde{\mathbf{H}}$, from Equation (2.3), is obtained via Fourier transformation of the channel in the time domain including the effects of adding and removing of the CP and the guard-band subcarriers. This procedure can be mathematically formulated as

$$\tilde{\mathbf{H}}_n = \underbrace{F_{\text{GBr}} D_{\text{FFT}} D_{\text{CPr}}}_{\mathbf{D}_1} \tilde{\mathbf{H}}_n^{\text{time}} \underbrace{D_{\text{CP}} D_{\text{FFT}}^H F_{\text{GB}}}_{\mathbf{D}_2}, \quad (3.18)$$

where the additionally introduced lower index n corresponds to the OFDM symbol index. Matrices F_{GBr} and D_{CPr} remove the guard-band subcarriers and the CP, respectively. Matrices D_{CP} and F_{GB} represent the addition of the CP and guard-band, respectively. Finally, matrix D_{FFT} is the Fourier transformation matrix. If the channel is not varying during the transmission of one OFDM symbol, $\tilde{\mathbf{H}}_n$ is a diagonal matrix. On the other hand, if the channel is varying within one OFDM symbol, $\tilde{\mathbf{H}}_n$ is not diagonal and ICI occurs.

The channel matrix in the time domain can be split into two parts, one corresponding to the mean channel and one to the time variation of the channel:

$$\tilde{\mathbf{H}}_n^{\text{time}} = \text{Toep}(\bar{\mathbf{h}}_n) + \Delta \mathbf{H}_n. \quad (3.19)$$

Here vector $\bar{\mathbf{h}}_n$ comprises the mean channel impulse response as experienced by the

n -th OFDM symbol. The Toeplitz operator $\text{Toep}(\cdot)$ is defined as

$$\text{Toep}(\mathbf{b}) \triangleq \begin{bmatrix} b(1) & 0 & \dots & \dots & \dots & 0 \\ \vdots & \ddots & \ddots & & & \vdots \\ b(N) & & \ddots & \ddots & & \vdots \\ 0 & \ddots & & \ddots & \ddots & \vdots \\ \vdots & \ddots & \ddots & & \ddots & 0 \\ 0 & \dots & 0 & b(N) & \dots & b(1) \end{bmatrix}, \quad (3.20)$$

with vector \mathbf{b} being of length N . The resulting Toeplitz matrix is of an appropriate size given by the size of the matrices \mathbf{D}_1 and \mathbf{D}_2 . The channel matrix in the frequency domain using the structure from Equation (3.19) is given by

$$\tilde{\mathbf{H}}_n = \mathbf{D}_1 (\text{Toep}(\bar{\mathbf{h}}_n) + \Delta \mathbf{H}_n) \mathbf{D}_2 \quad (3.21)$$

$$= \text{diag}(\tilde{\mathbf{h}}_n) + \mathbf{D}_1 \Delta \mathbf{H}_n \mathbf{D}_2, \quad (3.22)$$

where vector $\tilde{\mathbf{h}}_n$ contains the diagonal elements of the channel matrix in the frequency domain. The operator $\text{diag}(\mathbf{b})$ creates a diagonal matrix with the vector \mathbf{b} on its main diagonal.

Based on the above considerations, the frequency domain channel matrix can be decomposed using a set of basis functions

$$\tilde{\mathbf{H}}_n = \sum_{i=0}^{N_{\text{order}}} \text{diag}(\gamma_n^{(i)}) \mathbf{D}_1 \mathbf{T}^{(i)} \mathbf{D}_2, \quad (3.23)$$

where the matrices $\mathbf{T}^{(i)}$ are diagonal matrices comprising of the corresponding basis vectors $\mathbf{t}^{(i)}$ on their main diagonals. The channel estimator delivers an estimate of the diagonal elements of the channel matrix in the frequency domain, which corresponds to the mean of the channel during the transmission of one OFDM symbol. In [48], it is shown that if the mean channel of several consecutive OFDM symbols is known, the optimal coefficient can be obtained by means of a linear regression. Using polynomials as the basis functions in Equation (3.23), the coefficients of the BEM are obtained as follows

$$\begin{bmatrix} \hat{\gamma}_n^{(0)} & \hat{\gamma}_n^{(1)} & \hat{\gamma}_n^{(2)} & \dots & \hat{\gamma}_n^{(N_{\text{order}})} \end{bmatrix} = (\mathbf{M}^H \mathbf{M})^{-1} \mathbf{M}^H [\hat{\mathbf{g}}_1 \hat{\mathbf{g}}_2 \dots \hat{\mathbf{g}}_{N_{\text{symbol}}}]^T, \quad (3.24)$$

where matrix \mathbf{M} contains the sampled basis function column wise. For example, for

a polynomial basis matrix \mathbf{M} is given as

$$\mathbf{M} = [\mathbf{1} \ \mathbf{m} \ \mathbf{m}^{\odot 2} \ \dots \ \mathbf{m}^{\odot N_{\text{order}}}], \quad (3.25)$$

where the operator $\cdot^{\odot i}$ denotes the element-wise raise to the power of i and the vector \mathbf{m} has the following structure

$$\mathbf{m} = \left[\left\lfloor \frac{N_s}{2} \right\rfloor, N_s + \left\lfloor \frac{N_s}{2} \right\rfloor, \dots, N_s (N_{\text{symbol}} - 1) + \left\lfloor \frac{N_s}{2} \right\rfloor \right]^T, \quad (3.26)$$

with N_{symbol} being the number of OFDM symbols within one subframe and vector \mathbf{t} is given as

$$\mathbf{t} = [1, 2 \dots N_s - 1, N_s]^T. \quad (3.27)$$

In the following, I discuss different possibilities for the choice of the basis for the BEM.

Linear Case

If polynomials are used as the basis spanning the channel space and the variable N_{order} is set to one ($N_{\text{order}} = 1$), the channel is allowed to vary linearly in time. Higher order channel variations are not taken into account. The same assumption has been made in [45–47]. It was shown that such an assumption is valid at low Doppler spreads.

DPS Sequences

In [53], a low-dimensional subspace spanned by discrete prolate spheroidal sequences is used for time-variant channel estimation. The subspace is designed according to the maximum Doppler frequency of a user. It is shown in [53] that the channel estimation bias obtained with the Slepian basis expansion is more than a magnitude smaller compared to the Fourier basis expansion (i.e., a truncated discrete Fourier transform) [54] or a polynomial. The concept introduced in [53], can be directly extended to the ICI model. The polynomials in Equation (3.23) are replaced by DPS sequences.

Orthogonalized Sequences

When increasing the polynomial order above four in the approach of [48], the matrix in Equation (3.24) becomes ill-conditioned. With increasing number of basis

functions N_{order} , the condition number of the term $\mathbf{M}^H\mathbf{M}$ in Equation (3.24) is also increasing. Therefore, the result of the inversion is not reliable. The maximum modeling order N_{order} depends on the choice of the basis vectors $\mathbf{m}^{\odot i}$. The main requirement on the basis vectors is the orthogonality between their sampled version. Orthogonal sampled sequences that span the same space as the sequences $\mathbf{m}^{\odot 0}, \mathbf{m}^{\odot 1}, \mathbf{m}^{\odot 2}, \dots, \mathbf{m}^{\odot N_{\text{order}}}$ have therefore to be found. During the search for the new orthogonal sequences it has to be considered that it is required to construct corresponding sequences $\mathbf{t}^{\odot 0}, \mathbf{t}^{\odot 1}, \mathbf{t}^{\odot 2}, \dots, \mathbf{t}^{\odot N_{\text{order}}}$ at the sample level. In order to solve the given problem with defined requirements, I apply the Gram Schmidt orthonormalization algorithm [55] on the vectors $\mathbf{m}^{\odot 0}, \mathbf{m}^{\odot 1}, \mathbf{m}^{\odot 2}, \dots, \mathbf{m}^{\odot N_{\text{order}}}$. During the orthogonalization process, also the vectors $\mathbf{t}^{\odot 0}, \mathbf{t}^{\odot 1}, \dots, \mathbf{t}^{\odot N_{\text{order}}}$ have to be transformed in the same manner. The new sampled basis vectors \mathbf{l}_i and the new basis vectors at the sample level \mathbf{k}_i can be constructed as:

$$\mathbf{l}_i = \mathbf{m}^{\odot i} - \sum_{j=1}^{i-1} \frac{\mathbf{l}_j^T \mathbf{m}^{\odot i}}{\mathbf{l}_j^T \mathbf{l}_j} \mathbf{l}_j \quad 0 \leq i \leq N_{\text{order}}, \quad (3.28)$$

$$\mathbf{k}_i = \mathbf{t}^{\odot i} - \sum_{j=1}^{i-1} \frac{\mathbf{l}_j^T \mathbf{t}^{\odot i}}{\mathbf{l}_j^T \mathbf{l}_j} \mathbf{k}_j \quad 0 \leq i \leq N_{\text{order}}. \quad (3.29)$$

By applying this procedure, it is possible to find basis vectors \mathbf{k}_i , such that their sampled versions \mathbf{l}_i are orthonormal. Therefore, the linear regression from Equation (3.24) simplifies to

$$\begin{bmatrix} \hat{\gamma}_n^{(0)} & \hat{\gamma}_n^{(1)} & \dots & \hat{\gamma}_n^{(N_{\text{order}})} \end{bmatrix} = \mathbf{L}^H \begin{bmatrix} \hat{\mathbf{g}}_1 & \hat{\mathbf{g}}_2 & \dots & \hat{\mathbf{g}}_{N_{\text{symbol}}} \end{bmatrix}^T, \quad (3.30)$$

where matrix \mathbf{L} contains the vectors \mathbf{l}_i , $\mathbf{L} = [\mathbf{l}_0 \mathbf{l}_1 \dots \mathbf{l}_{N_{\text{order}}}]$. The ICI model is obtained with the help of Equation (3.23), where matrices $\mathbf{K}^{(i)}$ are used instead of matrices $\mathbf{T}^{(i)}$. Matrices $\mathbf{K}^{(i)}$ contain vectors \mathbf{k}_i on their main diagonals.

This orthogonalization process can be applied not only to polynomials but also to DPS sequences. Furthermore, the basis sequences orthogonal at OFDM symbol level, not only solve the problem of the ill-conditioned matrix, but also decrease the overall complexity of the estimator, since instead of matrix inversion in Equation (3.24) only a matrix multiplication in Equation (3.30) is necessary.

To quantify the performance of various ICI modeling approaches, the ICI modeling MSE is defined as

$$\text{MSE}_{\text{ICI},k,m} = \mathbb{E} \left\{ \left\| \text{vec}(\mathbf{H}_{k,m}) - \text{vec}(\hat{\mathbf{H}}_{k,m}) \right\|_2^2 \right\}, \quad (3.31)$$

with $\text{vec}(\mathbf{H}_{k,m})$ being a vectorized version of the channel matrix between k -th and m -th subcarriers. Matrix $\hat{\mathbf{H}}_{k,m}$ represents the estimate obtained via the method

described in this section.

In Figure 3.6(a), the MSE of various ICI estimation/modeling approaches is illustrated. The MSE for a subcarrier located in the middle of the transmission bandwidth ($k = 36$) is shown to illustrate the ICI from both sides of the considered subcarrier. In this example, the SNR is fixed to 30 dB, Doppler frequency to 1200 Hz, and RMS delay spread to 0 ns. All chosen parameters are rather extreme in order to properly demonstrate the performance of the modeling approaches. The green curve represents the MSE when estimating ICI, assuming linear channel variation between consecutive OFDM symbols. Such an approach allows to decrease the estimation error. The blue and red curves represents MSE corresponding to the orthogonalized polynomial BEM and DPS BEM, respectively. For both of the models, the model order is set to five. These two approaches significantly lower the estimation MSE. Note that DPS sequences slightly outperforms the orthogonalized polynomial basis. Finally, the magenta line presents the MSE when estimation ICI using polynomial basis with model order five.

Figure 3.6(b) shows the performance of the orthogonalized polynomial model versus subcarrier index. As the model order is increased, the MSE of the ICI estimator is decreased. In this example, the SNR is fixed to 30 dB, Doppler frequency to 1200 Hz, and RMS delay spread to 0 ns. Model order one corresponds to the linear case, when a linear channel variation between OFDM symbols is assumed.

3.2 Post-equalization SINR

I consider a time-variant scenario and derive an analytical expression for the post-equalization SINR of an MIMO system using a ZF equalizer based on imperfect channel knowledge.

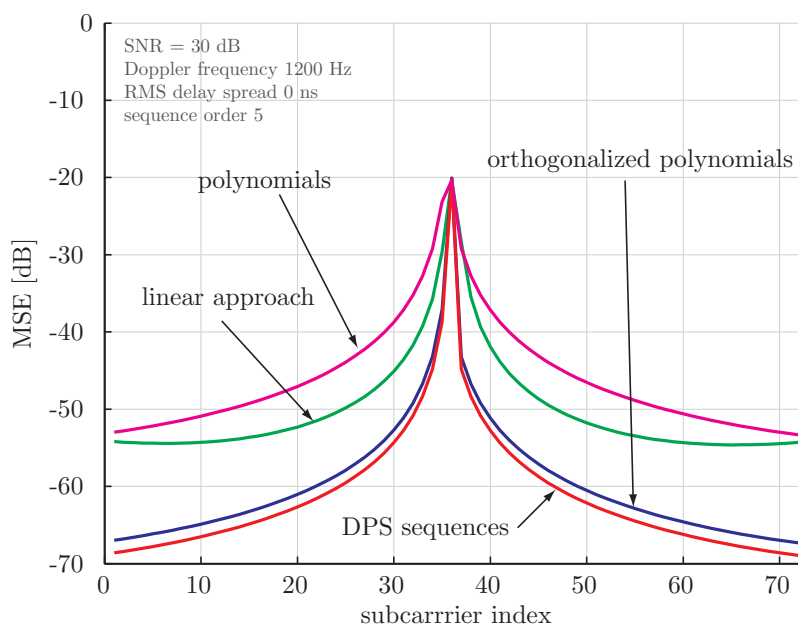
If perfect channel knowledge is available at the equalizer, the ZF estimate of the data-symbol \mathbf{s}_k is given as

$$\hat{\mathbf{s}}_k = (\mathbf{G}_{k,k}^H \mathbf{G}_{k,k})^{-1} \mathbf{G}_{k,k}^H \mathbf{y}_k. \quad (3.32)$$

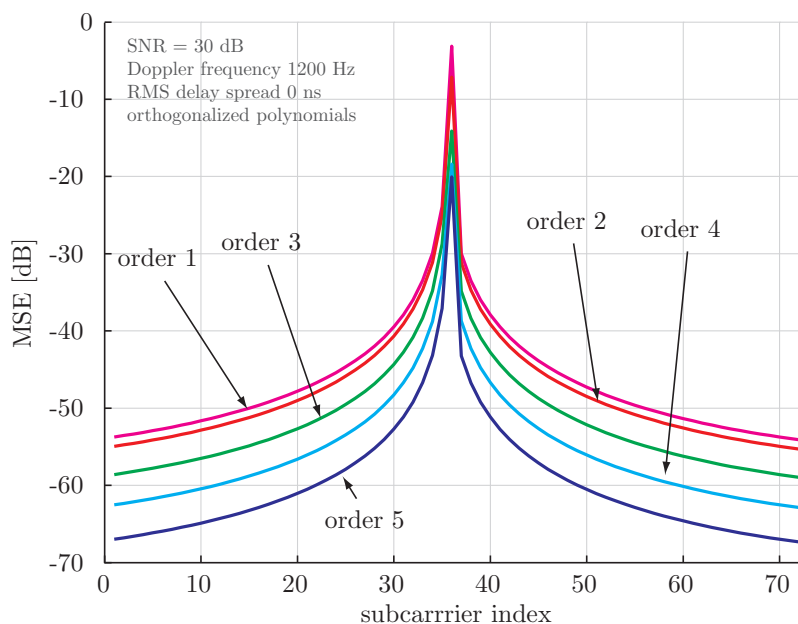
The data estimate $\hat{\mathbf{s}}_k$ given by Equation (3.32) results in a post-equalization SINR of the l -th layer given as [56]

$$\bar{\gamma}_{l,k} = \frac{\sigma_s^2}{(\sigma_n^2 + \sigma_{\text{ICI}}^2) \mathbf{e}_l^H (\mathbf{G}_{k,k}^H \mathbf{G}_{k,k})^{-1} \mathbf{e}_l}, \quad (3.33)$$

where the vector \mathbf{e}_l is an $N_l \times 1$ zero vector with a one on the l -th element. This vector extracts the signal on the corresponding layer after the equalizer. The variable



(a) MSE for various ICI estimation models versus subcarrier index: when utilizing on orthogonalized polynomial basis or a DPS basis, a significant performance improvement can be achieved compared to other methods.



(b) MSE for various ICI estimation model orders: as the the number of basis functions is increased, the MSE is decreasing.

Figure 3.6: MSE for various ICI estimation models versus subcarrier index: in this example, the SNR is fixed to 30 dB, Doppler frequency to 1200 Hz, and RMS delay spread to 0 ns. The blue curve is identical in both figures.

σ_{ICI}^2 represents the ICI power that is given as

$$\sigma_{\text{ICI}}^2 = \mathbb{E} \left\{ \sum_{m \neq k} \|\mathbf{H}_{k,m} \mathbf{W}_m \mathbf{s}_m\|_2^2 \right\}. \quad (3.34)$$

The authors of [44] derived the ICI power leaking from neighboring subcarriers due to the loss of orthogonality between subcarriers. For a typical assumption of the Jakes' spectrum, the ICI power σ_{ICI}^2 can be expressed as

$$\sigma_{\text{ICI}}^2 = 1 - \int_{-1}^1 (1 - |x|) J_0(2\pi f_d T_s x) dx, \quad (3.35)$$

where $J_0(\cdot)$ denotes the zeroth order Bessel function, representing the channel time correlation function. The variable f_d represents the maximal Doppler frequency and T_s the OFDM symbol duration. The maximal Doppler frequency can be obtained by the following expression

$$f_d = v_{\max} \frac{f_c}{c_0}, \quad (3.36)$$

where v_{\max} is the maximal user velocity, f_c the carrier frequency, and c_0 the speed of light.

Figure 3.7 illustrates the ICI power that occurs as an additional noise term in the input-output relation (see Equation (2.6)). The ICI power is increasing with increasing Doppler frequency. At a Doppler frequency of 1200 Hz, it reaches approximately -20 dB. This value of the Doppler frequency corresponds to a velocity of approximately 500 km/h at a carrier frequency of 2.5 GHz. Therefore at typical user velocities, only negligible leakage between subcarriers occurs. However, especially at high Doppler spreads, ICI has to be considered.

Let me proceed to the case of imperfect channel knowledge. I define the perfect channel as the channel estimate $\hat{\mathbf{H}}_{k,k}$ plus an estimation error $\mathbf{E}_{k,k}$ due to the imperfect channel estimation

$$\mathbf{H}_{k,k} = \hat{\mathbf{H}}_{k,k} + \mathbf{E}_{k,k}, \quad (3.37)$$

where the elements of the matrix $\mathbf{E}_{k,k}$ can be modeled as statistically independent random variables, each with variance σ_e^2 . Inserting Equation (3.37) in Equation (2.6), the input-output relation is modified to

$$\mathbf{y}_k = \left(\hat{\mathbf{H}}_{k,k} + \mathbf{E}_{k,k} \right) \mathbf{W}_k \mathbf{s}_k + \mathbf{n}_k + \sum_{m \neq k} \mathbf{H}_{k,m} \mathbf{W}_m \mathbf{s}_m. \quad (3.38)$$

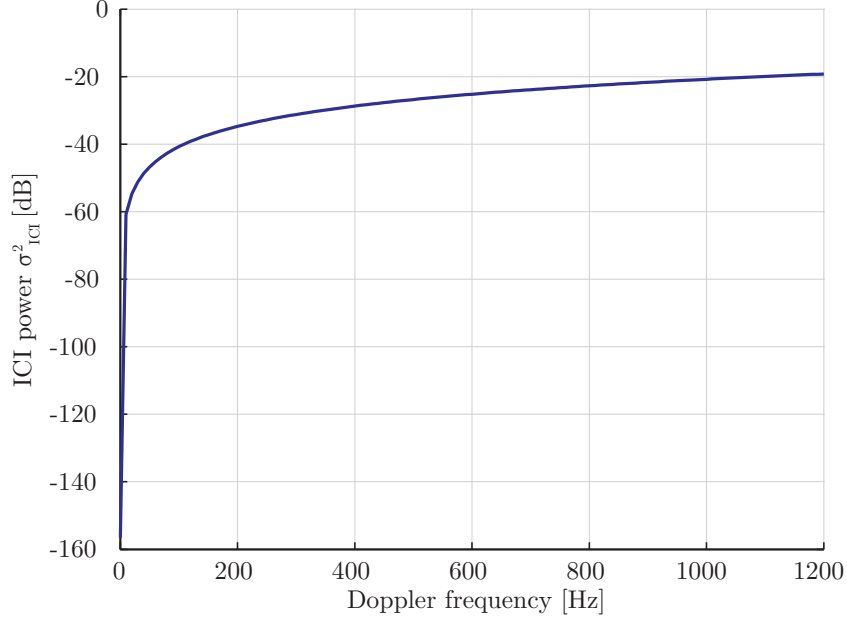


Figure 3.7: ICI power as a function of Doppler frequency: at a Doppler frequency of 0 Hz no ICI occurs. At a high Doppler frequency of 1200 Hz, the ICI power reaches -20 dB.

Since the channel estimation error matrix $\mathbf{E}_{k,k}$ is unknown at the receiver, the ZF solution is given again by Equation (3.32), with the channel matrix $\mathbf{H}_{k,k}$ replaced by its estimate $\hat{\mathbf{H}}_{k,k}$ that is known at the receiver

$$\hat{\mathbf{s}}_k = \left(\hat{\mathbf{G}}_{k,k}^H \hat{\mathbf{G}}_{k,k} \right)^{-1} \hat{\mathbf{G}}_{k,k}^H \mathbf{y}_k, \quad (3.39)$$

with matrix $\hat{\mathbf{G}}_{k,k}$ being equal to $\hat{\mathbf{H}}_{k,k} \mathbf{W}_k$. In Appendix D, the resulting average post-equalization SINR for a ZF equalizer on the l -th layer is derived as

$$\bar{\gamma}_{l,k} = \frac{\sigma_s^2}{\left(\sigma_n^2 + \sigma_{\text{ICI}}^2 + \sigma_e^2 \sigma_d^2 \right) \mathbf{e}_l^H \left(\mathbf{G}_{k,k}^H \mathbf{G}_{k,k} \right)^{-1} \mathbf{e}_l}. \quad (3.40)$$

In Equation (3.40), it is assumed that the available data power σ_d^2 is evenly distributed over individual layers, i.e., $\sigma_s^2 = \frac{\sigma_d^2}{N_1}$. Furthermore, I include a-priori knowledge about the channel estimation performance into the SINR expression of a ZF equalizer by inserting Equation (3.9) in Equation (3.40) and decompose the expression into two parts

$$\bar{\gamma}_{l,k} = f_h(\mathbf{G}_{k,k}) f_{\text{pow}}(c_e, d, \sigma_d^2, \sigma_p^2, \sigma_n^2), \quad (3.41)$$

with the so-called power allocation function $f_{\text{pow}}(c_e, d, \sigma_d^2, \sigma_p^2, \sigma_n^2)$ being

$$f_{\text{pow}}(c_e, d, \sigma_d^2, \sigma_p^2, \sigma_n^2) = \frac{\sigma_d^2}{\left(\sigma_n^2 + \sigma_{\text{ICI}}^2 + \left(c_e \frac{\sigma_n^2 + \sigma_{\text{ICI}}^2}{\sigma_p^2} + d\right) \sigma_d^2\right)} \quad (3.42)$$

and the equalizer allocation function

$$f_h(\mathbf{G}_{k,k}) = \frac{1}{N_l \mathbf{e}_l^H \left(\mathbf{G}_{k,k}^H \mathbf{G}_{k,k} \right)^{-1} \mathbf{e}_l}. \quad (3.43)$$

It was shown in [57] that the post-equalization SINR of a ZF equalizer is a random variable following a Gamma distribution for a stationary channel. Therefore, when assuming a stationary channel, the mean value of the equalizer allocation function can be obtained analytically

$$\sigma_{\text{ZF}, \mathbf{G}} = \mathbb{E} \{ f_h(\mathbf{G}_{k,k}) \}. \quad (3.44)$$

The value of $\sigma_{\text{ZF}, \mathbf{G}}$ is equal to $N_r - N_t + 1$ if neglecting antenna correlation [57, 58]. Inserting Equation (3.44) in Equation (3.41), the average post-equalization SINR for a ZF equalizer under imperfect channel knowledge is obtained as

$$\begin{aligned} \bar{\gamma} &= \mathbb{E} \{ \bar{\gamma}_{l,k} \} \\ &= \frac{\sigma_d^2}{\left(\sigma_e^2 \sigma_d^2 + \sigma_n^2 + \sigma_{\text{ICI}}^2 \right)} \sigma_{\text{ZF}, \mathbf{G}}. \end{aligned} \quad (3.45)$$

Figure 3.8 illustrates the accuracy of the derived post-equalization SINR model for a ZF equalizer. The solid line represents SINR versus SNR obtained via simulation for various MIMO setups. The dashed lines represent the SINR obtained via the derived model. These curves show perfect alignment in the considered SNR range except in the low SNR region, where the simulated SINR values is slightly below the values obtained via the model. This effect is caused by a significant channel power increase by $\mathbf{E}_{k,k}$ when assuming $\mathbf{H}_{k,k} = \hat{\mathbf{H}}_{k,k} + \mathbf{E}_{k,k}$.

3.3 Summary

In this chapter, I dealt with receiver performance modeling that is necessary in order to optimize transmitter structures. In specific, I derived the MSE of a general LS channel estimator utilizing a two-dimensional interpolation and of an LMMSE channel estimator. The MSE of any linear channel estimator can be decomposed into two parts, a noise dependent part and a noise independent part. The later also referred to as the interpolation error. Furthermore, an ICI modeling approach

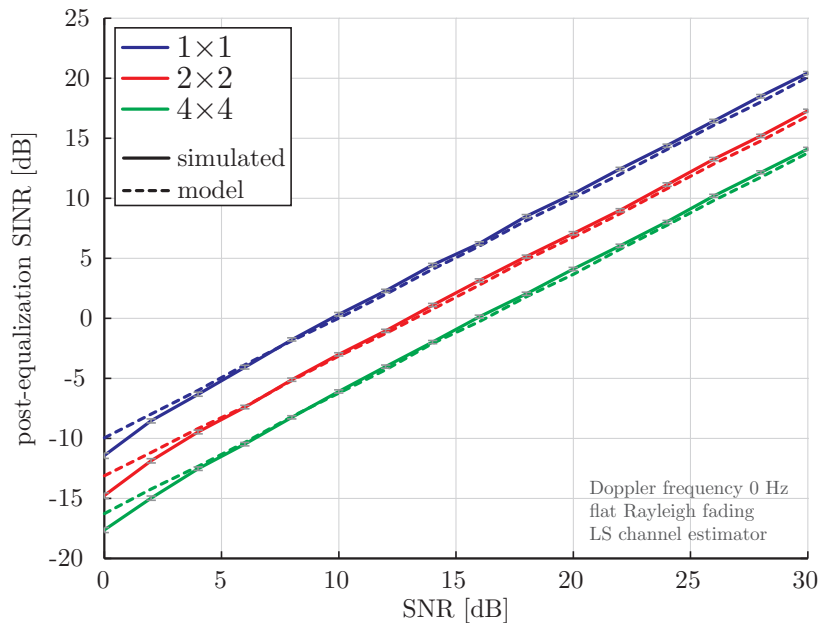


Figure 3.8: Post-equalization SINR model for a ZF equalizer: the solid lines represent SINR values obtained via simulation and the dashed line corresponding SINR values obtained via the derived model in Equation (3.40).

was introduced that allows to precisely model ICI. I utilized a BEM model with DPS sequences or orthogonalized polynomial basis. Last but not least, I derived a post-equalization SINR model for a ZF equalizer under imperfect channel knowledge.

The considered LS and LMMSE channel estimators treat potential ICI as additive noise. Such an approach is clearly suboptimal and the concept has to be extended toward ICI-aware channel estimators. In the derivation of the channel estimation MSE, it was assumed that the interpolation weights are real valued. The extension towards complex-valued interpolation weights is straightforward, but I would like to stress that the complex interpolation weights represent the general case. Another critical assumption during the MSE derivation is that the estimation error at the pilot-symbols and the channel at the data-symbols are uncorrelated. This is clearly a simplification, since a part of the estimation error at the pilot-symbols is caused by ICI that is given by the channel at the data positions. The simulation shows that this assumption can be justified. In the proposed ICI modeling approach, it was assumed that the mean channel is located in the middle of an OFDM symbol. This assumption is typically valid, but not strictly. The derived post-equalization SINR expression of a ZF equalizer provides a useful insight into the performance of a linear receiver. The power of this model lies in the fact that it allows to treat the performance of a receiver analytically. In a real system, however, post-equalization SINR is not the quantity that should be maximized. The network designers are

typically more interested into throughput maximization. Another drawback of the post-equalization SINR is that it can be only expressed for linear equalizers. However, more reliable non-linear solutions are available to cope with channel distortions.

For the derivation of the MSE for a linear channel estimator utilizing a two-dimensional interpolation, I considered a general case without any assumptions on the interpolation weights. The provided results can serve as a basis for a design of an optimal interpolator. Various optimization criteria can be chosen, e.g., overall MSE minimization, interpolation error minimization or the noise dependent part of the MSE minimization.

The provided concept of ICI modeling is especially useful at the receiver. It can be applied to improve the channel estimation performance [24] and in order to design ICI-aware channel equalizers [24]. At the transmitter, the model can be applied to design ICI mitigating precoding [52]. In [59], the ICI modeling approach presented in this chapter was extended employing Karhunen-Loève transformation resulting in a small addition gain due to the optimality of the spanned spaced.

The presented post-equalization SINR model was utilized for the SINR prediction in the system level simulation in [49] and for optimal power distribution in [41].

4 Pilot-Symbol Power Allocation

For the purpose of channel estimation, known symbols are inserted into the transmitted data stream. These so-called pilot-symbols consume valuable resources such as bandwidth and power. Some standards for wireless communication, e.g. LTE, allow to assign different power levels to the data and pilot subcarriers, which creates room for the optimization of the transmission system. A power increase at the pilot subcarriers typically results in a more reliable channel estimate [41], which implies higher throughput, however the power available for the data subcarriers is then decreased given a constant sum power constraint.

In this chapter, I show how to optimally distribute the available power among the pilot and data subcarriers that delivers a maximized system performance. Furthermore, I show how to take advantage of the saturation effect of linear channel estimators at high Doppler spreads caused by the interpolation error. This results in considerable transmit power savings while keeping the overall system performance intact.

It is shown by means of simulations that the channel capacity strongly depends on the power that is assigned to the pilot-symbols [60]. The authors suggested that roughly half of the available power should be assigned to the pilot-symbols for the maximization of the capacity. The authors of [61] showed the impact of different power allocations on the BER. However, only an approximation of the impact on BER by the imperfect channel knowledge is provided for a simple Binary Phase-Shift Keying (BPSK) modulation. In [62], an optimal pilot-symbol allocation was analytically derived for Phase-Shift Keying (PSK) modulations of order two and four, using BER as the optimization criterion. In [50], an optimal pilot-symbol power in MIMO systems was derived based on a lower bound for the capacity. The solution provided by Hassibi and Hochwald is limited only to the LMMSE channel

estimator. When the number of the pilot-symbols is equal to the number of the transmit antennas, half of the available power should be assigned to the pilot-symbols in order to maximize the capacity lower bound. Authors of [63] investigated power allocations among the pilot- and data-symbols for MIMO transmission systems using the post-equalization SINR as the cost function. However, they only considered a lower bound of the SINR expression; and only an LMMSE channel estimator was considered. The optimal solution was given as the ratio of the numbers of the data- and pilot-symbols.

In [41], the authors derived an optimal power distribution among the pilot- and data-symbols for time-invariant channels under imperfect channel knowledge. The optimal distribution of power turned out to be independent of the SNR and of the actual channel realization. The solution was provided for LS and LMMSE channel estimators. The optimal distribution among the pilot- and data-symbols depended on the utilized channel estimator and on the number of transmit antennas. In [64], this work was extended to multi eNodeB scenarios where the interference from the neighboring eNodeBs was included. Due to the LTE pilot-symbol design, the pilot-symbols from the neighboring eNodeBs are overlapping with the data-symbols in the eNodeB of interest, which further complicates the optimization problem. In [64], only the worst case scenario was considered.

With the increasing demand for data rates in wireless networks, also the power consumption is continually increasing [65]. The increasing power consumption results in increased greenhouse gas emissions. Techniques to improve the current situation in wireless networks are thus referred to as green radio. One of the earliest strategies in green radio was to design ultra-efficient power amplifiers [66, 67]. Currently, the focus has shifted more to the MAC layer [68] and to the network design [69]. However, the potential power savings at the physical layer were only poorly investigated.

4.1 Optimal Power Allocation

In this section, I describe how to distribute the available power among pilot- and data-symbols in an optimal manner. As the cost function, I make use of the post-equalization SINR of a ZF equalizer under imperfect channel knowledge. The general case of doubly-selective channels is considered.

In order to keep the overall transmit power constant, the powers radiated at the pilot-symbols σ_p^2 and at the data-symbols σ_d^2 have to fulfill the following equation

$$\sigma_p^2 N_p + \sigma_d^2 N_d = N_p + N_d, \quad (4.1)$$

where the variables N_p and N_d represent the number of pilot-symbols and data-

symbols in a subframe, respectively. In order to describe the interconnection between the pilot-power σ_p^2 and the data-power σ_d^2 , I introduce a variable p_{off} which is the power offset between the power of the pilot-symbols and the data-symbols, denoted by

$$\sigma_p^2 = p_{\text{off}} \sigma_d^2. \quad (4.2)$$

Therefore, σ_p^2 and σ_d^2 can be expressed in terms of the variables N_p , N_d , and p_{off} :

$$\sigma_d^2 = \frac{N_p + N_d}{N_d + N_p p_{\text{off}}}, \quad (4.3)$$

$$\sigma_p^2 = \frac{N_p + N_d}{\frac{N_d}{p_{\text{off}}} + N_p} = p_{\text{off}} \sigma_d^2. \quad (4.4)$$

Inserting Equation (4.3) and Equation (4.4) into the power allocation function and simplifying the expression, I obtain

$$\begin{aligned} f_{\text{pow}} \left(c_e, d, \frac{\sigma_p^2}{p_{\text{off}}}, \sigma_p^2, \sigma_n^2 \right) &= \frac{1}{(\sigma_n^2 + \sigma_{\text{ICI}}^2) \left(\frac{1}{\sigma_p^2} (p_{\text{off}} + c_e) + \frac{d}{\sigma_n^2 + \sigma_{\text{ICI}}^2} \right)} \\ &= \frac{1}{(\sigma_n^2 + \sigma_{\text{ICI}}^2) \left(\frac{\frac{N_d}{p_{\text{off}}} + N_p}{N_p + N_d} (p_{\text{off}} + c_e) + \tilde{d} \right)}, \end{aligned} \quad (4.5)$$

with the variable \tilde{d} being proportional to the interpolation error d (see Equation (3.11)) and given as

$$\tilde{d} = \frac{d}{\sigma_n^2 + \sigma_{\text{ICI}}^2}. \quad (4.6)$$

Note that Equation (4.5) is independent of the channel realization.

Let me proceed to the definition of the optimization problem. The target is to find an optimal value of p_{off} that maximizes the post-equalization SINR in Equation (3.40) while keeping the overall transmit power constant. The optimization problem can be formulated mathematically as

$$\begin{aligned} &\underset{p_{\text{off}}}{\text{maximize}} && \tilde{\gamma}_{l,k} \\ &\text{subject to} && N_d \sigma_d^2 + N_p \sigma_p^2 = N_d + N_p. \end{aligned} \quad (4.7)$$

In order to maximize the post-equalization SINR with respect to the variable p_{off} , the power allocation function in Equation (4.5) has to be maximized with respect to the variable p_{off} . The terms $\sigma_n^2 + \sigma_{\text{ICI}}^2$ and \tilde{d} are larger than or equal to zero (see

Appendix A) and independent of the variable p_{off} . Thus, in order to maximize the power allocation function, the following expression has to be minimized

$$f(\sigma_p^2, \sigma_d^2) = \frac{1}{\sigma_d^2} + \frac{c_e}{\sigma_p^2}, \quad (4.8)$$

which I refer to as simplified power allocation function. The simplified power allocation function can be further simplified when inserting Equation (4.3) and Equation (4.4) leading to

$$\bar{f}(p_{\text{off}}) = \frac{N_d + N_p}{N_p + N_d} (p_{\text{off}} + c_e). \quad (4.9)$$

The above expression depends solely on the power offset among the pilot- and data-powers not on the actual powers. The minimum of the simplified power allocation function in Equation (4.9) can simply be found by differentiation, resulting in the optimal value of the variable p_{off}

$$p_{\text{off,opt}} = \sqrt{\frac{N_d c_e}{N_p}}. \quad (4.10)$$

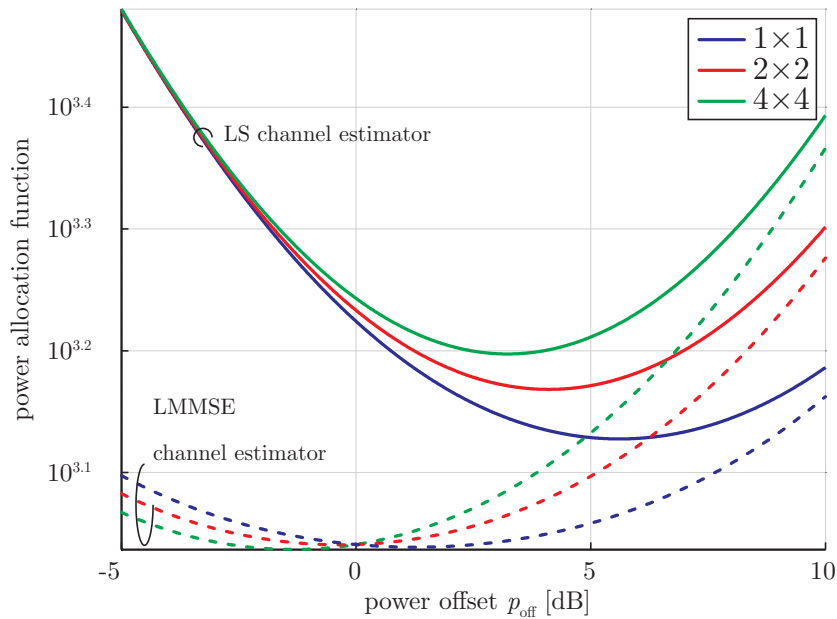


Figure 4.1: The simplified power allocation function $f(p_{\text{off}})$ for different antenna configurations: the simplified power allocation function $f(p_{\text{off}})$ versus power offset for two state-of-the-art linear channel estimators. The functions have distinct minimum points that correspond to the optimal choice of the power offset.

Figure 4.1 shows an example of the simplified power allocation function from Equation (4.9) for LS and LMMSE channel estimators for various numbers of transmit antennas utilizing LTE pilot patterns. All of these functions have distinct minimum points. These minimum points correspond to the maximization of the post-equalization SINR. Typical values of parameters for LTE downlink N_d , N_p , and c_e are provided in Table 4.1. Note that although N_d and N_p depend on the utilized bandwidth, the minimum of $f(p_{\text{off}})$ is independent of it, since N_d and N_p scale with the same constant with increasing bandwidth and actually only their ratio is what matters. The value of c_e is different for four transmit antennas due to the lower number of pilot-symbols at the third and fourth antenna in an LTE downlink system. The last row of Table 4.1 presents the optimal values of $p_{\text{off,opt}}$ for different numbers of transmit antennas and an ITU VehA [70] type channel model for LTE downlink transmission.

Table 4.1: Values of the parameters of $f(p_{\text{off}})$ for different number of transmit antennas at 1.4 MHz bandwidth, ITU PedA [70] channel model, LS and LMMSE channel estimators

Parameter	Tx = 1	Tx = 2	Tx = 4
N_d	960	912	864
N_p	48	96	144
LS			
c_e	0.6623	0.6971	0.7359
d	5.9^{-4}	5.9^{-4}	5.9^{-3}
$p_{\text{off,opt}}$ [dB]	≈ 5.61	≈ 4.11	≈ 3.22
LMMSE			
c_e	0.1819	0.1819	0.2574
d	1.4^{-4}	1.4^{-4}	1.1^{-3}
$p_{\text{off,opt}}$ [dB]	≈ 1.27	≈ -0.35	≈ -1.35

Simulation Results

In the following part, I present simulation results and discuss the performance of LTE transmission systems with different pilot-symbol powers under doubly-selective channels. Table 4.2 presents the most important simulator settings. The performance of the system is demonstrated at an SNR value of 10 dB. Note that as derived earlier, the optimal value of the variable p_{off} is independent of the value of SNR.

Simulation results showing throughput performance for 1×1 , 2×2 , and 4×4 antenna configurations are shown in Figure 4.2 for LS and LMMSE channel estimators. In this example, the Doppler frequency is set to 230 Hz and SNR = 10 dB. Little arrows always indicate the theoretically derived optimal value of the variable p_{off} that

Table 4.2: Simulator settings for power distribution simulations.

Parameter	Value
Bandwidth	1.4 MHz
Number of data subcarriers	72
FFT size	128
CP duration	$\approx 4.76 \mu s$
Number of transmit antennas	1, 2, 4
Number of receive antennas	1, 2, 4
Receiver type	ZF
Transmission mode	Open-loop spatial multiplexing
Channel type	ITU VehA [70]
MCS	adaptive
SNR	10 dB
Doppler frequency	230 Hz

maximizes the post-equalization SINR. Detailed values are listed in Table 4.1. The simulation results show an excellent match with the analytical solution. The precision of the simulated throughput curves is indicated by 95% confidence intervals. Using the optimal value of power offsets between pilot- and data-symbols results in throughput maximization. Moving away from this value, a throughput loss can be observed. However, this loss is usually not severe and the relatively broad maximum indicates a high robustness against inaccurate power distribution between pilot- and data-symbols. This is valid especially for a highly accurate channel estimator such as the LMMSE channel estimator.

A negative value of the variable p_{off} (in dB) corresponds to the reduction of the power radiated at the pilot-symbols and an increasing power radiated at the data-symbols. Such a negative value is optimal in the case of four transmit antennas applying an LMMSE estimator. This kind of channel estimator is of superb performance and therefore requires less power at the pilot-symbols to obtain a high quality channel estimate.

Table 4.3: Throughput gain at SNR = 10 dB when using optimal power distribution between data and pilot-symbols for various number of transmit antennas and LS and LMMSE channel estimators.

Parameter	Tx = 1	Tx = 2	Tx = 4
LS			
throughput gain	10%	10%	7%
LMMSE			
throughput gain	0.5%	0.1%	0.7%

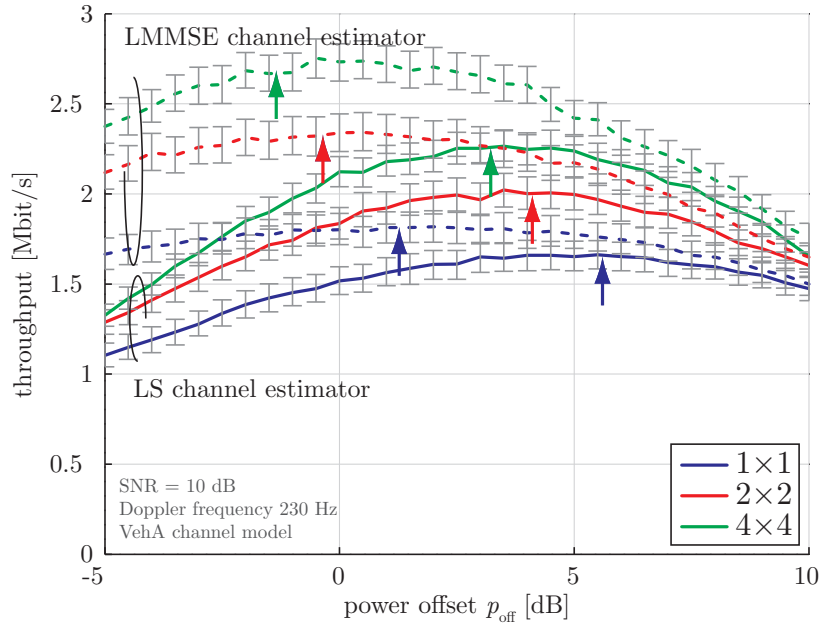


Figure 4.2: Throughput of LTE system versus p_{off} using different channel estimators and various antenna setups. Little arrows always indicate the theoretically derived optimal value of the variable p_{off} , that maximizes the post-equalization SINR.

Considering a single transmit antenna with an LS channel estimator, the optimal value of $p_{\text{off,opt}} = 5.61$ dB may be considered rather high. However, due to the low number of pilot-symbols compared to the number of data-symbols, the overall power radiated at the pilot-symbols is increased approximately by 6% compared to the case of the uniform power distribution.

An OFDM transmission system that does not utilize different power levels for its pilot- and data-symbols, corresponds to $p_{\text{off}} = 0$ dB. In Figure 4.2 can be observed, that using optimal power distribution results in throughput gains up to 10%. Table 4.3 summarizes the throughput gain in percent of a system using optimal power distribution among data- and pilot-symbols compared to a conventional system with equal power distribution. For the LMMSE channel estimators, only a small gain can be observed because the values of $p_{\text{off,opt}}$ are close to 1 (0 dB). Therefore, a system with equal power radiated at the pilot- and data-symbols is already close to the optimum. Although the provided results are shown in the context of the current LTE standard, the presented concept is not limited to it and can principally be applied to any MIMO OFDM based system.

4.2 Power Efficient Power Allocation

As shown in Figure 3.4 and Figure 3.5, the performance of the linear channel estimators becomes saturated with increasing Doppler spread of the channel. This saturation mainly originates in low temporal correlation between the pilot-symbol positions and the data-symbol positions. Due to this effect, a power increase at the pilot-symbols does not necessary lead to an improvement of the quality of the channel estimate. Especially, when the interpolation error is a dominant term in the MSE of a channel estimator. Therefore, in such a situation it might be beneficial not to increase the power radiated at pilot-symbols, but rather invest it for the transmission of the data-symbols. Such a strategy, however, increases the inter-layer interference due to the imperfect channel knowledge. In this section, I present a solution how to take advantage of the above mentioned channel saturation effect by reducing the overall transmit power while preserving the throughput performance of the system.

Let me recall, the problem definition of the optimal power distribution between the pilot- and the data-symbols in Equation (4.7). The optimal power distribution is obtained by the maximization of the post-equalization SINR with respect to the power offset p_{off} while keeping the overall transmit power constant. Let me formulate a relaxed optimization problem, for which I only upper bound the transmit power, and use the actual pilot-symbol power σ_p^2 and data-symbol power σ_d^2 instead of the power offset

$$\begin{aligned} & \underset{\sigma_p^2, \sigma_d^2}{\text{maximize}} && \bar{\gamma}_{l,k} && (4.11) \\ & \text{subject to} && \sigma_p^2 N_p + \sigma_d^2 N_d \leq N_d + N_p. \end{aligned}$$

Similar to utilizing the whole available power (see Section 4.1), the problem of the maximization of the post-equalization SINR corresponds to the minimization of the simplified power allocation function in Equation (4.9):

$$\begin{aligned} & \underset{\sigma_p^2, \sigma_d^2}{\text{minimize}} && f(\sigma_p^2, \sigma_d^2) && (4.12) \\ & \text{subject to} && \sigma_p^2 N_p + \sigma_d^2 N_d \leq N_d + N_p \end{aligned}$$

with the simplified power allocation function given in Equation (4.8)

$$f(\sigma_p^2, \sigma_d^2) = \frac{1}{\sigma_d^2} + \frac{c_e}{\sigma_p^2},$$

where in contrast to Equation (4.9), the variables σ_d^2 and σ_p^2 were used instead of the

variable p_{off} . Note, the reformulated simplified power allocation function directly depends on the power radiated at the pilot- and data-symbols and not on the power offset between them as in Equation (4.9). The new definition allows to decrease the overall transmission power. However, the solution of the optimization problem in Equation (4.12) is identical to utilizing a constant transmit power constraint. The simplified power allocation function is minimized only if the whole available power is utilized. This is caused by the fact that the pilot and the data powers are in the denominators of the simplified power allocation function.

Let me consider the term \tilde{d} in the power allocation function in Equation (4.5). This term is always larger or equal than zero, namely $\tilde{d} \geq 0$. It thus becomes obvious that if it is larger than zero, it causes an overall limitation of the post-equalization SINR. Furthermore, consider a situation when $\tilde{d} \gg f(\sigma_p^2, \sigma_d^2)$. In this case, the post-equalization SINR is mainly determined by the value of \tilde{d} , and its value is almost independent of the choice of σ_p^2 and σ_d^2 .

Therefore, in order to take advantage of the interpolation error, the actual transmit power is minimized while bounding the post-equalization SINR, or equivalently the simplified power allocation function, so that a certain performance of the system is guaranteed. I thus define the optimization problem as follows:

$$\begin{aligned}
 & \underset{\sigma_p^2, \sigma_d^2}{\text{minimize}} && \sigma_p^2 N_p + \sigma_d^2 N_d && (4.13) \\
 & \text{subject to} && f(\sigma_p^2, \sigma_d^2) < a\tilde{d} + f(\tilde{\sigma}_p^2, \tilde{\sigma}_d^2) \\
 & && 0 < \sigma_p^2 < \frac{N_d + N_p}{N_p} \\
 & && 0 < \sigma_d^2 < \frac{N_d + N_p}{N_d} \\
 & && \sigma_p^2 N_p + \sigma_d^2 N_d \leq N_d + N_p.
 \end{aligned}$$

The first condition from Equation (4.13) constraints the simplified power allocation function, so that it does not become larger than the variable \tilde{d} multiplied by a real constant a , that I call a saturation margin, plus a simplified power allocation function evaluated at $\tilde{\sigma}_p^2$ and $\tilde{\sigma}_d^2$, which are the optimal values based on the constraints in Section 4.1. The purpose of the saturation margin a is to ensure that the value of the simplified power allocation function is much smaller than the variable \tilde{d} in case of channel estimation saturation $f(\sigma_p^2, \sigma_d^2) \ll \tilde{d}$. The second and the third conditions from Equation (4.13) warrant that at least some power is assigned to the pilot- and data-symbols, respectively. At the same time, the power assigned to the data- and pilot-symbols is not larger than the maximum available power. The last condition upper bounds the sum transmit power of the pilot- and data-symbols by the maximum available power. It is also assumed that $N_p + N_d$ is constant. This

assumption is typically fulfilled in systems for wireless communications.

The cost function and the constraints formulated in Equation (4.13) are posynomial functions [71] and therefore the formulated optimization problem belongs to the family of geometric programs. Such problems can be efficiently solved employing techniques of convex optimization. For solving the optimization problem in Equation (4.13) I utilized CVX, a package for specifying and solving convex programs [72, 73].

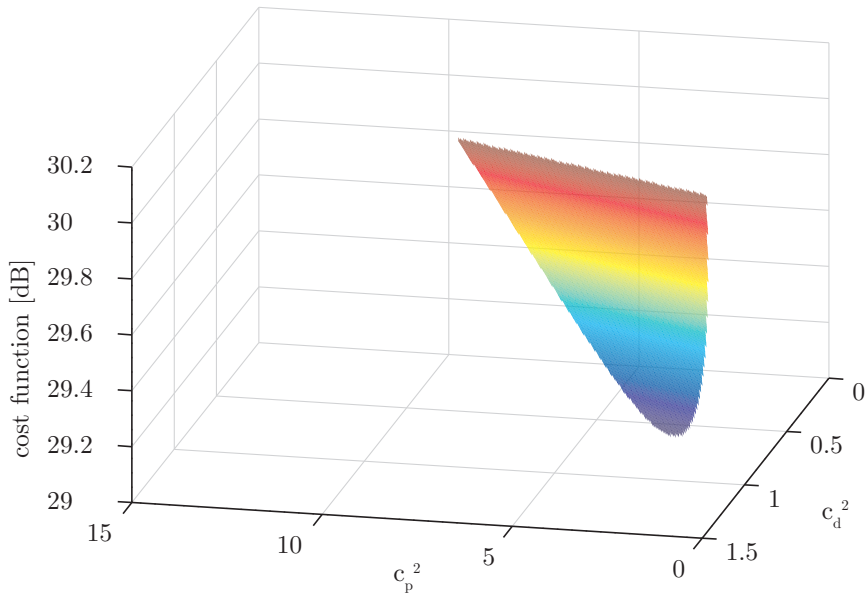


Figure 4.3: Cost function $\sigma_p^2 N_p + \sigma_d^2 N_d$ for an SISO transmission system applying an LS channel estimator at a Doppler frequency of 1150 Hz and SNR = 20 dB.

Figure 4.3 displays an example of a cost function $\sigma_p^2 N_p + \sigma_d^2 N_d$ for an SISO transmission scheme utilizing an LS channel estimator at a Doppler frequency of 1150 Hz and an SNR = 20 dB. In this case, by solving the optimization problem defined in Equation (4.7), variables σ_p^2 and σ_d^2 are chosen by the algorithm to $\sigma_p^2 \approx 2.6$ and $\sigma_d^2 \approx 0.7$, which results in $p_{\text{off}} \approx 5.6$ dB and an actual transmit power saving of around 20%. In this example, the variable $a = \frac{1}{16}$ is set.

Simulation Results

In the following part, I present simulation results and discuss the performance of LTE transmission systems with different pilot-symbol powers under doubly-selective channels. Table 4.4 shows the most important simulator settings.

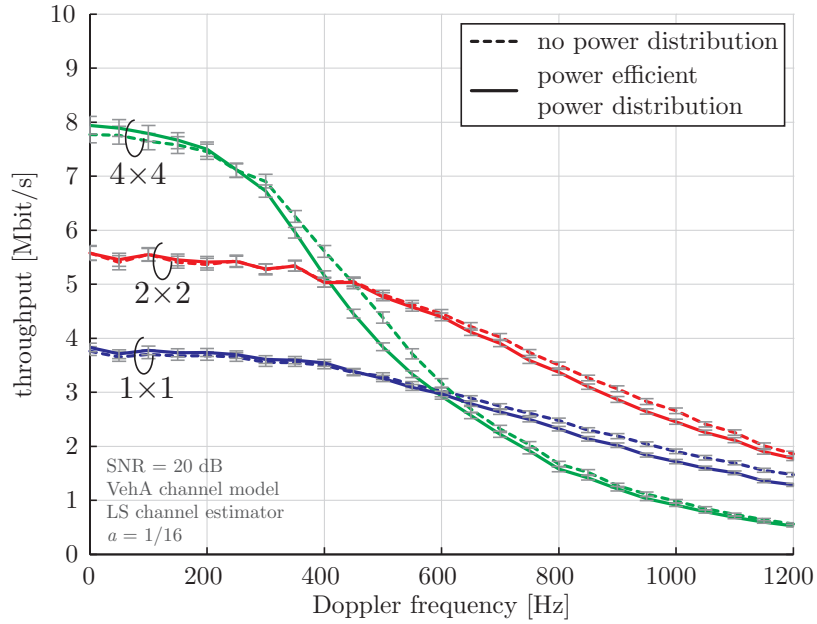
Figure 4.4(a) shows throughput versus Doppler frequency for various numbers of utilized antennas at SNR=20 dB. The dashed line depicts an LTE system with no

Table 4.4: Simulator settings for power efficient power distribution simulations.

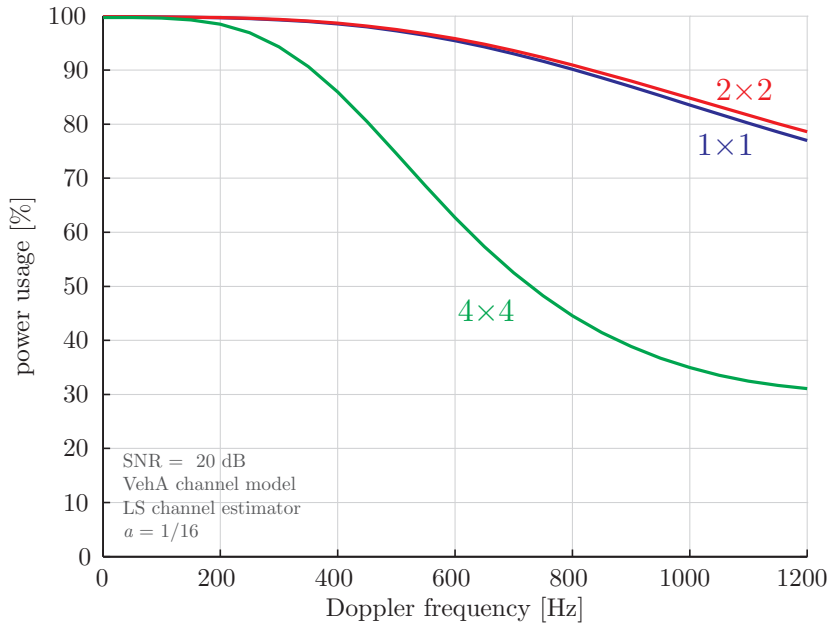
Parameter	Value
Bandwidth	1.4 MHz
Number of data subcarriers	72
FFT size	128
CP duration	$\approx 4.76 \mu\text{s}$
Number of transmit antennas	1, 2, 4
Number of receive antennas	1, 2, 4
Receiver type	ZF
Transmission mode	Open-loop spatial multiplexing
Channel type	ITU VehA [70]
SNR	20 dB

power distribution among pilot- and data-symbols. The continuous line represents a system with the proposed power efficient power distribution among pilot- and data-symbols. The amount of power when utilizing the proposed power efficient power distribution is shown in Figure 4.4(b). In case when no power distribution is applied, the whole available transmit power is utilized. For example, considering a 4×4 transmission system at a Doppler frequency of 1200 Hz, when using the proposed power distribution algorithm almost 70% of the total transmit power can be saved compared to a system with no power distribution, while achieving the same throughput. For the simulated curves 95% confidence intervals are calculated, which are plotted in gray color. Their size indicates a high quality of the simulation results. At lower Doppler frequencies, the system utilizing power distribution outperforms the system without any power distribution. This is consistent with results from [41, 43, 64]. At higher Doppler frequencies the system with power efficient power distribution experiences a small throughput loss, at the same time utilizes less transmit power than the system not utilizing power distribution. Note that the throughput loss can be further decreased by changing the variable a in the first condition of Equation (4.7). In the shown simulation the saturation margin is fixed to $a = \frac{1}{16}$. If no SINR loss is desired, the saturation margin a has to be set to zero, in this case, no power savings are achieved.

Figure 4.4(b) depicts the actual transmit power for various antenna setups versus Doppler frequency at SNR = 20 dB when using the power efficient solution. With increasing Doppler frequency also the amount of power used for the transmission decreases. This behavior can be explained by the fact that the performance of the channel estimators with increasing Doppler spread becomes saturated due to the low temporal channel correlation. Therefore, less power is radiated at the pilot-symbols and at the same time the power at the data-symbols is limited, since it would only increase the inter-layer interference caused by the imperfect channel knowledge.



(a) Throughput comparison of various LTE MIMO systems without any power distribution and with power efficient power distribution at SNR = 20 dB versus Doppler frequency.



(b) Percentage of power for the transmission of LTE MIMO systems for various numbers of transmit antennas plotted versus Doppler frequency utilizing the proposed power efficient power distribution at SNR=20 dB.

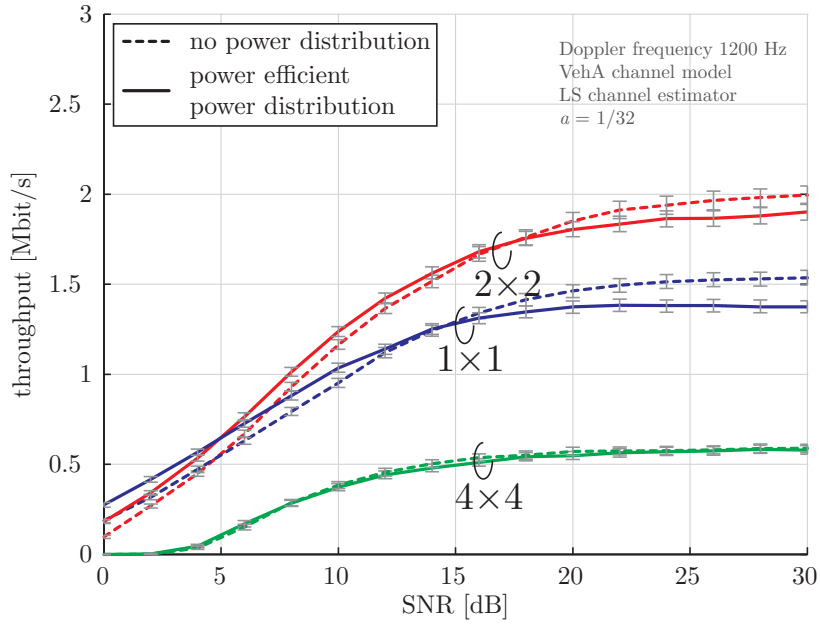
Figure 4.4: Power efficient power allocation versus Doppler frequency.

In Figure 4.5(a), I compare the performance of an LTE system utilizing a unit power distribution with its counterpart, utilizing the proposed power efficient power distribution among pilot- and data-symbols. The throughput is shown as a function of SNR for a VehA channel model and for a fixed Doppler frequency of 1200 Hz. The selected value of the Doppler frequency is rather high, but it serves to illustrate an extreme case with a significant interpolation error d . Because of the choice of the Doppler frequency, the performance of 4×4 LTE systems is inferior to the performance of other considered MIMO setups, no matter which power distribution is utilized, since the LTE pilot pattern utilized for four transmit antennas fails to estimate highly time-variant channels. In the 4×4 case, the throughput of both competing systems is the same, the only difference comes from the amount of utilized power for the transmissions. The amount of utilized transmission power by the power efficient system compared to the system with unit power distribution is shown in Figure 4.5(b). In the 4×4 case, while achieving the same performance for the considered scenario, up to 65% of the transmit power can be saved to achieve the same performance.

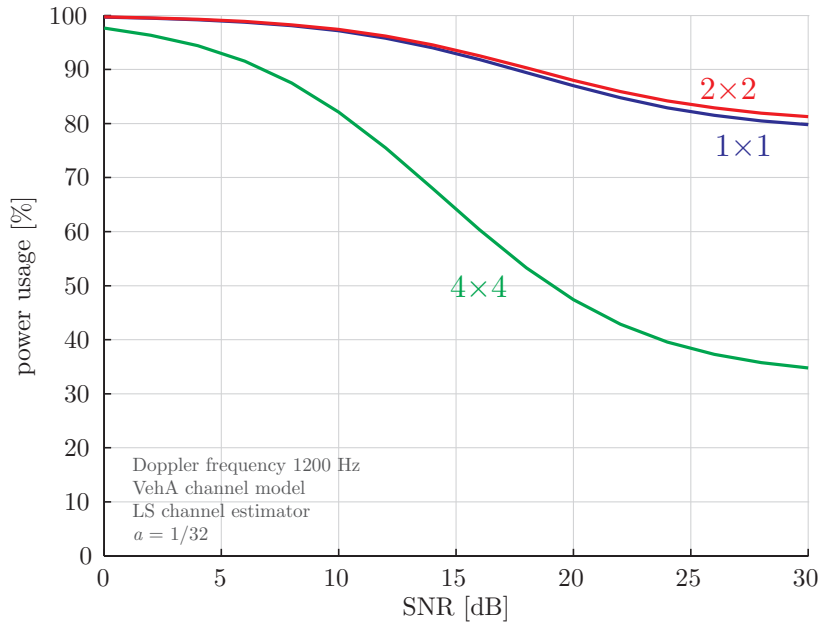
Let me concentrate on the cases of a single transmit antenna and two transmit antennas in Figure 4.5(a) and Figure 4.5(b). In these cases, the applied channel estimator in combination with the pilot patterns provided by the LTE standard does not completely fail to estimate time-variant channels and therefore the considered MIMO schemes outperform 4×4 transmission systems and their throughput grows with increasing SNR. The system utilizing power efficient power distribution outperforms the standard LTE system up to a certain SNR value. In the case of a single transmit antenna, this breakpoint is approximately at 15 dB, in the case of a 2×2 system, approximately at 17 dB. At high SNR values, the system with no power distribution slightly outperforms the power efficient system. The performance gain is smaller than 5%. Figure 4.5(b) shows the amount of power utilized for the transmission by the power efficient system compared to the standard LTE system. At low SNR values the whole available transmit power is utilized, since the performance of the channel estimator is not yet saturated. With increasing SNR, also the power savings are increasing. At the SNR values, at which the power efficient system outperforms the system without power distribution, the power savings reach up to 10%. At high SNR values, only 80% of the total transmit power is utilized, while achieving up to 5% throughput loss.

In Figure 4.6(a) and Figure 4.6(b), I investigate the influence of the saturation margin a on the overall performance of the system and on the power usage. Let me focus on Equation (4.13) for a moment. From the first condition, it can be inferred that an increasing value of the saturation margin a allows a higher value of the simplified power allocation function compared to the optimal solution. By

4. PILOT-SYMBOL POWER ALLOCATION



(a) Throughput comparison of various LTE MIMO systems without any power distribution with power efficient power distribution versus SNR at a Doppler frequency of 1200 Hz.



(b) Percentage of power for the transmission of LTE MIMO systems for various numbers of transmit antennas plotted versus SNR utilizing the proposed power efficient power distribution at a Doppler frequency of 1200 Hz.

Figure 4.5: Power efficient power allocation versus SNR.

allowing a higher value of the simplified power allocation function, also the post-equalization SINR is effectively decreased. At the same time, the power utilized for the transmission is lowered. Therefore, with increasing value of the saturation margin a , a decreasing value of the post-equalization SINR and a decreasing amount of the transmission power are expected.

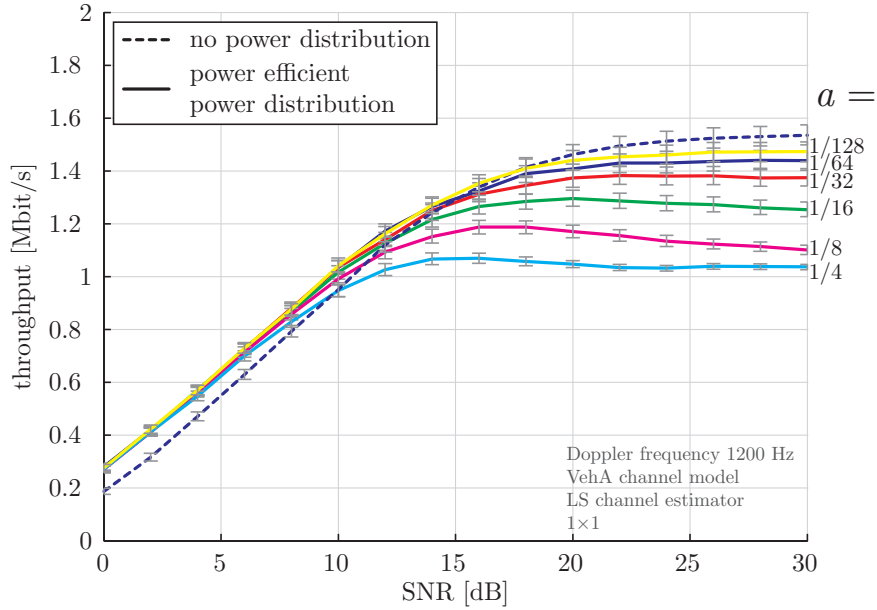
The throughput versus SNR of various SISO transmissions is depicted in Figure 4.6(a) under a VehA channel model at a Doppler frequency of 1200 Hz. The blue dashed line represents a typical LTE system with unit power distribution. The colored solid lines represent power efficient systems with different saturation margins a . Figure 4.6(b) illustrates the amount of transmission power utilized by the power efficient systems with various values of the saturation margin. As expected, with an increasing value of the saturation margin, the performance of the system is upper bounded by the performance of the system with unit power distribution and the transition power is decreasing. Let me consider two extreme cases of the saturation margin. The cyan curves represents a power efficient system with the saturation margin of $\frac{1}{4}$. Such a system outperforms the standard LTE system up to an SNR value of approximately 10 dB, while utilizing much less power than the standard LTE system. However, at higher SNR values the throughput becomes saturated, since a post-equalization drop is allowed. The yellow lines represent a power efficient system with $a = \frac{1}{128}$. Such a system performs very close to a system with no power distribution and reduces the transmission power by approximately 5%. Based on these results, I can conclude that the saturation margin should be chosen based on the operation point such that the performance loss is negligible and the power savings maximized.

In the previous problem formulation Section 4.1, the whole available power had to be utilized, however by increasing the power radiated at the data-symbols, inter-layer interference would be increased, therefore the power radiated at the pilot-symbols is increased, with a negligible effect on the quality of the channel estimate due to the interpolation error with increasing Doppler frequency. The interpolation error is more significant with increasing SNR, therefore the transmit power is lower with an increasing SNR.

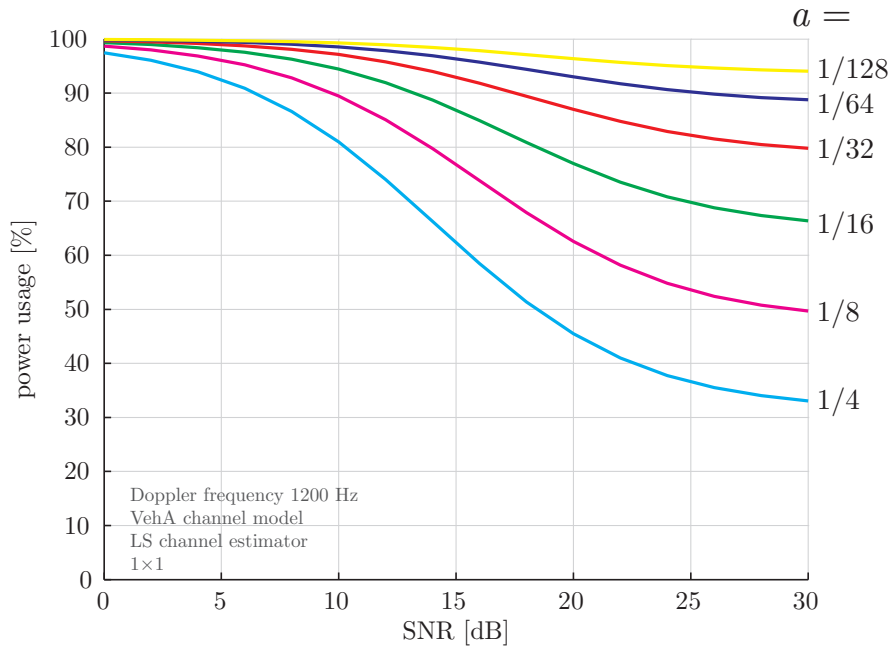
4.3 Summary

In this chapter, I introduced a framework that allows to optimally distribute available power among pilot- and data-symbols. The optimum is based on a maximization of the post-equalization SINR of a ZF equalizer. The optimal power distribution solution depends only on the ratio between pilot- and data-symbols and on the performance of the applied channel estimator, namely on the noise contribution in the

4. PILOT-SYMBOL POWER ALLOCATION



(a) Throughput versus SNR comparison of LTE SISO transmissions without any power distribution with power efficient power distribution at a Doppler frequency of 1200 Hz for various values of the saturation margin a .



(b) Percentage of power for the transmission of an LTE SISO systems for various numbers of transmit antennas plotted versus SNR, utilizing the proposed power efficient power distribution at a Doppler frequency of 1200 Hz for various values of the saturation margin a .

Figure 4.6: Power efficient power allocation versus SNR for various saturation margins a .

MSE. This means that the optimal power distribution is independent of the channel statistics and also of the operation point (SNR). Later in the chapter, I showed how to take advantage of the interpolation error that is growing especially with an increasing Doppler frequency. In this case, when increasing the power that is radiated at the pilot-symbols, the channel estimate quality is not necessary improved and therefore it appears beneficial to increase the power radiated at the data positions. However, due to the imperfect channel knowledge, such an approach would increase the inter-layer interference and therefore it is beneficial to decrease the overall transmit power. I proposed an algorithm that allows to decrease the overall transmit power while keeping the performance of the overall system almost intact compared to the case when the whole available power is utilized.

In order to obtain an SNR independent solution for the optimal power distribution, variables c_e and d are required to be SNR independent. This is true for the LS channel estimator utilizing a two-dimensional linear interpolator. The variables c_e and d depend on SNR in case of the LMMSE channel estimator. Therefore, the optimal power distribution for the LMMSE is also SNR dependent. However, it is possible to find a precise approximation for SNR independent variables c_e and d for the LMMSE channel estimator.

The saturation margin a in the power efficient allocation requires a further investigation and optimization. From the provided results, it can be observed that larger values of the saturation margin save more transmit power but degrade the performance at high SNR values. The performance degradation is however not present at low SNR values. Therefore, an optimal value of the saturation margin as a function of SNR should be found.

In [41], the power distribution among pilot- and data-symbols in time-invariant scenarios was investigated. The authors of [64] extended the analysis towards multiple base stations in the network. This is especially necessary for cell-edge users that experience strong interference from the neighboring base stations. The power distribution framework was extended toward time-variant situations in [43]. In [74], power efficient power distribution among pilot- and data-symbols was introduced.

5 Optimal Pilot-Symbol Pattern Design

Coherent detection is utilized in most of the transmission systems for mobile wireless communications. The performance of such systems especially depends on the utilized pilot-symbol patterns. To avoid jeopardizing the performance of the overall system, standardization organizations prefer fixed and therefore robust pilot-symbol patterns, which allow to estimate the transmission channel with sufficient high accuracy under various channel conditions. This overprovisioning approach leads to an advantage in terms of system robustness at the cost of reducing the system efficiency.

In this chapter, I investigate how to optimally design pilot-symbol patterns. First, I show how to find pilot-symbol patterns that maximize an upper bound for the constrained channel capacity. In the next step, I include power distribution among pilot- and data-symbols into the optimization framework. In the last part of the chapter, I show how to exploit advantages offered by the optimal pilot-symbol patterns in MIMO OFDM systems. So-called adaptive pilot-symbol patterns are introduced that adjust to the varying channel statistics.

A summary of various pilot-symbols design methods is provided in [75]. The earliest methods aimed to minimize the MSE of a channel estimator [76, 77]. The authors of [76, 77] showed that equi-powered, equi-spaced pilot-symbols lead to the lowest MSE. In contrast to these findings, in [78], it was shown that for channel estimation of doubly-selective channels, diamond-shaped pilot-symbol patterns are optimal in terms of channel estimation MSE. This solution was obtained for a given pilot-symbol overhead. It was not shown how to choose distance parameters of the diamond-shaped pilot-symbol pattern for various channel types. The diamond-shaped pilot-symbol patterns are discussed later in this chapter. The authors of [50, 79] proposed a design pattern that maximizes the channel capacity. There are many different approaches for designing pilot-symbol patterns based on

the minimization of BER [80] or Symbol Error Ratio (SER) [81].

The adaptation of the pilot patterns in OFDM systems was first proposed in [82]. Simeone and Spagnolini designed pilot patterns in a way that the effective SNR loss due to the channel estimation error remained limited within a desired bound. Their solution requires a complex Kalman channel estimator and only a greedy recommendation was proposed when designing the pilot patterns. A similar approach was presented in [83], the authors of which designed pilot patterns such that the channel estimation MSE was bounded as desired by the system designer while minimizing the pilot-symbol overhead. The presented solution was limited to a LMMSE channel estimator and a LS channel estimator with a linear interpolation. The authors of [84] considered the flatness of the channel estimation MSE as the cost function for their adaptive pilot design. The proposed solution was applied with an LMMSE channel estimator and with an LMMSE approximation. In [85], the authors considered a Nyquist sampling theorem as the design criterion for the pilot-symbol placement in order to preserve channel estimation performance. The presented solutions [82–85] for adaptive pilot pattern design focus on the channel estimation performance in various forms as the cost function, with less or no emphasis on the throughput. Additionally, the presented solutions are mostly limited to an LMMSE channel estimator, which in reality cannot be utilized due to its high computational complexity and its a-priori requirements on the channel statistics.

5.1 Optimal Pilot-Symbol Patterns

In this section, it is shown how to design optimal pilot-symbol patterns for doubly-selective channels. First, I concentrate on the case of unit power distribution among pilot- and data-symbols and investigate the performance gain that is achieved by optimal pilot patterns. In the second part, I include power distribution among the pilot- and data-symbol into the problem formulation. I show how to obtain optimal pilot-symbol patterns with an optimal power distribution for a given channel autocorrelation matrix and an SNR value.

In [78], Choi and Lee showed that for a given amount of pilot-symbol overhead, in terms of MSE, it is optimal to position the pilot-symbols in a diamond-shaped constellation. It is, however, not shown how to choose shape parameters of the diamond-shaped pilot-symbol pattern and consequently how much overhead is required for a proper channel estimation. Figure 5.1 shows an example of such a diamond-shaped pilot-symbol pattern. Diamond-shaped pilot-symbol patterns can be decomposed into two patterns with pilot-symbols equi-spaced in time and in frequency directions with distances D_t and D_f , respectively. These two patterns with equi-spaced pilot-symbols are separated from each other by $\lceil \frac{D_t}{2} \rceil$ in the time direc-

tion and by $\lceil \frac{D_f}{2} \rceil$ in the frequency direction. Therefore, a diamond-shaped pattern is fully described by two variables D_f and D_t . Figure 5.1 shows an example of a diamond-shaped pilot-symbol pattern with $D_f = 10$ and $D_t = 4$.

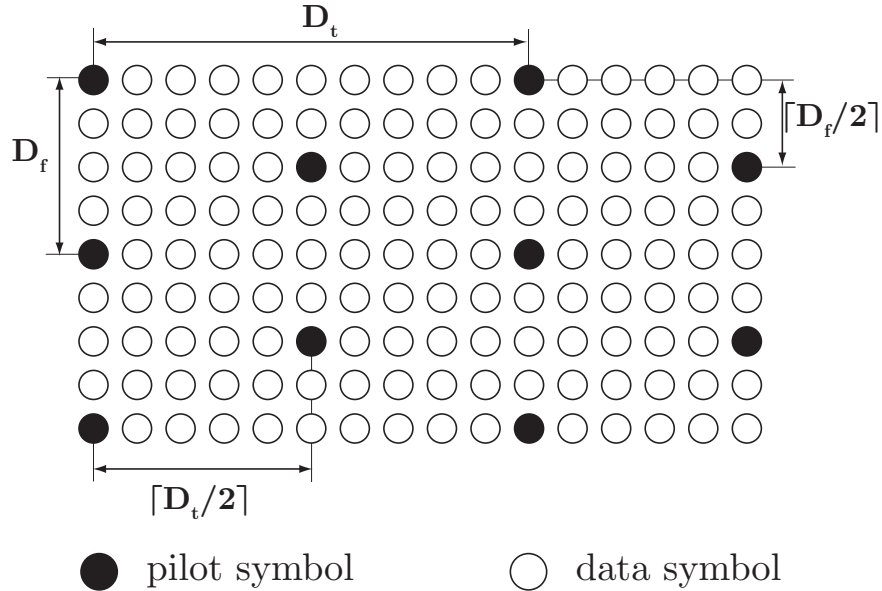


Figure 5.1: Example of a diamond-shaped pilot-symbol pattern: the pilot-symbol pattern is fully described by two variables D_f and D_t . These parameters determine the pilot-symbol density in the time and the frequency dimension.

Note that also LTE utilizes such a diamond shaped pilot-symbol pattern with $D_f = 6$ and $D_t = 7$. Considering only diamond-shaped pilot-symbol patterns, I continue my investigation and show which diamond patterns are optimal. Although I continue my investigation with diamond-shaped pilot-patterns, the presented optimization framework is not restricted solely to this family of pilot patterns.

In order to investigate the optimal choice of the pilot pattern, knowledge of the channel estimator performance with a given pilot pattern is required. Basic principles are provided in Section 3.1, where I showed that the MSE of a linear channel estimator can be decomposed into a noise dependent part $c_e (\sigma_n^2 + \sigma_{\text{ICI}}^2)$ and a noise independent part d , the later also called interpolation error. The noise dependent part is, besides the noise, determined by a coefficient c_e . The coefficient c_e from Equation (3.9) is purely defined by the pilot-symbol pattern for an LS channel estimator. The interpolation error d additionally depends on the channel autocorrelation matrix. Therefore, from this point on, I use the following notation $c_e(D_f, D_t)$ and $d(D_f, D_t, \mathbf{R}_h)$, in which the variable \mathbf{R}_h represents the channel autocorrelation matrix.

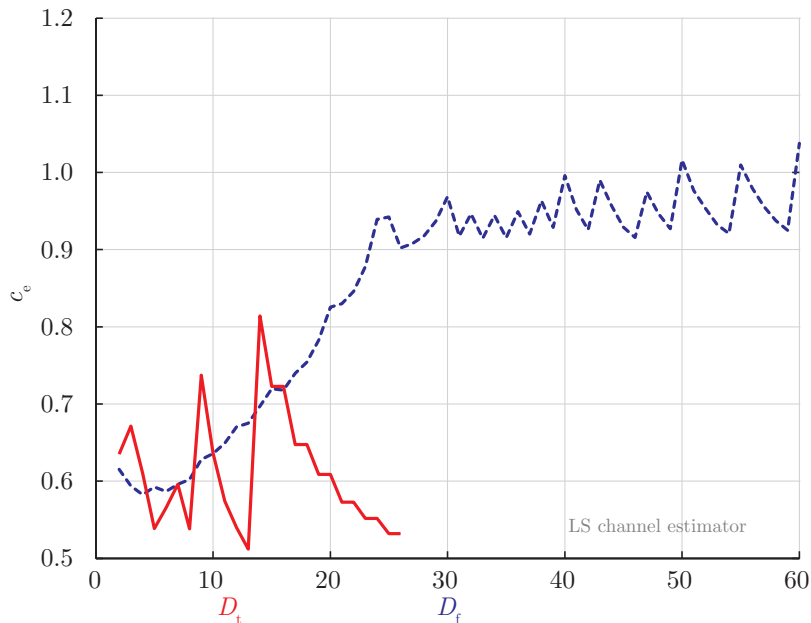


Figure 5.2: The red solid curve represents the coefficient $c_e(D_f, D_t)$ versus D_t while keeping $D_f = 7$. The blue dashed curve shows the behavior of the coefficient $c_e(D_f, D_t)$ versus D_f while keeping $D_t = 7$. Both curves are shown for an LS channel estimator.

Figure 5.2 shows an exemplarily behavior of the coefficient $c_e(D_f, D_t)$ versus the distance between two adjacent pilot-symbols in one dimension while the distance in the second dimension is fixed. Let me first consider a case, in which the distance in the time direction between adjacent pilot-symbols D_t is fixed and the distance in the frequency direction is varied. This case corresponds to the dashed blue curve in Figure 5.2. The behavior is intuitive to understand up to a certain distance. With an increasing distance between pilot-symbols D_f , the variable $c_e(D_f, D_t)$ is also increasing. The curve is not perfectly smooth due to the required extrapolation for points outside the diamond shape. In [86, 87], the authors considered only interpolated channel estimates and the value of the variable c_e grows with an increasing distance between the pilot-symbols. The pilot pattern is always located in a symmetric position with respect to the center of the time-frequency grid. Due to the centralization of the pilot pattern, the number of the points outside of the diamond shape can vary depending on the distance parameters of the diamond pattern. Consider a case, in which increasing the distance between pilot-symbols in the frequency direction does not decrease the amount of pilot-symbols in a given bandwidth. In such a case, there are less data positions to extrapolate and therefore the value of $c_e(D_f, D_t)$ slightly decreases even though the distance between the pilot-symbols is increased. This effect is even more pronounced when the variable D_f becomes larger and the amount of the data positions to extrapolate becomes significant compared to

the number of the total data-symbols. Therefore, at higher values of D_f , a sawtooth curve behavior of the variable $c_e(D_f, D_t)$ can be observed. If D_f is increased by one and the variable $c_e(D_f, D_t)$ changes from a local minimum to a local maximum, the amount of the pilot-symbols in the frequency direction is decreased by one. This behavior can be clearly observed in the red solid curve in Figure 5.2, which shows the value of the variable $c_e(D_f, D_t)$ versus D_t while keeping D_f fixed. The sawtooth behavior originates from the fact that only 14 OFDM symbols are considered in order to be able to consistently compare the proposed system with a conventional LTE system. Therefore, there is a significant number of data positions to extrapolate compared to the total number of data positions. Note that the maximum distance between pilots in the time direction is 26. This distance value ensures that at least two pilot-symbols in the time direction are utilized within the considered 14 OFDM symbols.

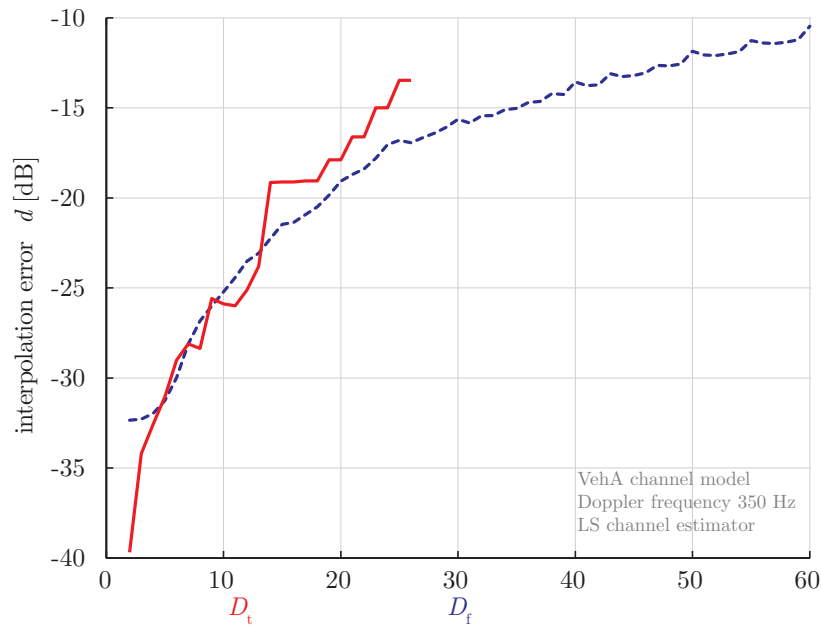


Figure 5.3: The red solid curve represents interpolation error $d(D_f, D_t, \mathbf{R}_h)$ versus D_t while keeping $D_f = 7$. The blue dashed curve shows the behavior of interpolation error $d(D_f, D_t, \mathbf{R}_h)$ versus D_f while keeping $D_t = 7$. Both curves are shown for an LS channel estimator and VehA channel model for a Doppler frequency of 350 Hz.

Figure 5.3 shows the behavior of the interpolation error $d(D_f, D_t, \mathbf{R}_h)$ for a varying distance in the frequency direction while the distance in the time direction is fixed (blue dashed line) and the corresponding case, in which the distance in the time direction is varied while the distance in the frequency direction is fixed (red solid line). The behavior of both curves is intuitive to understand, as an increase in the distance in either direction causes an increase of the interpolation error. Note that

the interpolation error depends on the second-order statistics of the channel. If the correlation is strong, the saturation coefficient is small [86]. The interpolation error, shown in Figure 5.3, can be interpreted as a bound on the best performance of an LS estimator for a Doppler frequency of 350 Hz under the VehA channel model. If no noise and no ICI are present, the overall MSE is equal to the interpolation error $d(D_f, D_t, \mathbf{R}_h)$, as can be inferred from Equation (3.9).

Figure 5.4 illustrates the behavior of the interpolation error $d(D_f, D_t, \mathbf{R}_h)$ as a function of the pilot-symbol distance D_t with a fixed pilot-symbol distance $D_f = 7$ for Doppler frequencies between 0 and 1200 Hz and with a fixed RMS delay spread of 400 ns. The value of the interpolation error grows with an increasing Doppler frequency and also with increasing pilot-symbol distance in the time direction D_t . This demonstrates a tendency that the performance of the channel estimator utilizing a fixed pilot pattern becomes poorer as the value of Doppler frequency is increasing.

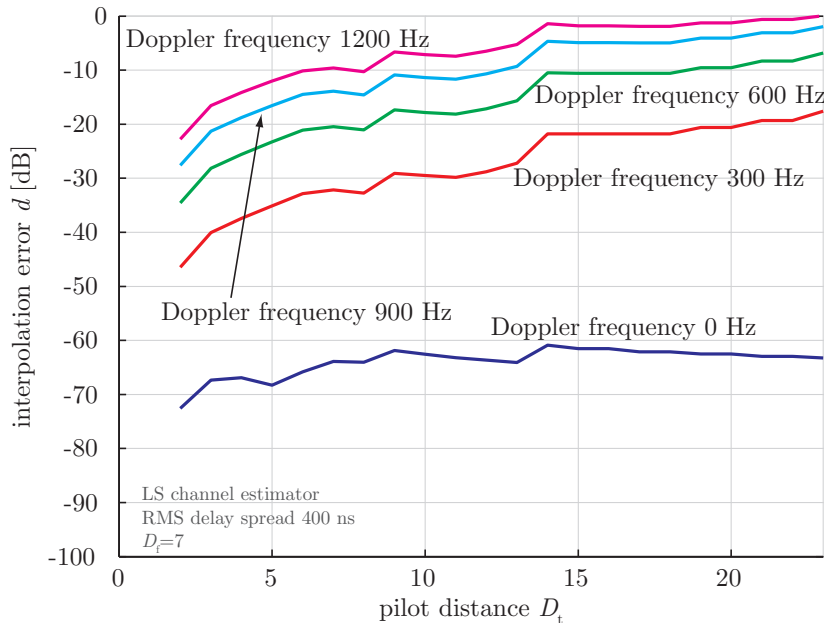


Figure 5.4: Interpolation error versus pilot-symbol distance D_t with a fixed pilot-symbol distance $D_f = 7$ for various values of Doppler frequencies with RMS delay spread of 400 ns. The interpolation error grows with increasing Doppler frequency and also with increasing pilot-symbol distance D_t .

Figure 5.5 illustrates the behavior of the interpolation error $d(D_f, D_t, \mathbf{R}_h)$ as a function of the pilot-symbol distance D_f at a fixed pilot-symbol distance $D_t = 7$ for RMS delay spreads between 0 and 800 ns with a Doppler frequency of 0 Hz. The interpolation error becomes more significant with increasing pilot-symbol distance and with increasing RMS delay spread. Note that for typical values of RMS delay spread up to 800 ns the interpolation saturation stays below -20 dB. Thus, at a

typical operational point, the interpolation error caused by frequency selectivity of a channel is smaller than the noise dependent part of the MSE.

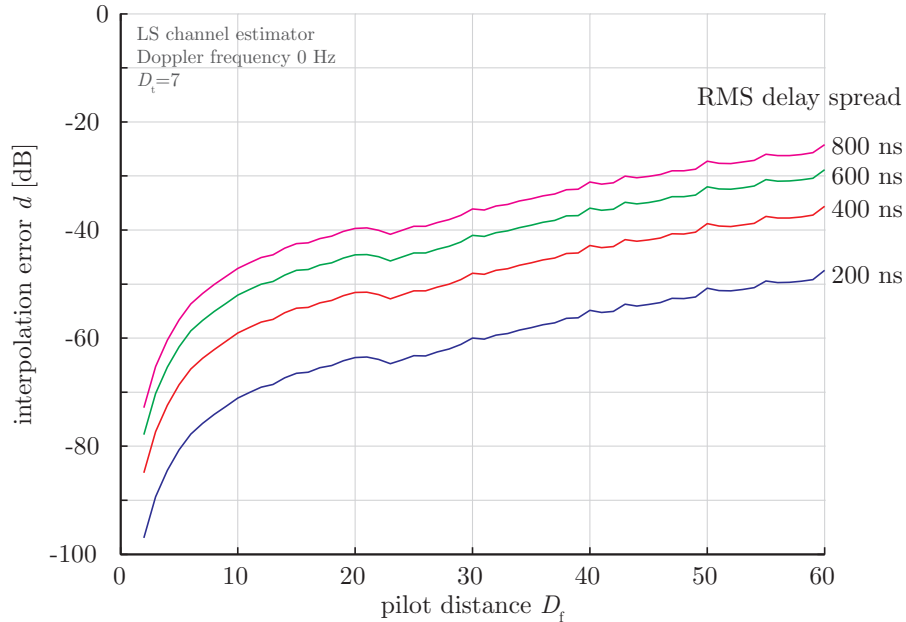


Figure 5.5: Interpolation error versus pilot-symbol distance D_f with a fixed pilot-symbol distance $D_t = 7$ for various values of RMS delay spreads with a Doppler frequency of 0 Hz. The interpolation error grows with increasing RMS delay spread and also with increasing pilot-symbol distance D_f .

At this point, it is possible to analytically express the performance of a linear channel estimator as a function of D_f and D_t for diamond-shaped pilot-symbol patterns. With this knowledge it is possible to maximize the post-equalization SINR in Equation (3.41) simply by maximizing the power allocation function in Equation (3.42) [43]. However, the optimal values of D_f and D_t and the optimal power distribution between the pilot- and the data-symbols cannot be found exclusively by maximizing the post-equalization SINR. Such an approach leads to a solution with minimum distances between adjacent pilot-symbols in the time and frequency directions, which would decrease the available bandwidth for data transmission. Therefore, another cost function is required that includes a penalty due to the bandwidth occupied by the pilot-symbols. The constrained channel capacity is thus a natural choice for the new cost function since it provides a more accurate estimate of the expected throughput than capacity [88, 89]

$$\mathcal{C} = B_s \sum_{l=1}^{N_l} \sum_k \log_2(1 + \gamma_{l,k}), \quad (5.1)$$

where B_s is the bandwidth utilized for the data transmission of a subcarrier and $\gamma_{l,k}$

is the post-equalization SINR at a layer l and a subcarrier k . The second sum in the above equation is a sum over all subcarriers carrying data-symbols.

The constrained capacity in Equation (5.1) is realistic as a waterfilling solution for a temporally changing channel is not feasible. Note also that for typically measured frequency selective MIMO channels the difference between the waterfilling solution (capacity) and the proposed constrained version is very small [90]. The impact of precoding matrices can be included in the channel estimation, as we consider here. Variable γ_l represents the instantaneous post-equalization SINR. However, Equation (5.1) cannot be directly utilized as a cost function, since it would require the knowledge of the instantaneous channel matrix and its estimation error. These are however not available and thus we utilize an ergodic capacity in terms of its expectation value. Such ergodic capacity requires the a-priori knowledge of statistics and is in general difficult to evaluate. However, its upper bound [91, 92] obtained by applying Jensen's inequality when inserting the mean post-equalization SINR Equation (3.45) in the constrained capacity expression Equation (5.1) (for more details see Appendix E), results in

$$\mathcal{C} \leq \bar{\mathcal{C}}, \quad (5.2)$$

$$\bar{\mathcal{C}} = B(D_f, D_t) \log_2(1 + \bar{\gamma}), \quad (5.3)$$

$$= B \log_2(1 + f_{\text{pow}}(c_e, d, \sigma_d^2, \sigma_p^2, \sigma_n^2) \sigma_{\text{ZF}, \mathbf{G}}). \quad (5.4)$$

Due to simplicity reasons in the above equations, I omit the dependency of the variables $B(D_f, D_t)$, $c_e(D_f, D_t)$, and $d(D_f, D_t, \mathbf{R}_h)$ on the variables D_t , D_f , and \mathbf{R}_h in the above equations. The ultimate target from physical-layer perspective is to maximize throughput. However, throughput is very difficult if not impossible to track analytically [89], which would allow a low complexity solution. Therefore, an analytical performance measure is required that allows to predict throughput including channel estimation error. The presented upper bound of the constrained capacity fulfils these requirements.

5.1.1 Unit Power Distribution

In this section, the same average power to the pilot-symbols and to the data-symbols is assigned. This approach is referred to as unit power distribution among the pilot- and data-symbols. This allows to investigate a potential gain that can be achieved solely by adjusting the pilot pattern.

Assuming evenly distributed power among pilot- and data-symbol (i.e., $\sigma_d^2 = 1$ and

$\sigma_p^2 = 1$), I obtain from Equation (E.4)

$$\bar{C}(D_t, D_f) = B(D_f, D_t) \log_2(1 + f_{\text{pow}}(c_e, d, 1, 1, \sigma_n^2) \sigma_{\text{ZF}, \mathbf{G}}). \quad (5.5)$$

Due to simplicity reasons in the above equations, I omit the dependency of the variables $c_e(D_f, D_t)$ and $d(D_f, D_t, \mathbf{R}_h)$ on the variables D_t , D_f , and \mathbf{R}_h .

In order to design a pilot-symbol pattern that maximizes the upper bound of the constrained channel capacity with respect to the pilot-symbol distance in the frequency dimension D_f and in the time dimension D_t , I formulate the optimization problem as

$$\begin{aligned} & \underset{D_t, D_f}{\text{maximize}} && \bar{C}(D_t, D_f) \\ & \text{subject to} && B(D_f, D_t) \leq \text{constant}. \end{aligned} \quad (5.6)$$

To solve the above optimization problem, the cost function is maximized over all possible combinations of the variables D_t and D_f in order to find their optimal set.

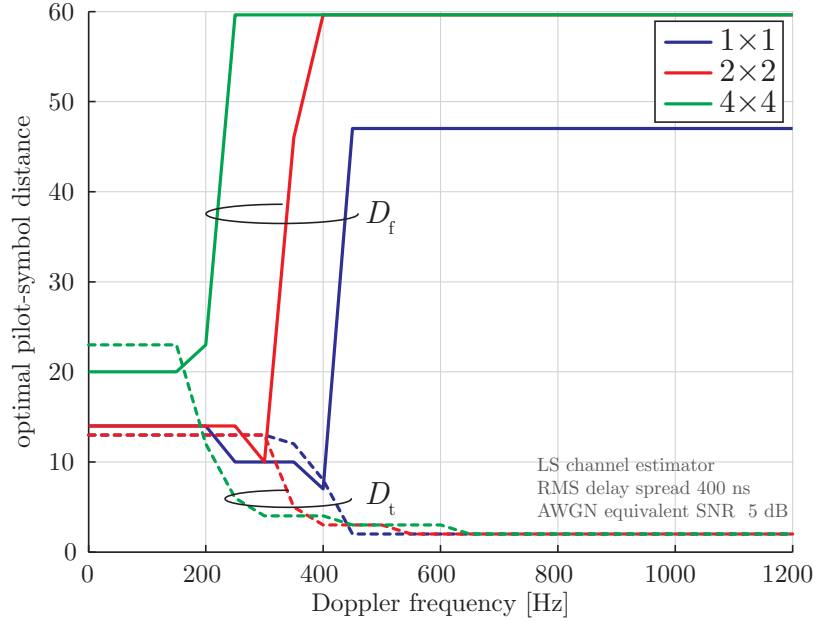


Figure 5.6: Optimal choice of the pilot-symbol distances in the frequency dimension D_f and in the time dimension D_t as a function of Doppler frequency. With an increasing Doppler frequency the pilot-symbol distance in the time dimension is decreasing and the distance in the frequency dimension is increasing. Overall, the amount of pilot-symbols is increasing with an increasing Doppler frequency.

To illustrate the optimal choice of the variables D_t and D_f , I consider an exemplarily case of a fixed RMS delay spread of 400 ns with a varying Doppler frequency.

Figure 5.6 illustrates an optimal choice for the parameters of the diamond-shaped pilot patterns as a function of the Doppler frequency for a fixed RMS delay spread of 400 ns for various MIMO setups at an AWGN equivalent SNR of 5 dB (for more details about AWGN equivalent SNR see Appendix F). In LTE terminology, an AWGN equivalent SNR of 5 dB corresponds to a CQI value seven. The distance between adjacent pilot-symbols in the time direction decreases with an increasing Doppler frequency for all considered MIMO setups. This is intuitive to understand, since with an increasing Doppler frequency also the time selectivity of a channel is increasing and therefore more pilot-symbols are required in order to obtain a precise channel estimate. At a Doppler frequency of 600 Hz, the distance between pilot-symbols in the time dimension D_t reaches the minimum distance allowed for all considered MIMO setups. On the other hand, the distance between pilot-symbols in the frequency direction D_f increases with increasing Doppler frequency. At a first sight, this might look unreasonable, since the frequency selectivity is fixed with a constant RMS delay spread of 400 ns and therefore a constant value of the variable D_f would be expected. Note, however, that with an increasing pilot density in the time direction and a fixed variable D_f , the overall pilot-symbol overhead would be extreme and only a small amount of data could be transmitted. Therefore, such a design strategy would lead to a low value of the constrained capacity. Therefore, the distance in the frequency direction is increasing with an increasing Doppler frequency.

In Figure 5.7, the optimal choice of the pilot pattern parameters versus RMS delay is shown. In this example, I fixed the Doppler frequency to 0 Hz, which corresponds to a time-invariant channel. The AWGN equivalent SNR value is fixed to 19.9 dB, which in LTE terminology corresponds to CQI 15. The distance in frequency direction decreases with an increasing value of RMS delay spread. Since with an increasing value of RMS delay spread the channel becomes more frequency-selective, more pilot-symbols in the frequency direction are required for a proper operation of the channel estimator. The distance in the time direction slightly decreases with an increasing RMS delay spread. This is caused mainly because an example of a time-invariant channel is considered. Thus, the channel is constant over individual OFDM symbols, i.e., the channel is perfectly correlated in the time direction. Therefore, in order to improve the channel estimation performance a denser pilot pattern in the time dimension is a good strategy due to its strong correlation.

Figure 5.8 shows the optimal choice of the distances between adjacent pilot-symbols in the time and frequency dimensions for a fixed Doppler frequency of 200 Hz and a fixed RMS delay spread of 400 ns. In general, two tendencies can be observed. First, with an increasing SNR, the distance between pilot-symbols in the time dimension is decreasing. Second, with an increasing SNR the distance in the frequency dimen-

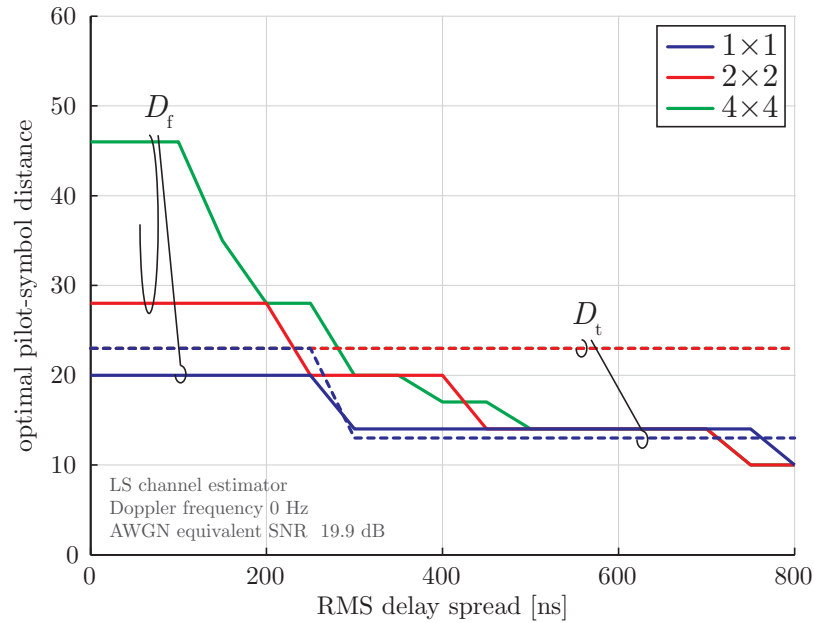


Figure 5.7: Optimal choice of the pilot-symbol distances in the frequency dimension D_f and in the time dimension D_t as a function of RMS delay spread for a fixed Doppler frequency and SNR. With an increasing RMS delay spread the pilot-symbol distance in the time dimension is decreasing and the distance in the frequency dimension too. Overall, the amount of pilot-symbols is increasing with an increasing value of RMS delay spread.

sion is increasing. Overall, the amount of pilot-symbols in the given transmission bandwidth is increasing with an increasing value of SNR. Let me discuss the blue solid line, representing the optimal choice of the pilot distance in the frequency dimension for an SISO system. In general, with an increasing value of SNR, a more reliable channel estimate is desired so that data-symbols out of high-order symbol alphabets can be successfully received. In the case of optimal pilot design with unit power distribution a more precise channel estimate can be obtained only via reserving more bandwidth for the pilot-symbols. Therefore, the optimal value of D_f for an SISO transmission system at SNR of 16 dB decreases, while the optimal D_t stays unchanged. With a further increasing value of SNR, the optimal choice of D_t decreases and the optimal D_f remains constant. But at SNR of 28 dB, the optimal D_f increases and the optimal D_t decreases. All of the mentioned changes with an increasing value of SNR, increase the amount of the total pilot-symbols.

The following trends can be identified when designing optimal pilot patterns with unit power allocation among pilot- and data-symbols:

- The optimal amount of pilot-symbols grows with an increasing value of Doppler frequency.
- With an increasing Doppler frequency, the optimal distance between pilot-symbols

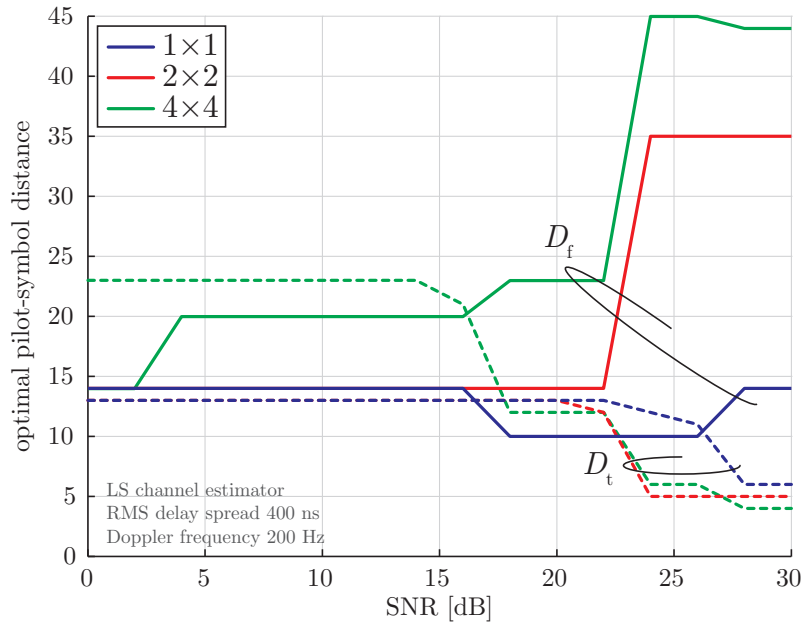


Figure 5.8: Optimal choice of the pilot-symbol distances in the frequency dimension D_f and in the time dimension D_t as a function of SNR for a fixed Doppler frequency and RMS delay spread. With an increasing SNR the pilot-symbol distance in the time dimension is decreasing and the distance in the frequency dimension is increasing. Overall, the amount of pilot-symbols is increasing with an increasing value of SNR.

in the time dimension decreases, whereas the optimal distance in the frequency dimension increases in order to compensate the constrained capacity loss caused by dense pilot-symbols in the time dimension.

- The optimal amount of pilot-symbols grows with an increasing value of RMS delay spread.
- With an increasing RMS delay spread, the optimal distance between pilot-symbols in the frequency dimension decreases. The optimal distance in the time dimension slightly decreases with an increasing value of RMS delay spread in order to improve channel estimation performance.
- The optimal amount of pilot-symbols grows with an increasing SNR value.

Simulation Results

In the following, I present throughput simulation results and compare the performance of two competitive wireless transmission systems in order to quantify the performance gain provided by optimal pilot patterns compared to conventional fixed pilot patterns. The first system utilizes LTE compliant pilot patterns for the purposes of channel estimation. The second system is the same in all parameters as

the first system except for the pilot patterns. It utilizes optimal pilot patterns with unit power distribution among pilot- and data-symbols. Table 5.1 shows the most important parameters of the simulations. In order to generate channels with an arbitrary RMS delay spread, I utilized the model presented in [93]. For generating channels with an arbitrary Doppler spread, I utilized the modified Rosa Zheng model, presented in the appendix of [53].

Table 5.1: Simulator settings for optimal pilot patterns with unit power distribution.

Parameter	Value
Bandwidth	1.4 MHz
Number of data subcarriers	72
FFT size	128
CP duration	$\approx 4.76 \mu\text{s}$
Number of transmit antennas	1, 2, 4
Number of receive antennas	1, 2, 4
Receiver type	ZF
Transmission mode	Open-loop spatial multiplexing

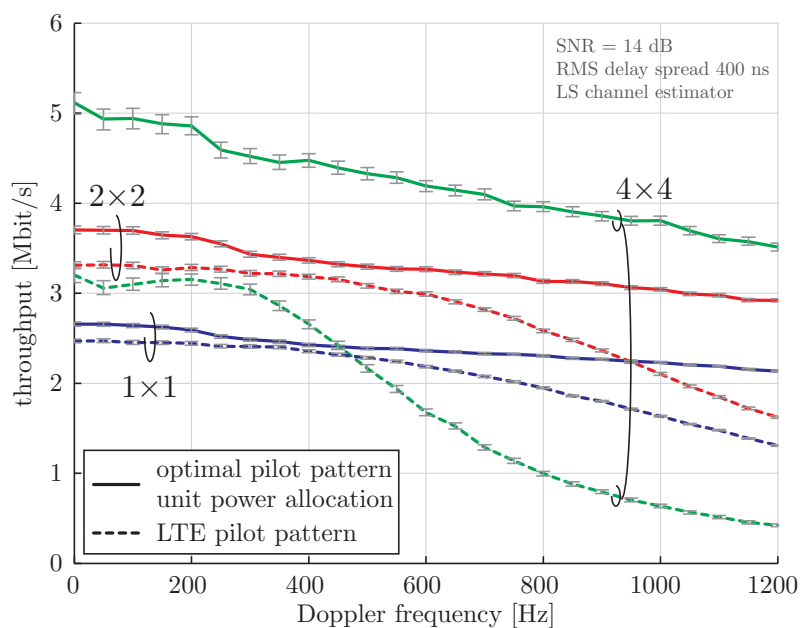
Figure 5.9(a) illustrates throughput as a function of Doppler frequency for various MIMO setups at a fixed SNR value of 14 dB and a fixed RMS delay spread of 400 ns. The throughput of the system with LTE pilot patterns is approximately constant up to a certain value of Doppler frequency and then begins to degrade. This Doppler frequency value shifts to lower values as the number of transmit antennas is increased. The performance degradation also worsens with an increasing number of transmit antennas. The performance drop with an increasing Doppler frequency of a 4×4 system with LTE pilot pattern is mainly caused due to the pilot pattern placed on the third and fourth transmit antennas that does not allow a precise estimation of time-variant channels. The systems utilizing optimal pilot patterns always outperform the corresponding LTE systems. Let me consider a 1×1 transmission system. The throughput approximately linearly decreases with an increasing Doppler frequency. At around a Doppler frequency of 350 Hz, a gap between the two competing systems is the smallest from the considered scenarios and therefore I can conclude that the LTE pilot pattern for a single transmit antenna is close to an optimal pilot pattern with unit power distribution at a Doppler frequency of 350 Hz. The performance of the remaining antenna setups with optimal pilot patterns behaves in a similar manner: approximately linear throughput loss with an increasing Doppler frequency. Note that the throughput loss is more significant as the number of transmit antennas is increased. This is caused mainly by the fact that for a higher amount of transmit antennas, there are more channel coefficients to estimate and therefore also more pilot-symbols are required. At Doppler frequencies around 950 Hz, an SISO system utilizing optimal pilot patterns outperforms a 2×2 MIMO system with the LTE pilot pattern. Thus, at high Doppler spreads optimal pilot

patterns allow to save hardware cost and complexity that are inherently connected with MIMO applications.

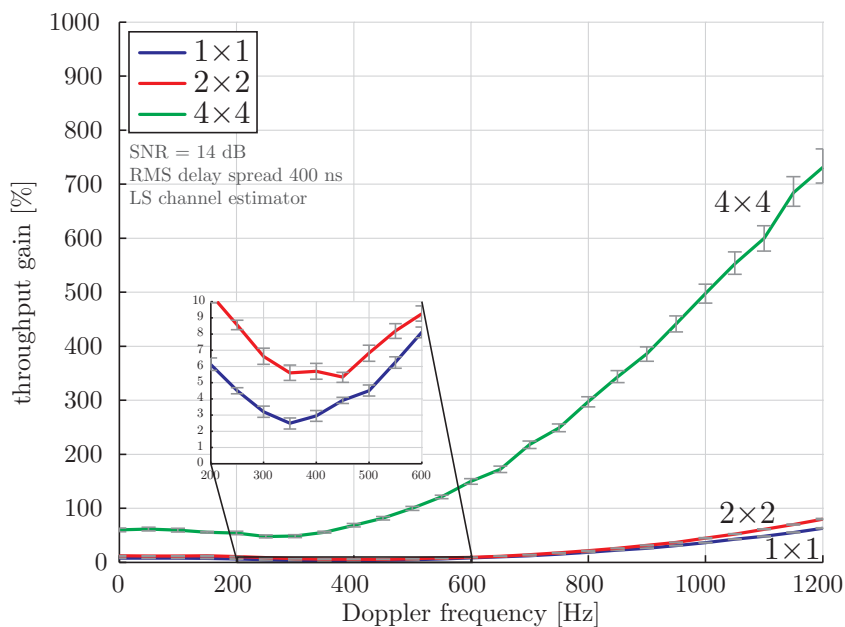
In Figure 5.9(b), the relative throughput gain in percent of a system utilizing optimal pilot-symbol patterns relative to its counterpart utilizing a standard LTE pilot-symbol pattern is shown versus Doppler frequency for a fixed SNR of 14 dB and a fixed RMS delay spread of 400 ns. As observed from Figure 5.9(a), the throughput gain reaches its maximum at the maximum Doppler frequency. The potential throughput gains offered by optimal pilot patterns grow with increasing number of transmit antennas. In the case of four transmit antennas, it reaches up to almost 800% compared to the corresponding 4×4 LTE system. Such a high gain is caused mainly due to the LTE pilot design for four transmit antennas failing to estimate time-variant channels. In case of two transmit antennas, the gain reaches up to 80% and in case of a single transmit antenna up to 65%, respectively. Let me focus on the blue curve, representing an SISO system. The throughput gain compared to its LTE counterpart, is typically larger than 5%. Remember that LTE with this antenna configuration utilizes 4.7% of the bandwidth for the pilot-symbols. Thus, I can conclude, the throughput gain does not solely come from the fact that pilot-symbols occupy less bandwidth, but also because the channel estimate obtained is of higher precision than when utilizing LTE pilot patterns. The same line of arguments is valid also for the remaining antenna configurations.

Figure 5.10(a) illustrates throughput versus SNR for various MIMO setups utilizing either LTE pilot patterns or optimal pilot patterns with unit power distribution among data- and pilot-symbols. In this simulation, the RMS delay spread and the Doppler frequency are fixed to 400 ns and 200 Hz, respectively. Considering the dashed curves, which represent the systems utilizing LTE pilot patterns, a typical behavior can be observed: increasing the number of transmit and receive antennas boosts the overall throughput of the systems. However, at a low SNR value of 0 dB, it is more beneficial to transmit only with a single antenna, because the potential multiplexing benefits cannot be exploited at such a low SNR value. The solid lines represent systems utilizing optimal pilot patterns. These always outperform their corresponding counterparts. Note that for higher values of the Doppler frequency, the 4×4 MIMO system with LTE pilot pattern performs poorly, due to the LTE pilot design on the third and fourth transmit antennas. The standard compliant pilot pattern enables to estimate time-variant channels with a very poor quality [94].

To quantify the performance gain achieved due to the optimal pilot patterns, let me consider Figure 5.10(b). In this figure, the relative throughput gain in percent of a system with optimal pilot pattern relative to an LTE system versus SNR is shown. The gain is decreasing with increasing SNR. Higher gains are obtained for higher MIMO schemes. Let me consider the blue solid curve representing gain of an SISO



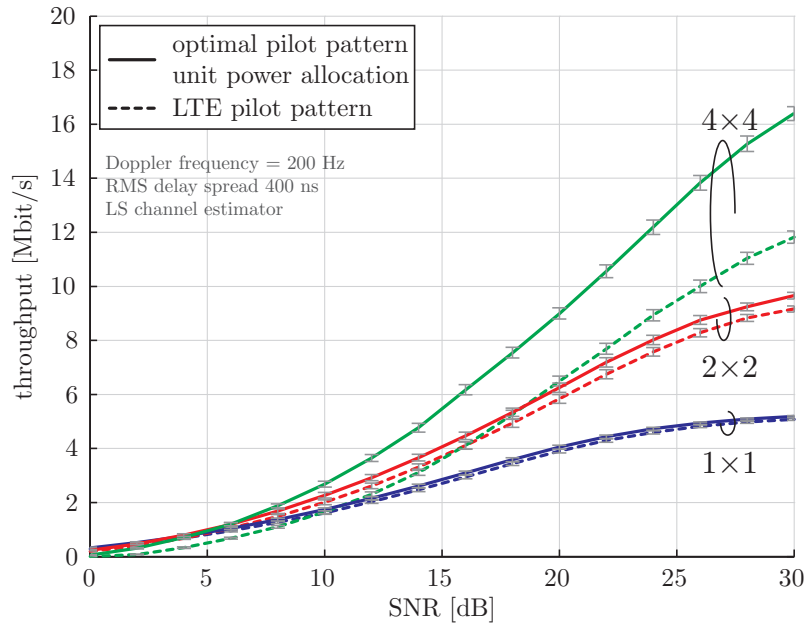
(a) Throughput as a function of Doppler frequency: Dashed lines represent systems utilizing LTE pilot patterns. Solid lines represent systems utilizing optimal pilot patterns with unit power distribution.



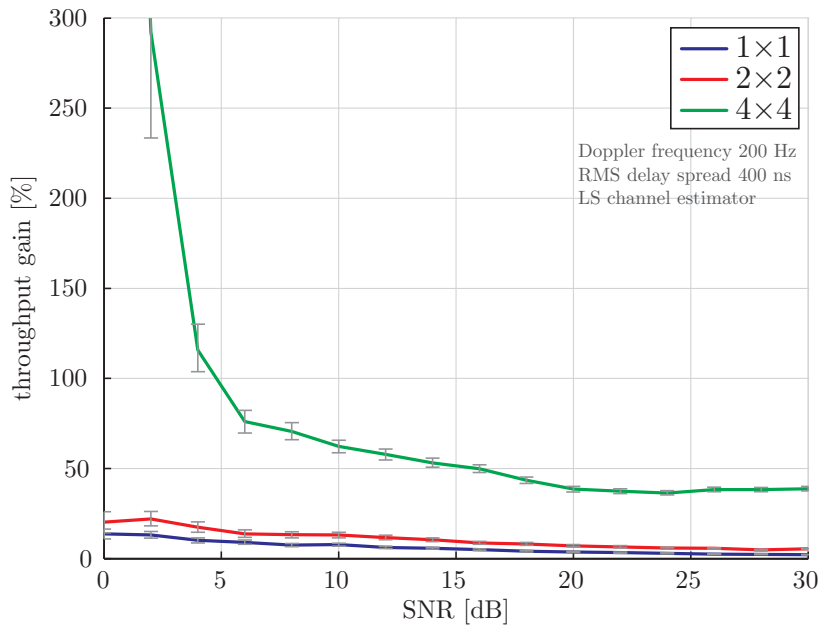
(b) Throughput gain of a system utilizing an optimal pilot pattern with unit power distribution compared to an LTE compliant system as a function of Doppler frequency.

Figure 5.9: Performance of optimal pilot patterns with unit power distribution versus Doppler frequency for a fixed SNR of 14 dB and a fixed RMS delay spread of 400 ns.

5. OPTIMAL PILOT-SYMBOL PATTERN DESIGN



(a) Throughput as a function of SNR: Dashed lines represent systems utilizing LTE pilot patterns. Solid lines represent systems utilizing optimal pilot patterns with unit power distribution.



(b) Throughput gain of a system utilizing an optimal pilot pattern with unit power distribution compared to an LTE compliant system as a function of SNR.

Figure 5.10: Performance of optimal pilot patterns with unit power distribution versus SNR for a Doppler frequency of 200 Hz and a fixed RMS delay spread of 400 ns.

system. At a high SNR value, it reaches approximately 3%. At this SNR value a highly precise channel estimate is required so that data-symbols out of high order symbol alphabets can be properly equalized. The SISO LTE pilot pattern allows to estimate the channel with such a high precision, but a further 3% of the pilot-symbols can be saved and utilized for the data transmission. The gain for a 4×4 system is significantly higher than for the other presented MIMO systems. This is caused by the pilot-symbol pattern provided by the LTE standard for four transmit antennas. Pilot-symbols placed on the third and fourth transmit antennas do not allow to estimate time-variant channels with high precision, thus the performance of such a system is limited. This limitation is even more severe at higher Doppler spreads. The throughput gain for a 4×4 system at low SNR is infinitely high, since the LTE system at this SNR values has zero throughput, but the system utilizing optimal pilot patterns delivers non-zero throughput at the considered SNR value.

5.1.2 Optimal Power Distribution

In this section, I include power distribution among pilot- and data-symbols into the optimal pilot-symbol pattern design framework. By doing so, it is possible to adjust the power at the pilot-symbols and obtain highly precise channel estimates at the pilot-symbols and therefore decrease the noise-dependent part of the channel estimation error.

I consider a case in which the entire available power is utilized for the transmission, and therefore, σ_d^2 and σ_p^2 can be expressed in terms of the variable p_{off} defined as the ratio between the power of the pilot-symbols and of the data-symbols

$$p_{\text{off}} = \frac{\sigma_p^2}{\sigma_d^2}. \quad (5.7)$$

Consequently, the variables σ_d^2 and σ_p^2 can be expressed in terms of the variable p_{off} and the numbers of the pilot- and data-symbols as

$$\sigma_p^2 = \frac{N_p + N_d}{\frac{N_d}{p_{\text{off}}} + N_p} = p_{\text{off}} \sigma_d^2, \quad (5.8)$$

$$\sigma_d^2 = \frac{N_p + N_d}{N_d + N_p p_{\text{off}}}. \quad (5.9)$$

Therefore, the cost function in Equation (5.5) depends only on the triple $(p_{\text{off}}, D_t, D_f)$ for a given channel autocorrelation matrix \mathbf{R}_h .

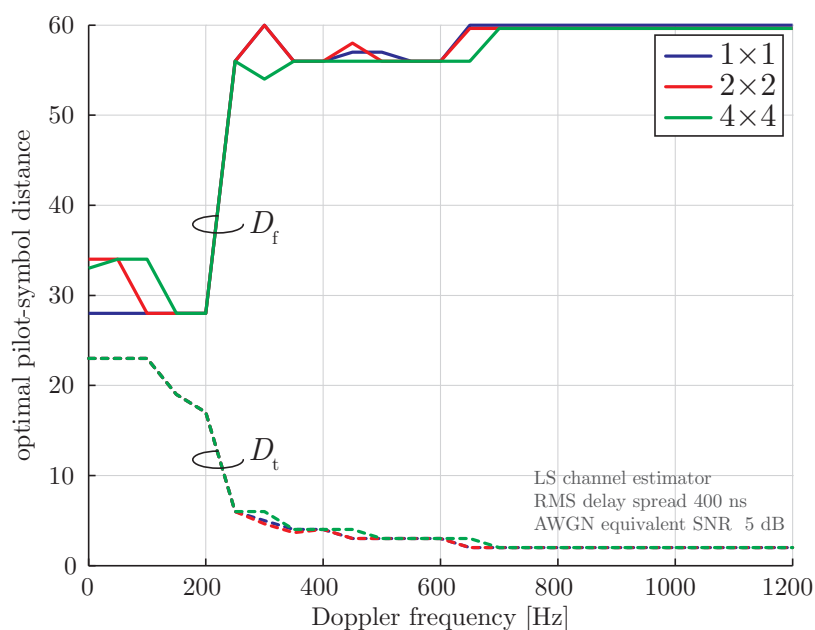
I formulate the optimization problem as

$$\begin{aligned} & \underset{p_{\text{off}}, D_t, D_f}{\text{maximize}} && \bar{C}(p_{\text{off}}, D_t, D_f) \\ & \text{subject to} && N_d \sigma_d^2 + N_p \sigma_p^2 = \text{constant} \\ & && B(D_f, D_t) \leq \text{constant} \end{aligned} \tag{5.10}$$

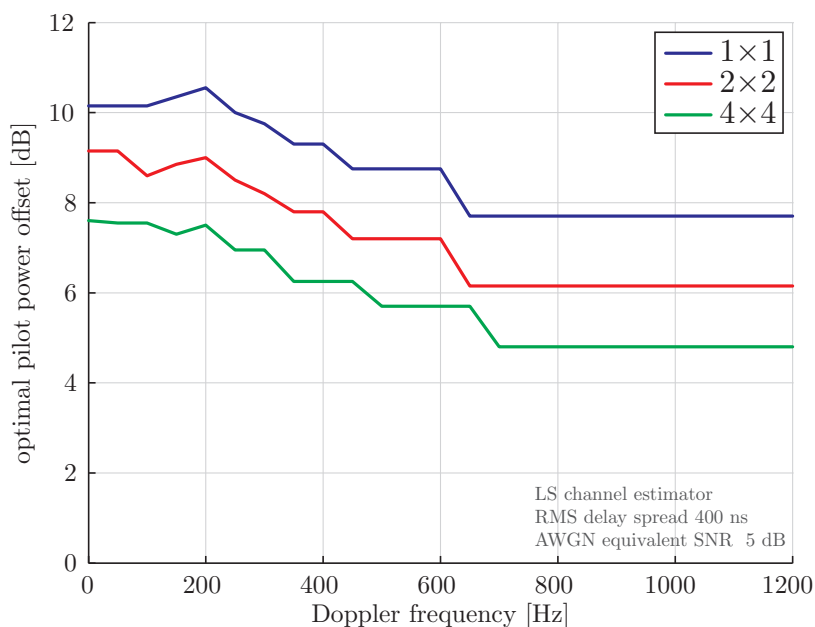
To solve the above optimization problem, I first find numerically the optimal value of p_{off} for all possible combinations of the variables D_f and D_t . Consequently, I maximize the cost function over the variables D_t and D_f in order to find the optimal triple p_{off} , D_t , and D_f .

Figure 5.11(a) and Figure 5.11(b) illustrate the optimal choice of the pilot pattern design variables as a function of Doppler frequency for a fixed AWGN equivalent SNR of 5 dB. Compared to the previous case of unit power distribution, the case of optimal power distribution is more complicated to understand. Let me recall that an MSE of a linear channel estimator consists of a noise dependent part and a noise independent part, also called interpolation error. When increasing the pilot-symbol power, only the noise dependent part is decreased. Therefore, when trying to find an optimal power offset value for a given values of the noise variance and the variables D_t and D_f , the power at the pilot-symbols is increased until the noise dependent part of the MSE is negligible compared to the interpolation error. At such a point, a further power increase does not deliver a further improvement in terms of MSE. Therefore, compared to the previous case of equal power distribution, when a more reliable channel estimate is required, it can be achieved not only by increasing the amount of the pilot-symbols but also by increasing the power at the pilot-symbols depending on what is more beneficial in terms of the cost function. Figure 5.11(a) shows the optimal choice of the pilot-symbol distances versus Doppler frequency for a constant RMS delay spread of 400 ns and a fixed AWGN equivalent SNR of 5 dB. The distance in the time direction is decreasing as the Doppler frequency increases, whereas the optimal distance in the frequency direction is increasing with an increasing Doppler spread. At high Doppler frequencies, the optimal choice of the pilot patterns is the same as in the case of equal power distribution for two and four transmit antennas. However, in the case of optimal power distribution more power is transmitted at the pilot-symbols than in the case of unit power distribution.

Figure 5.11(b) shows the optimal choice of power offset as a function of Doppler frequency for a fixed value of RMS delay spread. For all considered MIMO setups, optimal power offset decreases with increasing Doppler frequency. As it is shown in Figure 5.4, the interpolation error is increasing with an increasing Doppler frequency. Thus, at higher Doppler frequencies the point at which a further power increase at the pilot-symbols does not improve the MSE, is reached with a smaller amount of



(a) Optimal choice of the pilot-symbol distances as a function of Doppler frequency for optimal power distribution. With an increasing Doppler frequency the pilot symbol distance in the time dimension is decreasing and the distance in the frequency dimension is increasing. Overall, the amount of pilot-symbols is increasing with an increasing Doppler frequency.



(b) Optimal power offset between pilot- and data-symbol as a function of Doppler frequency for the case including also optimal power distribution. With an increasing Doppler frequency the power offset is decreasing.

Figure 5.11: Optimal pilot pattern parameters versus Doppler frequency.

power.

In Figure 5.12(a), the optimal choice of the pilot pattern parameters versus RMS delay spread is shown. In this example, the Doppler frequency is fixed to 0 Hz. This case corresponds to a block fading scenario with time-invariant channels. Since the channel is not changing over time, the optimal pilot distance in the time dimension is chosen as the maximum distance allowed by the optimization problem for all considered MIMO setups. This parameter choice corresponds to a single pilot-symbol in the time dimension. The pilot distance in the frequency dimension is decreasing as the RMS delay spread grows. With an increasing value of RMS delay spread the frequency-selectivity of the channel becomes stronger, thus more pilot-symbols in the frequency direction are required.

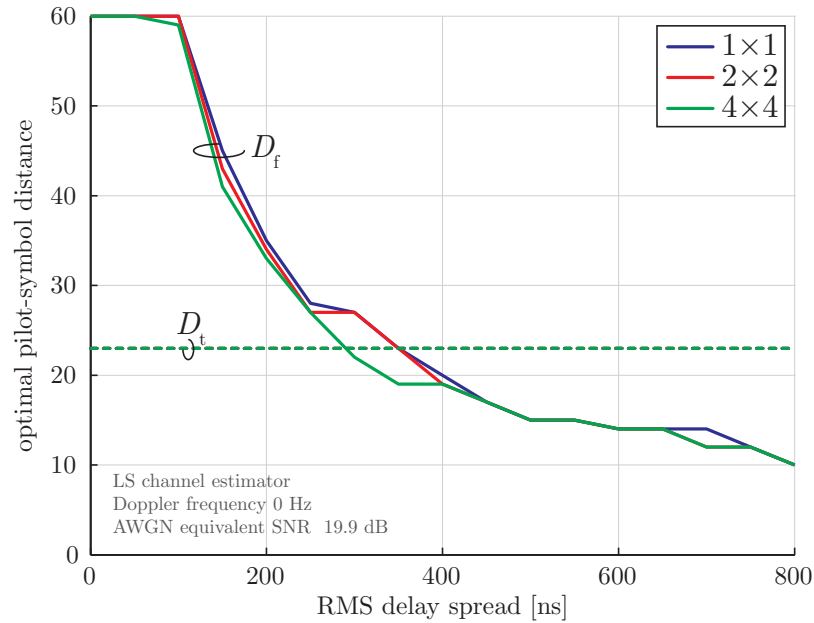
Figure 5.12(b) illustrates the optimal choice of the power offset versus RMS delay spread for a fixed SNR value and a fixed Doppler frequency of 0 Hz. The optimal power offset decreases with an increasing value of RMS delay spread.

The optimal choice of the triple D_f , D_t , and p_{off} versus SNR is shown in Figure 5.13(a) and in Figure 5.13(b). At a first sight, the optimal choice of the distances between pilot-symbols appears counterintuitive. In general, as in the case of the unit power distribution, the amount of pilot-symbols is increasing with an increasing value of SNR. At low SNR values, the increase of the amount of pilot-symbols originates from the decreasing distance in the frequency dimension. Between SNR values of 15 dB and 20 dB a significant reduction of the distance in the time dimension occurs and in order to compensate the capacity loss if the variable D_f would stay constant, the optimal distance in the frequency dimension is extended. Afterwards, with an increasing SNR the variable D_f decreases again to allow for a more accurate channel estimation.

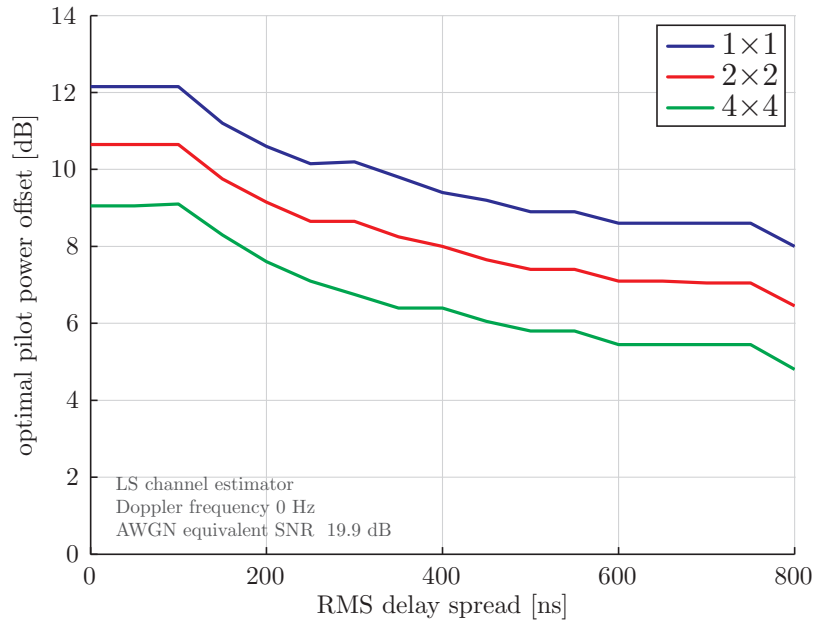
The behavior of the optimal power offset is shown in Figure 5.13(b) as a function of SNR for a fixed RMS delay spread of 400 ns and a fixed Doppler frequency of 200 Hz. The main function of the increased power of the pilot-symbols is to reduce a noise dependent portion of the channel estimation MSE. This, naturally, decreases with increasing SNR and therefore also the optimal choice of the power offset is decreasing with increasing SNR.

The following trends can be identified when designing optimal pilot patterns with optimal power allocation among pilot- and data-symbols:

- The optimal amount of pilot-symbols grows with an increasing value of Doppler frequency.
- With an increasing Doppler frequency, the optimal distance between pilot-symbols in the time dimension decreases, whereas the optimal distance in the frequency dimension increases in order to compensate the constrained capacity loss caused

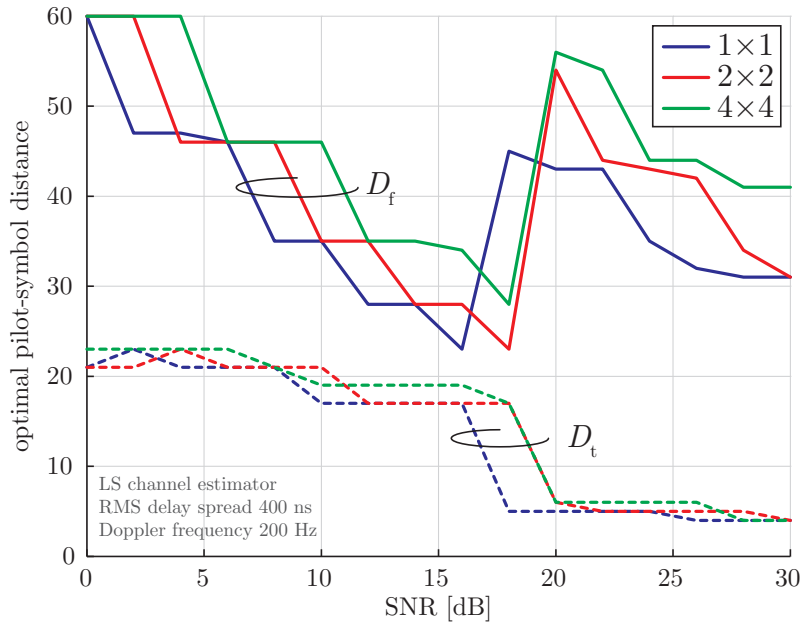


(a) Optimal choice of the pilot pattern parameters as a function of RMS delay spread for optimal power distribution. With an increasing RMS delay spread the pilot symbol distance in the frequency dimension is decreasing and the distance in the time dimension is constant (it is the same for all considered MIMO setups). Overall, the amount of pilot-symbols is increasing with an increasing RMS delay spread.

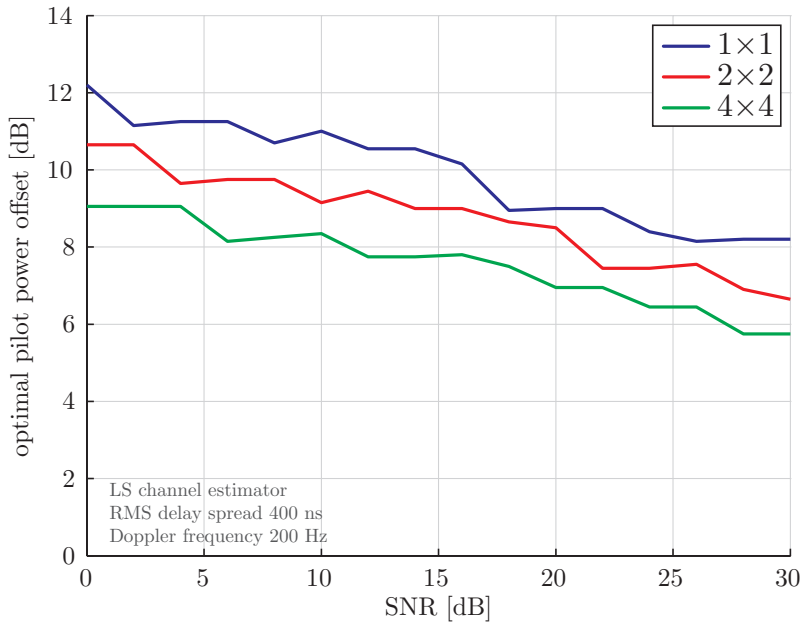


(b) Optimal power offset between pilot- and data-symbol as a function of RMS delay spread for the case including also optimal power distribution. With an increasing RMS delay spread the power assigned to the pilot-symbols is decreasing.

Figure 5.12: Optimal pilot pattern parameters versus RMS delay spread.



(a) Optimal choice of the pilot-symbol distances in the frequency dimension D_f and in the time dimension D_t as a function of SNR for a fixed Doppler frequency and RMS delay spread. With an increasing SNR the pilot symbol distance in the time dimension is decreasing and the distance in the frequency dimension is increasing. Overall, the amount of pilot-symbols is increasing with an increasing value of SNR.



(b) Optimal power offset between pilot- and data-symbol as a function of SNR. Since with an increasing value of SNR less noise is present, the power assigned to the pilot-symbols is decreasing for increasing SNR.

Figure 5.13: Optimal pilot pattern parameters versus SNR.

by dense pilot-symbols in the time dimension.

- The optimal amount of power radiated at pilot-symbols decreases with an increasing Doppler frequency.
- The optimal amount of pilot-symbols grows with an increasing value of RMS delay spread.
- The pilot-symbol distance in the frequency dimension grows as the value of RMS delay spread grows.
- The optimal amount of power radiated at pilot-symbols decreases with an increasing RMS delay spread.
- The optimal amount of pilot-symbols grows with increasing SNR.
- The optimal amount of power radiated at pilot-symbols decreases with increasing SNR.

Simulation Results

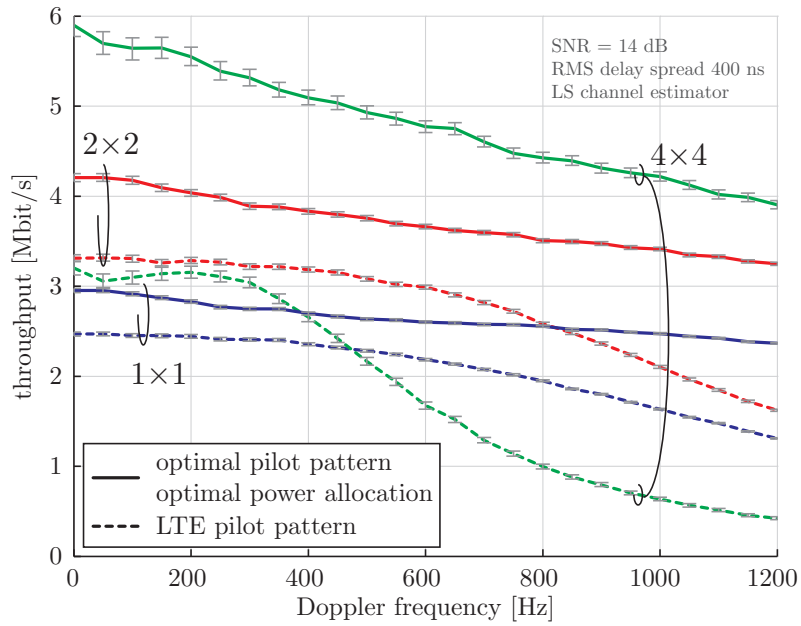
In the following, I present throughput simulation results for the optimal pilot pattern design including optimal power distribution among pilot- and data-symbols. I present throughput simulations for two competitive systems that are identical in all parameters except the utilized pilot patterns. The tested system utilizes the proposed optimal pilot patterns including optimal power distribution. I compare the performance of such a system to a benchmark system that utilizes pilot patterns provided by the LTE standard. Furthermore, I compare the performance of systems utilizing optimal pilot patterns with and without optimal power distribution. The most important simulation settings are presented in Table 5.2.

Table 5.2: Simulator settings for optimal pilot patterns with optimal power distribution.

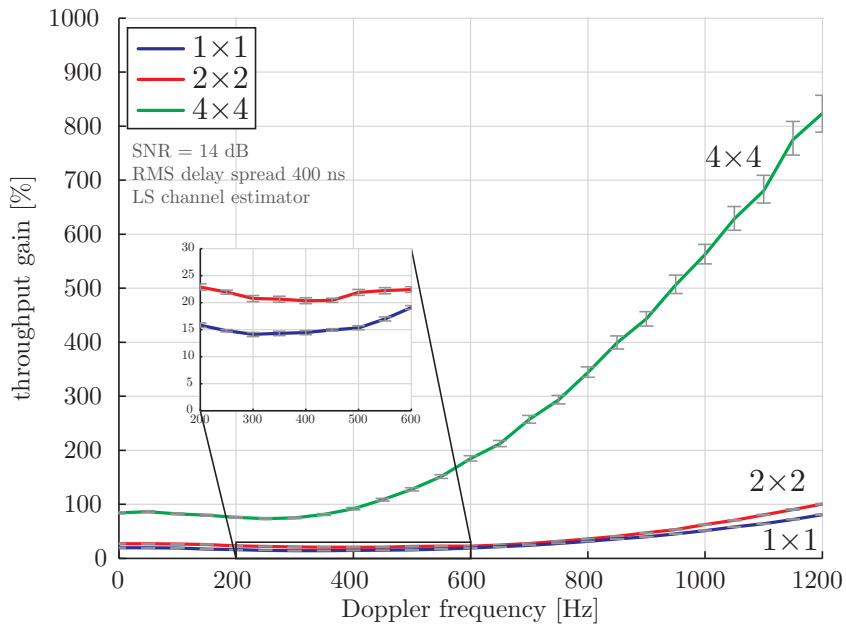
Parameter	Value
Bandwidth	1.4 MHz
Number of data subcarriers	72
FFT size	128
CP duration	$\approx 4.76 \mu\text{s}$
Number of transmit antennas	1, 2, 4
Number of receive antennas	1, 2, 4
Receiver type	ZF
Transmission mode	Open-loop spatial multiplexing

Figure 5.14(a) presents throughput simulation results versus Doppler frequency for various MIMO setups at a fixed SNR of 14 dB and a fixed RMS delay spread of 400 ns. The dashed lines represent a transmission system utilizing pilot patterns defined by the LTE standard for various numbers of transmit antennas. The solid lines represent the competing systems utilizing optimal pilot patterns with optimal power

5. OPTIMAL PILOT-SYMBOL PATTERN DESIGN



(a) Throughput as a function of Doppler frequency: Dashed lines represent systems utilizing LTE pilot patterns. Solid lines represent systems utilizing optimal pilot patterns with optimal power distribution.



(b) Throughput gain of a system utilizing an optimal pilot pattern with optimal power distribution compared to an LTE compliant system.

Figure 5.14: Performance of optimal pilot patterns with optimal power distribution versus Doppler frequency for a fixed SNR of 14 dB and a fixed RMS delay spread of 400 ns.

distribution among pilot- and data-symbols. The system with optimal pilot patterns outperforms the corresponding benchmark system in the considered Doppler spread range. With increasing Doppler frequency the gap between an LTE system and the competing system widens. The throughput increase grows with an increasing number of transmit antennas. Similar to the case of optimal pilot patterns with unit power distribution, the throughput loss of the optimal systems is approximately linear with an increasing Doppler frequency. The loss is more significant as the number of transmit antennas is increased. A comparison of these results with the results from Figure 5.9(a) yields a significant improvement of the system utilizing also optimal power distribution and not only optimal pilot patterns. I investigate the achieved performance gain in Figure 5.15.

In order to quantify the improvement of the performance when utilizing optimal pilot patterns with optimal power distribution, I present the relative throughput gain when compared with the LTE standard compliant transmission systems in Figure 5.14(b). As observed from the throughput figure, for a single and two transmit antennas, the gain relative to the LTE system is approximately constant up to a Doppler frequency of 600 Hz, afterwards it begins to grow with increasing Doppler frequency. For an SISO transmission system, the gain begins at around 20% and reaches up to 80%. For the system utilizing two transmit antennas, the gain begins at a value of approximately 30% and grows up to a value of 100%. As in the previous cases, the system utilizing four transmit antennas yields larger throughput gains, in a low mobility scenario at a Doppler frequency 0 Hz, the gain is around 85% and its grows up to 850% in a high mobility scenario at a Doppler frequency of 1200 Hz. For all considered MIMO setups, the achieved gain is larger than the amount of pilot-symbols utilized for channel estimation by the LTE standard. Thus, I can conclude that the gain does not only come from having more resources available for the data transmission, but is also due to a smart rearrangement of the pilot-symbols; the channel estimate is more precise than utilizing the standard compliant pilot pattern.

In order to show the significance of the optimal power allocation among pilot- and data-symbols, in Figure 5.15 I present the throughput gain of transmission systems utilizing optimal pilot patterns with optimal power distribution relative to systems utilizing optimal pilot patterns with unit power distribution. In order not to cause a potential confusion, let me stress that these two systems utilize not only different power levels at their pilot-symbols but also different pilot patterns. In general, the systems with optimal power distribution utilize less bandwidth for the pilot-symbols than the system with unit power distribution, due to possibility to decrease the channel estimation MSE, when required, by two means, adjusting pilot density and their power. The systems with unit power distribution can decrease the MSE

only by modifying the pilot patterns. Let me first focus on the blue and red curves, representing systems with a single and two transmit antennas, respectively. The gain ranges between 10% and 20%. It slightly grows with increasing Doppler frequency. The gain with two transmit antennas is larger than for a single transmit antenna. The presented gains are consistent with results shown in Chapter 4. As in the previous cases, the behavior for the 4×4 transmission is different. It grows more significantly with an increasing Doppler frequency and reaches up to almost 100%.

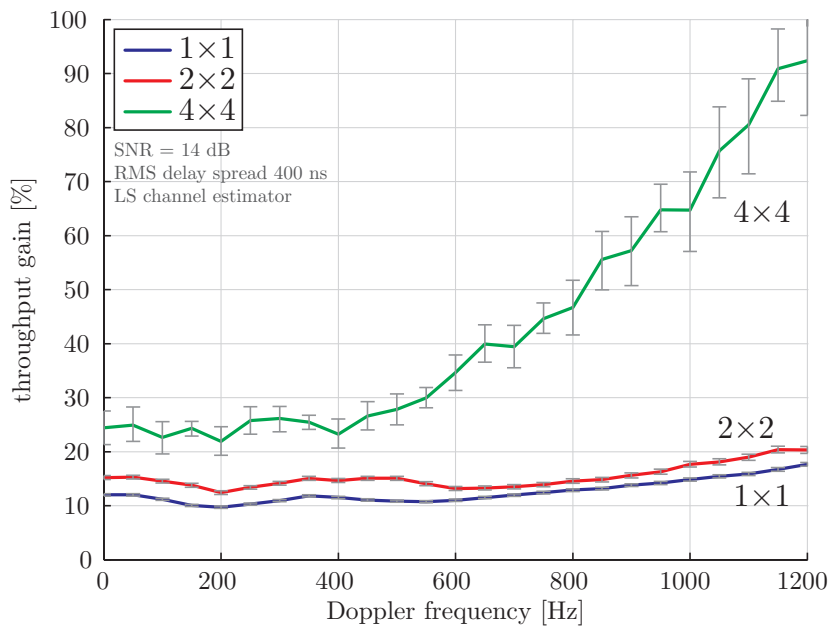


Figure 5.15: Throughput gain of a system utilizing an optimal pilot pattern with optimal power distribution compared to a system with optimal pilot pattern with unit power distribution, as a function of Doppler frequency for a fixed SNR of 14 dB and a fixed RMS delay spread of 400 ns.

In the following, I investigate the performance of the considered systems versus SNR for a fixed Doppler and RMS delay spreads. Figure 5.16(a) shows throughput for various MIMO setups for an RMS delay spread of 400 ns and a Doppler frequency of 200 Hz. The dashed lines represent systems utilizing pilot patterns provided by LTE. The solid lines represent systems utilizing optimal pilot patterns with optimal power distribution. The optimal systems always outperform the LTE benchmark systems. For the 1×1 system, the throughput gain is approximately constant up to an SNR value of 20 dB. After this value, the gain becomes smaller when further increasing SNR. For the 2×2 MIMO setup, the system utilizing optimal pilot patterns outperforms the LTE system by an approximately constant throughput offset in the whole considered SNR range. The situation differs for a 4×4 system. In this case, the pilot pattern provided by LTE fails to estimate precisely enough time-variant channels and therefore the gap between the optimal system and the

LTE system widens with increasing SNR. Based on the behavior of the gap size, I can conclude that the LTE pilot patterns for a single and two transmit antennas are close to optimal for high SNR values. Note that these SNR values are far beyond a typical operation point. Thus, the LTE pilot patterns are designed for rather extreme and unrealistic situations in order to operate suboptimally but in a wide range of scenarios.

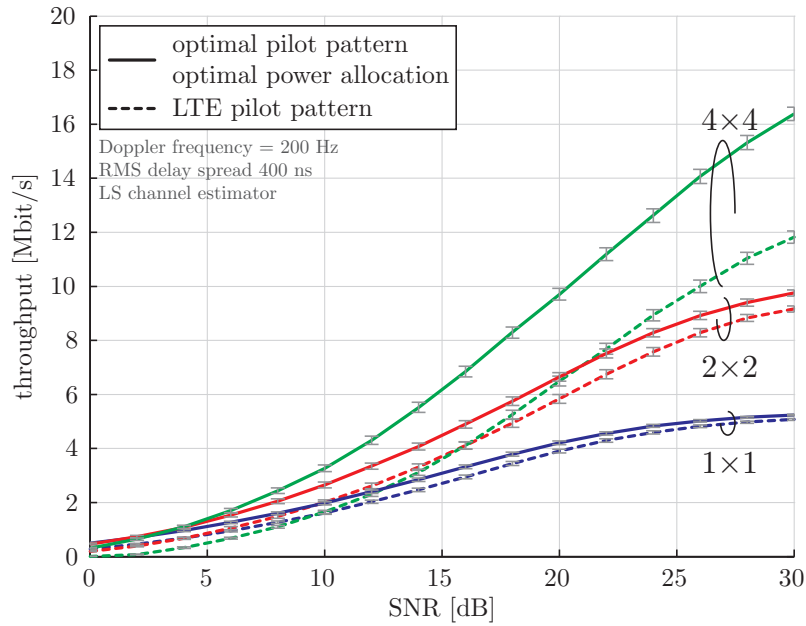
In Figure 5.16(b), the relative throughput gains of optimal systems with respect to pilot patterns and power distribution are shown and compared to their LTE counterparts. At low SNR value, the gains are relatively large and with increasing SNR they decrease. This is consistent with the previously stated finding that the LTE pilot patterns are designed for high SNR values. The gain is more significant for a higher number of transmit antennas. For an SISO system, the gain begins at 75% and decreases up to a value of 3.4% at an SNR of 30 dB. At such an operation point, a very precise channel state information is required in order to successfully transmit data-symbols out of high order symbol alphabets. The LTE pilot patterns provide such a precise channel state information but they require 3.4% more bandwidth than the optimal pilot patterns. For the MIMO setup with two antennas at both ends, the throughput gain begins at around 130% and decrease to a value of 6.5%. In the case of a 4×4 system, the gain at SNR of 0 dB is infinitely high, since the LTE system delivers zero throughput. At a high SNR value of 30 dB, the gain is around 40%.

The throughput gain of a system utilizing optimal pilot patterns with optimal power distributions compared to a system with optimal pilot patterns with unit power distribution is shown in Figure 5.17. The gain is shown for a fixed RMS delay spread of 400 ns and a fixed Doppler frequency of 200 Hz. These gains behave similar to the gains relative to LTE shown in Figure 5.16(b). The gain is larger for high MIMO orders. The gains decrease with an increasing SNR. The main difference is that the gains for all considered MIMO setups reach almost 0% at an SNR value of 30 dB.

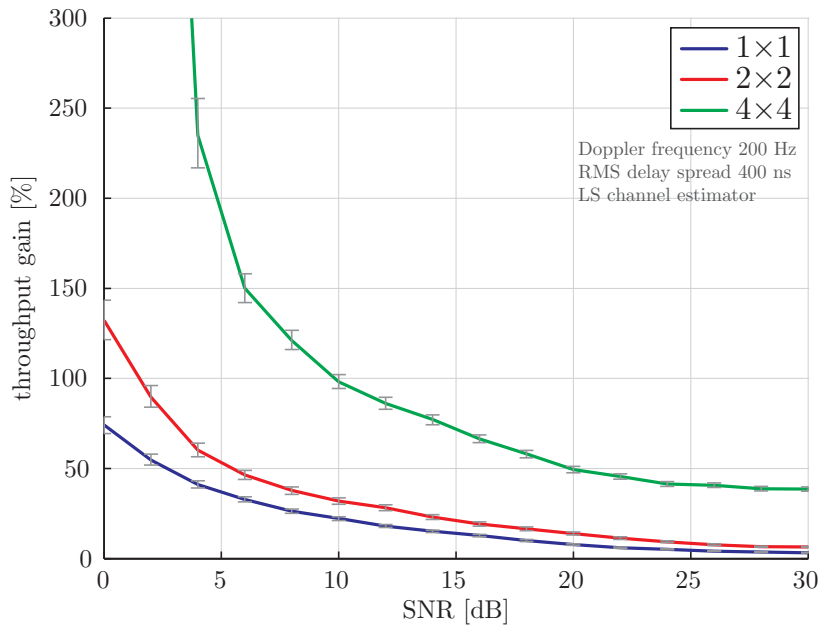
The sum of gains shown in Figure 5.17 and in Figure 5.10(b) results in gains of the optimal system presented in Figure 5.16(b). For low SNR values the main portion of the gains is due to the optimal power allocation, whereas the gains obtained at high SNR values are achieved due to the optimal pilot placement.

In Figure 5.18(a), throughput versus RMS delay spread for LMMSE and LS channel estimators for a time-invariant channel (at a Doppler frequency of 0 Hz) is shown. The throughput of all presented curves is approximately constant with a slight decrease when the RMS delay spread increases. The dashed lines represent transmission systems employing LTE pilot patterns. These system are always outperformed by the corresponding systems utilizing optimal pilot patterns (solid lines). The throughput gain when applying optimal pilot patterns compared to LTE pilot pat-

5. OPTIMAL PILOT-SYMBOL PATTERN DESIGN



(a) Throughput as a function of SNR: Dashed lines represent systems utilizing LTE pilot patterns. Solid lines represent systems utilizing optimal pilot patterns with optimal power distribution.



(b) Throughput gain of a system utilizing an optimal pilot pattern with optimal power distribution compared to an LTE compliant system, as a function of SNR.

Figure 5.16: Performance of optimal pilot patterns with optimal power distribution versus SNR for a fixed Doppler frequency of 200 Hz and a fixed RMS delay spread of 400 ns.

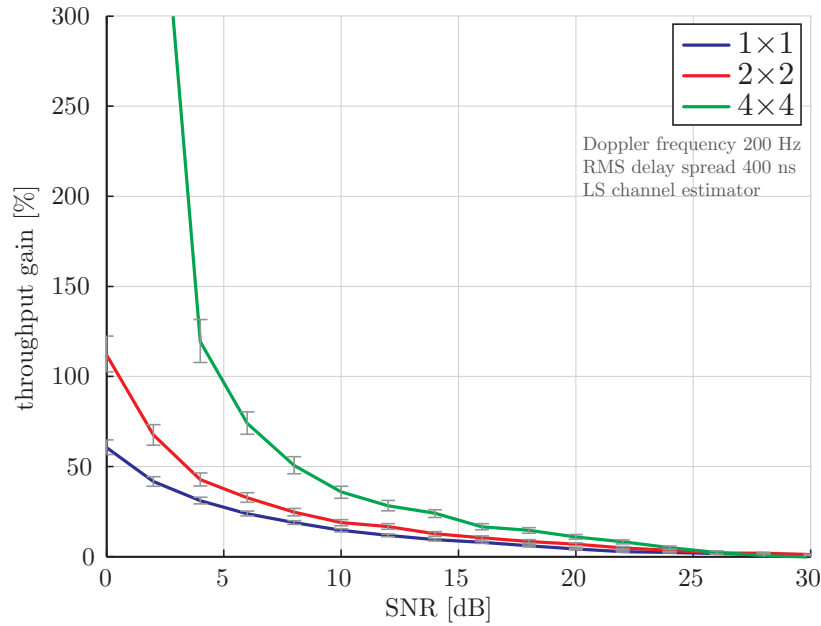
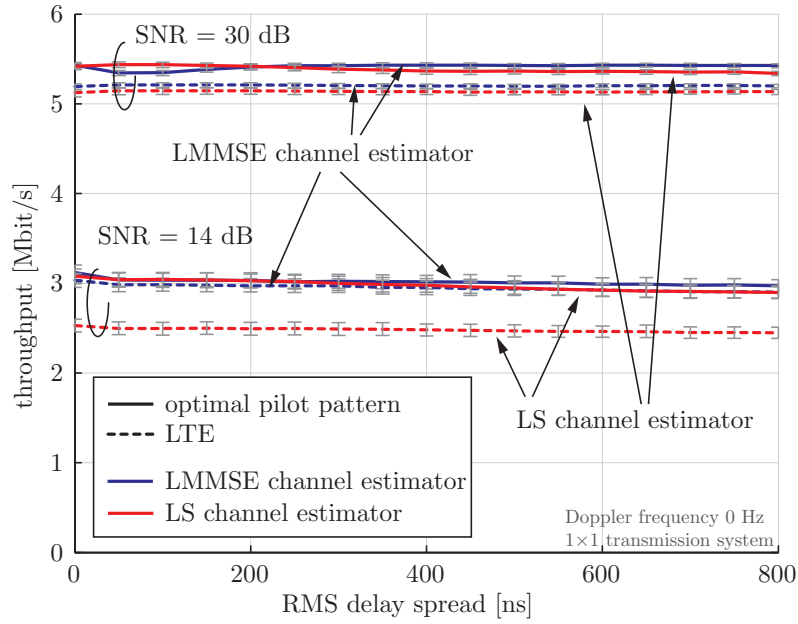


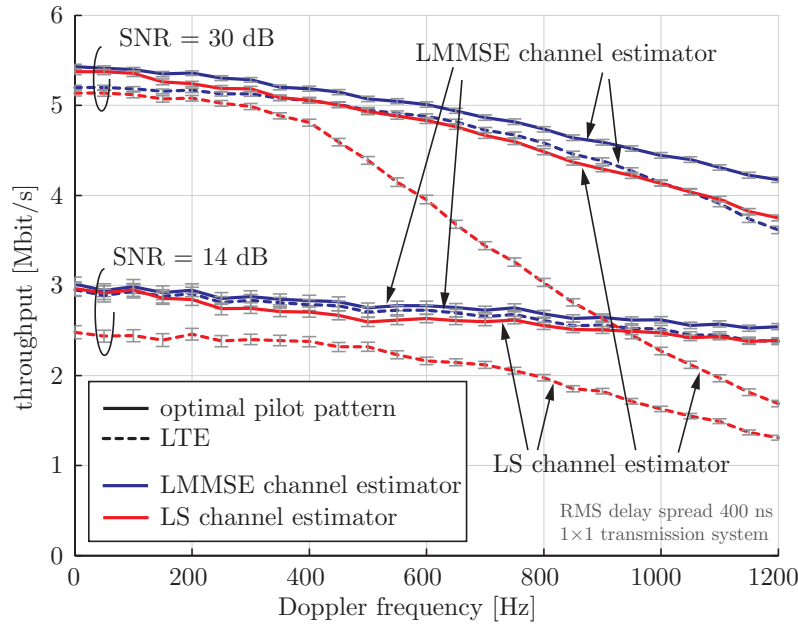
Figure 5.17: Throughput gain of a system utilizing an optimal pilot pattern with optimal power distribution compared to a system with optimal pilot pattern with unit power allocation, as a function of SNR for a fixed Doppler frequency of 200 Hz and a fixed RMS delay spread of 400 ns.

terns for an LMMSE channel estimator is approximately 2.5% at an SNR of 14 dB and 4.5% at an SNR of 30 dB. The gain when utilizing optimal pilot patterns for an LMMSE channel estimator is significantly lower than for an LS channel estimator, especially for an SNR of 14 dB. It is remarkable that the throughput of optimal pilot patterns for LS and LMMSE channel estimators is almost identical with a small performance gain when applying optimal LMMSE channel estimator. Therefore, when utilizing the proposed optimal pilot patterns under time-invariant channels, the performance of an optimal LMMSE estimator can almost be achieved by an LS channel estimator of lower complexity.

Figure 5.18(b) displays the throughput as a function of Doppler frequency for LMMSE and LS channel estimators at a fixed RMS delay spread of 400 ns and an SNR of 14 dB and 30 dB. The throughput improvement with the proposed pilot patterns compared to an LTE system with an LMMSE channel estimator is lower than when utilizing an LS channel estimator. For an LMMSE channel estimator the gain ranges between 2% and 7% at an SNR of 14 dB and between 3% and 15% at an SNR of 30 dB. For an LS channel estimator with the proposed pilot patterns, a system throughput is close to the system with a fixed LTE pilot pattern employing an LMMSE channel estimator. Therefore, I can conclude that with the proposed optimal pilot patterns, it is possible to decrease the computational complexity at



(a) Throughput versus RMS delay spread for LMMSE and LS channel estimators at a Doppler frequency of 0 Hz. For time-invariant channels, the performance of an optimal LMMSE estimator can almost be achieved by an LS channel estimator of lower complexity.



(b) Throughput versus Doppler frequency for LMMSE and LS channel estimators at an RMS delay spread of 400 ns.

Figure 5.18: Throughput comparison of LS and LMMSE channel estimators employing LTE compliant and optimal pilot patterns at SNR of 14 dB and 30 dB.

the receiver side while almost achieving the performance of an LMMSE channel estimator with fixed pilot patterns.

5.2 Adaptive Pilot-Symbol Patterns

Current standards for wireless communications typically utilize fixed pilot-symbol patterns for the purpose of channel estimation. Such an approach provides a high level of system robustness, if the pilot-symbol patterns are designed properly. At the same time, however, resources such as power and bandwidth are devoted solely for channel estimation and therefore limit the throughput of the system.

In this section, I describe a concept of adaptive pilot-symbol patterns that adjust to varying channel conditions. Furthermore, I investigate the feedback requirements for adaptive pilot-symbol patterns applied in MIMO OFDM systems. The main goal is to support a wide range of Doppler spreads and RMS delay spreads while keeping the number of allowed pilot-symbol patterns at a minimum.

In Section 5.1, I demonstrated how to design an optimal pilot-symbol pattern for a given SNR value and a given channel autocorrelation matrix. The channel autocorrelation matrix can be decomposed into a time correlation matrix and a frequency correlation matrix [20]. These two correlation matrices depend on the RMS delay spread and maximum Doppler spread, respectively. Therefore, an optimal pilot-symbol pattern is given by a triple of SNR, Doppler frequency, and RMS delay spread values.

Let me consider an LTE system for a moment. This system for wireless transmission allows to adapt coding rate, modulation alphabet, precoding, and some other important parameters of the transmission according to the quality of the channel. The main idea in LTE is the usage of the so-called CQI that is reported by the user equipment back to an eNodeB. The CQI is not only a measure of the channel quality, in consequence it also defines two important transmission properties, the coding rate and the modulation alphabet. There are 15 different CQIs defined in LTE. The CQI corresponds to an AWGN equivalent SNR value of a channel realization. Therefore, for each CQI value, an optimal pilot pattern should be defined. In this way, no additional feedback overhead is created to distinguish different SNR values, since the feedback for CQI is already implemented in the standard feedback channel.

In order to allow the pilot pattern to adapt to a varying user mobility, pilot patterns for various Doppler spreads (user velocities) have to be defined. Later in this section, I investigate a number of different pilot-symbol patterns required to support a wide range of Doppler spreads. A typical LTE system shall support users moving

Table 5.3: Simulator settings for adaptive pilot patterns.

Parameter	Value
Bandwidth	1.4 MHz
Number of data subcarriers	72
FFT size	128
CP duration	$\approx 4.76 \mu\text{s}$
Number of transmit antennas	1
Number of receive antennas	1
Receiver type	ZF
Transmission mode	SISO

with velocities up to 500 km/h, which corresponds to a Doppler frequency of approximately 1150 Hz at a carrier frequency of 2.5 GHz. Therefore, I divide the range of the Doppler frequencies between 0 and 1200 Hz into F bins and for each bin, an optimal pilot-symbol pattern is defined for the center value of the corresponding bin.

Finally, in order to allow the pilot-symbol patterns to adapt to frequency selectivity of the channel, optimal pilot-symbol patterns have to be designed for different values of RMS delay spread. Typical values of RMS delay spread range between 0 and 800 ns. I divide this range of RMS delay spread into T bins and for each bin, an optimal pilot-symbol pattern is defined for the center value of the corresponding bin.

Since the same pilot-symbol pattern is used for the entire transmission bandwidth, the extra feedback requirements caused by the adaptive pilot-symbol patterns are $\log_2(F) \log_2(T)$ bits, if coded brute force. In case of a multi-user transmission, $\log_2(F) \log_2(T)$ bits need to be reserved for each user. Note that since a single pilot-symbol pattern is used across the entire transmission bandwidth, its feedback requirements are negligible compared to other narrowband feedback indicators such as CQI, PMI, and RI.

Simulation Results

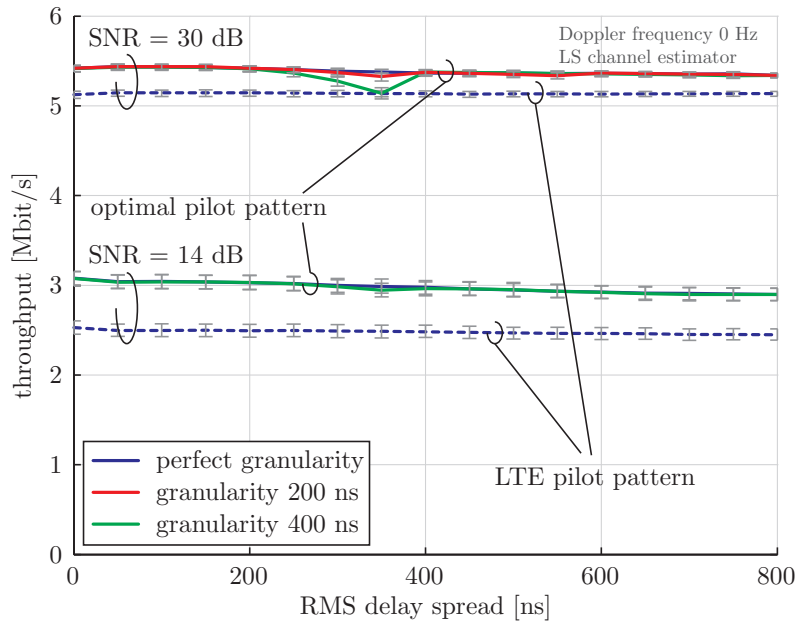
In the following, I present simulation results and compare the throughput of a system with adaptive pilot-symbol patterns with different bin granularities, against a system with a pilot-symbol pattern defined by LTE standards and unit distribution of power between data- and pilot-symbols. Table 5.3 shows the most important simulator settings of the Vienna LTE simulator [13].

Figure 5.19(a) illustrates throughput as a function of RMS delay spread for a fixed Doppler frequency of 0 Hz at SNR values of 14 dB and 30 dB. The blue dashed curves represent the throughput for an SISO LTE transmission system at a given SNR value. The throughput is approximately constant versus RMS delay spread for the LTE system. The blue solid curve represents a system with optimal pilot

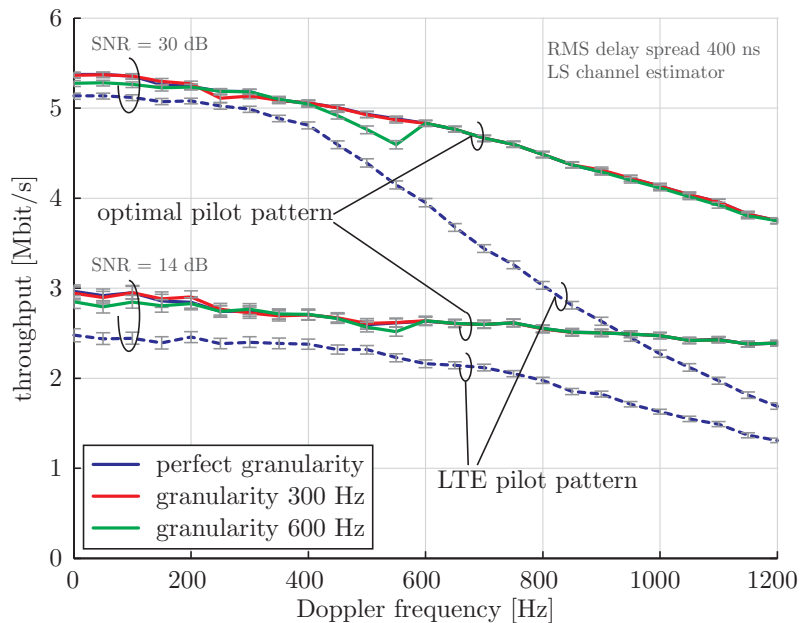
patters with perfect granularity, i.e., an optimal pilot pattern is generated for each RMS delay value. This system outperforms the standard compliant LTE system in the whole considered RMS delay range. Let me focus on the green solid curve in the 14 dB SNR scenario. This curve represents a system utilizing optimal pilot patterns, but in contrast to the previous case, the RMS delay spread range is divided into two bins, and optimal pilot-symbol patterns generated for the center points are utilized in the corresponding bins. The system with only two different pilot patterns in the considered RMS delay spread range shows the same performance as the competitive system utilizing a much higher number of pilot-symbol patterns. Therefore, I can conclude that for the considered situation of a fixed SNR of 14 dB and a fixed Doppler frequency of 0 Hz, only one bit of extra feedback is required, i.e., $T = 2$. Considering the green curve at an SNR value of 30 dB, a throughput drop occurs compared to the perfect case at an RMS delay spread of 350 ns. Therefore, I divide the RMS delay spread operation range into four bins, represented by the red curve. In this case the performance is the same as in the case of perfect granularity. Therefore, I can conclude that with two bits of extra wide-band feedback the RMS delay spread operation range up to 800 ns can be served.

Figure 5.19(b) shows throughput versus Doppler frequency for a fixed RMS delay spread of 400 ns at SNR of 14 dB and 30 dB. The blue dashed curves represents throughput for an SISO LTE transmission system at a given SNR value. A throughput drop occurs as the Doppler frequency increases. The blue solid curve represents a system with optimal pilot patters with perfect granularity. This system outperforms the standard compliant LTE system in the whole considered Doppler frequency range. Let me focus on the green solid curve it the 14 dB SNR scenario. This curve represents a system utilizing optimal pilot patterns, but in contrast to the previous case, the Doppler frequency range is divided into two bins, and optimal pilot-symbol patterns generated for the center points are utilized in the corresponding bins. The system utilizing only two different patterns in the considered Doppler frequency range shows poorer performance than the system with perfect granularity. The performance loss can be observed at two points: first, at low values of Doppler frequency, where too many pilots are utilized for channel estimation and therefore they cannot serve for data transmission. A second point is, at a Doppler frequency of 550 Hz, where the channel is not estimated properly. Therefore, I divide the Doppler frequency range into four bins. The system utilizing four different pilot patterns is represented by the red curve. The performance of such a system is the same as of the system with perfect granularity. Therefore, I can conclude that in order to support Doppler frequencies up to 1200 Hz at an SNR value of 14 dB, four different pilot patterns are required. In order to draw more general conclusions, let me consider the simulation results at a higher SNR value of 30 dB. In general, at higher SNR values the system is more sensitive to the utilized pilot patterns, since

5. OPTIMAL PILOT-SYMBOL PATTERN DESIGN



(a) Throughput as a function of RMS delay spread for a fixed SNR of 14 dB and 30 dB, and a fixed Doppler frequency of 0 Hz. Two bits of extra wide-band feedback are sufficient to support a range of RMS delay spread up to 800 ns.



(b) Throughput as a function of Doppler frequency for a fixed SNR of 14 dB and 30 dB, and a fixed RMS delay spread of 400 ns. Two bits of extra wide-band feedback are sufficient to support a range of Doppler frequency up to 1200 Hz.

Figure 5.19: Throughput comparison of an LS with optimal pilot patterns with various feedback granularities at SNR of 14 dB and 30 dB.

more precise channel estimates are required. The curves at an SNR of 30 dB show the same behavior as the 14 dB. Thus, four different pilot patterns are sufficient to support the desired Doppler frequency range.

5.3 Summary

In this chapter, I dealt with optimal pilot-symbol design for doubly-selective channels for MIMO OFDM systems. Compared to the previous chapter, I utilized an upper bound of constrained capacity as the cost function compared the post-equalization SINR that does not allow to introduce a penalty due to the bandwidth occupation by pilot-symbols. I compared the performance of a system utilizing optimal pilot patterns with an LTE system utilizing fixed pilot patterns. Significant throughput gains can be achieved when utilizing optimal pilot patterns. Last but not least, I introduced the concept of adaptive pilot patterns that adjust to the varying channel statistics and investigate the feedback requirements for such adaptive pilot patterns. It turned out that only four bits of extra wide-band feedback are required in order to support a wide range of situations.

As the cost function for the optimal pilot patterns, I chose an upper bound of the constrained capacity. This is a good compromise that does not requires perfect channel knowledge at the transmitter and the solution can be obtained off-line. However a more suitable cost-function might exist.

The feedback requirements of adaptive pilot patterns are supported only by simulation results. Therefore, a further investigation is required. As result, I obtained that four bits of extra feedback per user are required. This number could be even further decreased when applying differential encoding of the feedback or some other methods.

The content of this chapter is partially based on the following publications that I authored. The first insights into this topic were published in [86]. In order to find optimal pilot distance in a frequency selective system, the authors of [86] considered low and high SNR approximations of the constrained channel capacity. The analysis was extended towards time-variant channels in [87]. The authors of [95] conducted an analysis of the feedback requirements of adaptive pilot patterns.

6 Summary

Based on the results presented in this thesis, I can conclude that the current LTE standard for wireless communications, from a physical layer point of view, is still not optimal and there is a lot of room for improvement.

6.1 Contributions

In Chapter 3, I derived analytical models for the performance of an MIMO OFDM receiver. Firstly, I derived an expression for the MSE of an LS channel estimator utilizing a two-dimensional interpolation. It turned out that the MSE expression consists of two parts, a noise dependent part and a noise independent part, also called interpolation error. The interpolation error can cause a performance saturation as it becomes the dominant term in the MSE expression. I, further, derived the MSE expression for an LMMSE channel estimator. It can be shown that an LMMSE channel estimator can be obtained via interpolation of an LS channel estimator at the pilot positions, therefore the results shown for an LS channel estimator utilizing a two-dimension interpolation are valid also for an LMMSE channel estimator. However, the interpolation weights are in general SNR dependent, thus the interpolation error and the noise dependent coefficient depend on SNR as well. Secondly, I provided a model for ICI modeling that allows to design advanced receiver structures taking ICI into account. In the derived model, I applied a BEM approach with orthogonalized polynomials and DPS sequences. Such an approach significantly improves the ICI estimation error compared to the previously proposed approaches. Thirdly, I derived an expression for the post-equalization SINR for a ZF equalizer including imperfect channel knowledge. This allows to analytically treat the performance of an MIMO OFDM transmission system.

Chapter 4 provides a framework for an optimal power distribution among pilot- and data-symbols in an MIMO OFDM transmission system. As the cost function, I chose the average post-equalization SINR for a ZF equalizer under imperfect channel knowledge. The optimum power distribution depends on the ratio of the pilot- and data-symbols, and on the performance of the channel estimator. The throughput gains achieved by this strategy range up to 10% compared to the case of unit power distribution. Later in this chapter, I introduced a power efficient power distribution. I revisited a commonly mistaken intuition that when a more precise channel estimate is desired, a power increase at the pilot-symbols will do the job. However, in situations with a large interpolation error, such a strategy does not improve the MSE and on the other hand, a further power boost at the data-symbols increases inter-layer interference. Therefore, in situations with a large interpolation error, a power decrease can be of benefit instead. Thus, instead of maximizing the post-equalization SINR, I rather minimize the actual transmit power and set a constraint on the post-equalization SINR. By this approach a significant amount of transmit power can be saved while not influencing the performance of the overall system.

In Chapter 5, I derived a framework allowing to design optimal pilot patterns. As a cost function, I utilized an upper bound of the constrained channel capacity. In general, an optimal pilot pattern depends on an SNR value, channel correlation matrix, and on a channel estimator performance. Compared to a traditional approach of fixed pilot patterns utilizing in the LTE standard, gains up to 850% can be achieved depending on the operation point. The gain is higher for low SNR values, for low RMS delay spread, and for high Doppler spreads. I also introduced a concept of adaptive pilot patterns that adjust to varying channel statistics. Only with four additional wide-band feedback bits per user, users can effectively benefit from the optimal pilot patterns.

6.2 Outlook

Due to the high cost and complexity of measurements, typically, a new technology is at first investigated by means of simulations. However, before applying in a real world, extensive measurements have to be conducted in order to provide sufficient evidence for a proper operation of the investigated technology. Thus, all concepts provided in this thesis should be a subject of an intensive measurement campaign. Such a measurement campaign can provide evidence that the assumptions made throughout this thesis are reasonable and do not restrict the validity of the presented work.

During my investigation, I neglected antenna correlations. However, antennas are hardly perfectly uncorrelated and therefore antenna correlation should be taken into

account in the next step of the introduced optimization framework. Especially, with the wild race of increasing the number of transmit antennas at the base station, it cannot be expected that all spatial layers have the same power and therefore the optimal power distribution may differ among individual layers at the pilot- and also data-symbols.

I introduced an approach for a power reduction while preserving the performance of the system for situations with a dominant interpolation error that occur at high Doppler frequencies. This is a simple step towards green radio exploited at the physical layer. More effort should be invested into this direction of research.

In this thesis, I considered single-user MIMO setups. In the future, a shift towards multi-user MIMO is expected and therefore a way of adaptive pilot patterns incorporation into multi-user MIMO has to be investigated in order for a successful connection of these two concepts.

For today's typical applications, ICI does not play a crucial role yet. However, with high mobile velocities this is going to change and therefore more advanced ICI-aware receivers have to be investigated. The approaches considered until now set unrealistic assumptions.

The derived channel estimation MSE as a function of the interpolation weights provides a useful framework for design on various interpolators. In this way interpolators fulfilling various criteria can be designed to deliver optimal performance in the desired situations.

A Interpolation Error Lower Bound

In the following appendix, I show that the interpolation error is lower bounded by

$$0 \leq d. \quad (\text{A.1})$$

As shown in Chapter 3 by Equation (3.11), the interpolation error is given as

$$d = \frac{1}{N_d} \sum_{j=1}^{N_d} \left(1 - 2 \sum_{i \in \mathcal{P}_j} w_{j,i} \Re \{R_{j,i}\} + \sum_{i \in \mathcal{P}_j} \sum_{i' \in \mathcal{P}_j} w_{j,i} w_{j,i'} R_{i,i'} \right). \quad (\text{A.2})$$

The interpolation error in the above equation is obtained as arithmetical mean of interpolation errors at individual data positions j that are given as

$$d_j = 1 - 2 \sum_{i \in \mathcal{P}_j} w_{j,i} \Re \{R_{j,i}\} + \sum_{i \in \mathcal{P}_j} \sum_{i' \in \mathcal{P}_j} w_{j,i} w_{j,i'} R_{i,i'}. \quad (\text{A.3})$$

First, I show that $0 \leq d_j$ is valid for all j , from which follows that $0 \leq d$ is valid.

Let me define a variable $\bar{h}_{d,j}$, similar to Equation (3.3), as weighted average of the channel at the pilot positions from set \mathcal{P}_j

$$\bar{h}_{d,j} = \sum_{i \in \mathcal{P}_j} w_{j,i} h_{p,i}. \quad (\text{A.4})$$

Compared to the previous case of Equation (3.3), I obtain the channel estimate at a data position j as a weighted average of the channel estimate at the neighboring pilot positions. The considered neighbors are defined in the set \mathcal{P}_j . The case of Equation (A.4) corresponds to perfect channel knowledge at the pilot-symbol positions.

In the next step, I define the MSE error between $h_{d,j}$ and $\bar{h}_{d,j}$ as

$$\bar{\sigma}_{e,j}^2 = \mathbb{E} \left\{ \|h_{d,j} - \bar{h}_{d,j}\|^2 \right\} \quad (\text{A.5})$$

$$= \mathbb{E} \left\{ \|h_{d,j}\|^2 \right\} - 2\Re \left\{ \mathbb{E} \left\{ h_{d,j}^* \bar{h}_{d,j} \right\} \right\} + \mathbb{E} \left\{ \|\bar{h}_{d,j}\|^2 \right\}. \quad (\text{A.6})$$

The error caused by interpolation in Equation (A.5) is defined as a quadratic form and there $0 \leq \bar{\sigma}_{e,j}^2$ holds. Equation (A.6) can be expanded by following the same line of arguments as in Section 3.1 and results in

$$\bar{\sigma}_{e,j}^2 = 1 - 2 \sum_{i \in \mathcal{P}_j} w_{j,i} \Re \{ R_{j,i} \} + \sum_{i \in \mathcal{P}_j} \sum_{i' \in \mathcal{P}_j} w_{j,i} w_{j,i'} R_{i,i'}. \quad (\text{A.7})$$

The expressions in Equation (A.7) and Equation (A.3) are identical and therefore I can conclude that the interpolation error is always equal or larger than zero.

B Two-Dimensional Linear Interpolation

In the following appendix, it is shown how to obtain interpolation weights $w_{j,i}$ in Equation (3.3) when following two dimensional linear interpolation.

First of all, I define a vector \mathbf{p}_i , whose entries are positions of the i -th pilot in the time-frequency grid, namely $\mathbf{p}_i = [f_i, t_i]^T, i = 1, 2, \dots, N_p$, where the scalar f_i is a frequency index and t_i a time index. Similarly, I denote the position of the j -th data-symbol in the time-frequency grid by a vector \mathbf{d}_j .

Example: I assume that the channel of the first data symbol $h_{d,1}$ is located within the plane spanned by the channel estimates at the first three pilot symbols, $h_{p,1}, h_{p,2}, h_{p,3}$. The plane spanned by these three channel estimates is defined as follows

$$\mathbf{d}_1 = \mathbf{p}_1 + a(\mathbf{p}_2 - \mathbf{p}_1) + b(\mathbf{p}_3 - \mathbf{p}_1), \quad (\text{B.1})$$

where a and b are real scalars that indicate how far is the vector \mathbf{d}_1 located from \mathbf{p}_1 in respective directions. For a general solution, Equation (B.1) can be reformulated as

$$\mathbf{d}_1 = (1 - a - b)\mathbf{p}_1 + a\mathbf{p}_2 + b\mathbf{p}_3. \quad (\text{B.2})$$

Comparing Equation (3.3) with Equation (B.2), using a linear interpolation, it can be recognized that the interpolation weights are given as $w_{1,1} = 1 - a - b$, $w_{1,2} = a$ and $w_{1,3} = b$. Note that the sum of the interpolation weights is equal to one.

If the interpolated data-symbol is located between the three nearest pilot-symbols, as it is the case in Figure 3.2, the interpolation weights $w_{j,i}$ are bounded as $0 \leq w_{j,i} \leq 1$. In case of extrapolation, when the data-symbol is located outside of a triangle area spanned by three closest pilot-symbols, the interpolation weights can

B. TWO-DIMENSIONAL LINEAR INTERPOLATION

become negative and also larger than one.

C MSE Parameter Approximation for LMMSE

In order to quantify MSE performance of a linear channel estimator, variables c_e and d were derived in Chapter 3. In the special case of an LS channel estimator with a two-dimensional linear interpolator, these variables turned out to be SNR independent, since the interpolation weights in Equation (3.3) are chosen solely based on the "geometrical" distances between pilot- and data-symbols. In general, variables c_e and d depend on SNR. This appendix provides a simple approximation method for finding SNR independent variables c_e and d for an LMMSE channel estimator.

Considering Figure 3.5, it may be believed that the variables variables c_e and d are SNR independent. However, this is not the case and therefore the MSE of an LMMSE channel estimator can only be approximated by

$$\sigma_e^2 \approx c_e \frac{\sigma_n^2 + \sigma_{\text{ICI}}^2}{\sigma_p^2} + d, \quad (\text{C.1})$$

where the scalar coefficient c_e and the interpolation error d can be obtained by the following method. First, it is assumed that there is no noise and no ICI, and insert $\sigma_n^2 = 0$ and $\sigma_{\text{ICI}}^2 = 0$ into Equation (3.16), providing an MSE value given with perfect channel knowledge at the pilot-symbols, resulting in the interpolation error d . Figure 3.3 shows the value of the interpolation error d over Doppler frequency for 1×1 and 4×4 systems for LTE pilot-symbol pattern obtained by this method. In the case of a 2×2 MIMO system using the pilot-symbol pattern defined in LTE, the interpolation error d is the same as in a 1×1 case, since the amount of the pilot-symbols is the same and an LMMSE estimator performs identically.

C. MSE PARAMETER APPROXIMATION FOR LMMSE

The SNR independent value of c_e can be obtained by applying linear regression on Equation (3.9).

D ZF Post-equalization SINR

In the following appendix, I derive the post-equalization SINR for a ZF equalizer with imperfect channel knowledge. Let me begin with the input-output relation under imperfect channel knowledge

$$\mathbf{y}_k = \left(\hat{\mathbf{H}}_{k,k} + \mathbf{E}_{k,k} \right) \mathbf{W}_k \mathbf{s}_k + \mathbf{n}_k + \sum_{m \neq k} \mathbf{H}_{k,m} \mathbf{W}_m \mathbf{s}_m. \quad (\text{D.1})$$

Since the channel estimation error matrix $\mathbf{E}_{k,k}$ is unknown at the receiver, the ZF solution is given again by Equation (3.32), with the channel matrix $\mathbf{H}_{k,k}$ replaced by its estimate $\hat{\mathbf{H}}_{k,k}$ that is known at the receiver

$$\hat{\mathbf{s}}_k = \left(\hat{\mathbf{G}}_{k,k}^H \hat{\mathbf{G}}_{k,k} \right)^{-1} \hat{\mathbf{G}}_{k,k}^H \mathbf{y}_k, \quad (\text{D.2})$$

with matrix $\hat{\mathbf{G}}_{k,k}$ being equal to $\hat{\mathbf{H}}_{k,k} \mathbf{W}_k$. The symbol error after the ZF equalizer is given as

$$\hat{\mathbf{s}}_k - \mathbf{s}_k = \left(\hat{\mathbf{G}}_{k,k}^H \hat{\mathbf{G}}_{k,k} \right)^{-1} \hat{\mathbf{G}}_{k,k}^H \left(\mathbf{E}_{k,k} \mathbf{W}_k \mathbf{s}_k + \mathbf{n}_k + \sum_{m \neq k} \mathbf{H}_{k,m} \mathbf{W}_m \mathbf{s}_m \right). \quad (\text{D.3})$$

From Equation (D.3), the instantaneous symbol error matrix can be computed

$$\begin{aligned}
\text{SE}_k &= (\hat{\mathbf{s}}_k - \mathbf{s}_k) (\hat{\mathbf{s}}_k - \mathbf{s}_k)^{\text{H}} \\
&= \left(\hat{\mathbf{G}}_{k,k}^{\text{H}} \hat{\mathbf{G}}_{k,k} \right)^{-1} \hat{\mathbf{G}}_{k,k}^{\text{H}} \left(\mathbf{E}_{k,k} \mathbf{W}_k \mathbf{s}_k + \mathbf{n}_k + \sum_{m \neq k} \mathbf{H}_{k,m} \mathbf{W}_m \mathbf{s}_m \right) \\
&\quad \left(\mathbf{E}_{k,k} \mathbf{W}_k \mathbf{s}_k + \mathbf{n}_k + \sum_{m \neq k} \mathbf{H}_{k,m} \mathbf{W}_m \mathbf{s}_m \right)^{\text{H}} \hat{\mathbf{G}}_{k,k} \left(\hat{\mathbf{G}}_{k,k} \hat{\mathbf{G}}_{k,k}^{\text{H}} \right)^{-1}.
\end{aligned} \tag{D.4}$$

The instantaneous post-equalization SINR at the layer l and subcarrier k is given as

$$\gamma_{l,k} = \frac{\mathbf{e}_l^{\text{H}} \mathbf{s}_k \mathbf{s}_k^{\text{H}} \mathbf{e}_l}{\mathbf{e}_l^{\text{H}} \text{SE}_k \mathbf{e}_l}, \tag{D.5}$$

where the vector \mathbf{e}_l is an $N_l \times 1$ zero vector with a one on the l -th element. This vector extracts the signal on the corresponding layer after the equalizer. For the further derivation, I assume:

- Channel estimation error and noise are uncorrelated.
- Noise and data are uncorrelated.
- Channel estimation error and data are uncorrelated.
- Data symbol on different layers are uncorrelated.
- Power is equally distributed between all layers.
- Power is equally distributed between all transmit antennas.

In order to obtain average layer post-equalization SINR, I apply expectation operator for a given estimated channel matrix $\hat{\mathbf{G}}_{k,k}$ on Equation (D.5)

$$\begin{aligned}
\hat{\gamma}_{l,k} &= \mathbb{E} \left\{ \gamma_{l,k} | \hat{\mathbf{G}}_{k,k} \right\} \\
&= \frac{\sigma_s^2}{(\sigma_e^2 \sigma_d^2 + \sigma_n^2 + \sigma_{\text{ICI}}^2) \mathbf{e}_l^{\text{H}} \left(\hat{\mathbf{G}}_{k,k}^{\text{H}} \hat{\mathbf{G}}_{k,k} \right)^{-1} \mathbf{e}_l}.
\end{aligned} \tag{D.6}$$

The nominator of the expression in Equation (D.6) is obtained as:

$$\begin{aligned}
\mathbb{E} \left\{ \mathbf{e}_l^{\text{H}} \mathbf{s}_k \mathbf{s}_k^{\text{H}} \mathbf{e}_l \right\} &= \mathbf{e}_l^{\text{H}} \mathbb{E} \left\{ \mathbf{s}_k \mathbf{s}_k^{\text{H}} \right\} \mathbf{e}_l \\
&= \mathbf{e}_l^{\text{H}} \sigma_s^2 \mathbf{I} \mathbf{e}_l \\
&= \sigma_s^2 \mathbf{e}_l^{\text{H}} \mathbf{I} \mathbf{e}_l \\
&= \sigma_s^2.
\end{aligned} \tag{D.7}$$

The quantities σ_e^2 , σ_n^2 , and σ_{ICI}^2 in Equation (D.11), I define as

$$\begin{aligned} \mathbb{E} \{ \mathbf{E}_{k,k} \mathbf{W}_k \mathbf{s}_k \mathbf{s}_k^H \mathbf{W}_k^H \mathbf{E}^H \} &= \mathbb{E} \{ \mathbf{E}_{k,k} \mathbf{x}_k \mathbf{x}_k^H \mathbf{E}^H \} & (\text{D.8}) \\ &= \frac{\sigma_d^2}{N_t} \mathbb{E} \{ \mathbf{E}_{k,k} \mathbf{E}^H \} \\ &= \sigma_e^2 \sigma_d^2 \mathbf{I} \end{aligned}$$

$$\mathbb{E} \{ \mathbf{n}_k \mathbf{n}_k^H \} = \sigma_n^2 \mathbf{I} \quad (\text{D.9})$$

$$\mathbb{E} \left\{ \sum_{m \neq k} \mathbf{H}_{k,m} \mathbf{W}_m \mathbf{s}_m \left(\sum_{m \neq k} \mathbf{H}_{k,m} \mathbf{W}_m \mathbf{s}_m \right)^H \right\} = \sigma_{\text{ICI}}^2 \mathbf{I}. \quad (\text{D.10})$$

In order to consider the true post-equalization SINR, I define $\hat{\mathbf{H}}_{k,k} = \mathbf{H}_{k,k} + \mathbf{E}_{k,k}$. Due to the equivalency of to the previous model $\mathbf{H}_{k,k} = \hat{\mathbf{H}}_{k,k} + \mathbf{E}_{k,k}$, I directly obtain the average post-equalization SINR of a ZF equalizer at the l -th transmission layer for a given effective channel matrix $\mathbf{G}_{k,k}$ as

$$\tilde{\gamma}_{l,k} = \frac{\sigma_s^2}{(\sigma_e^2 \sigma_d^2 + \sigma_n^2 + \sigma_{\text{ICI}}^2) \mathbf{e}_l^H \left(\mathbf{G}_{k,k}^H \mathbf{G}_{k,k} \right)^{-1} \mathbf{e}_l}. \quad (\text{D.11})$$

The main difference between Equation (D.11) and Equation (D.6) lies in the replacement of $\hat{\mathbf{G}}_{k,k}$ by $\mathbf{G}_{k,k}$. The difference between these two expression is visible especially in a low SNR region (see Figure 3.8).

E Constrained Capacity Upper Bound

In the following, I derive an upper bound for the constrained capacity including channel estimation error. Let me begin the derivation with the instantaneous constrained capacity

$$\mathcal{C} = B_s \sum_{l=1}^{N_1} \sum_k \log_2(1 + \gamma_{l,k}), \quad (\text{E.1})$$

where B_s represents the bandwidth of a subcarrier. The second sum in the above equation is a sum over all subcarriers carrying data-symbols. In the next step, I include Equation (D.5) into Equation (E.1)

$$\mathcal{C} = B_s \sum_{l=1}^{N_1} \sum_k \log_2 \left(1 + \frac{\mathbf{e}_l^H \mathbf{s}_k \mathbf{s}_k^H \mathbf{e}_l}{\mathbf{e}_l^H \mathbf{S} \mathbf{E}_k \mathbf{e}_l} \right). \quad (\text{E.2})$$

In order to obtain a feasible solution for the considered optimization problems, I consider a mean value of the constrained capacity

$$\mathbb{E} \{ \mathcal{C} \} = B_s \sum_{l=1}^{N_1} \sum_k \mathbb{E} \left\{ \log_2 \left(1 + \frac{\mathbf{e}_l^H \mathbf{s}_k \mathbf{s}_k^H \mathbf{e}_l}{\mathbf{e}_l^H \mathbf{S} \mathbf{E}_k \mathbf{e}_l} \right) \right\}. \quad (\text{E.3})$$

However, the expectation operator in Equation (E.4) cannot be directly evaluated, therefore, only an upper bound of the mean constrained channel capacity is considered by applying Jensen's inequality [91, 92] as follows

$$\mathbb{E} \{ \mathcal{C} \} \leq \bar{\mathcal{C}}, \quad (\text{E.4})$$

with

$$\begin{aligned}\bar{C} &= B_s \sum_{l=1}^{N_1} \sum_k \log_2 \left(1 + \mathbb{E} \left\{ \frac{\mathbf{e}_l^H \mathbf{s}_k \mathbf{s}_k^H \mathbf{e}_l}{\mathbf{e}_l^H \mathbf{S} \mathbf{E}_k \mathbf{e}_l} \right\} \right) \\ &= B(D_f, D_t) \log_2(1 + \bar{\gamma}),\end{aligned}\tag{E.5}$$

with the transmission bandwidth being sum of subchannels over all data-subcarriers and layers

$$B(D_f, D_t) = B_s \sum_{l=1}^{N_1} \sum_k 1.\tag{E.6}$$

F AWGN-equivalent SNR Definition

In this appendix, AWGN-equivalent SNR definition is provided. AWGN-equivalent SNR represents a measure for the quality of a transmission channel. Such a measure is frequently used in system modeling for link abstraction [31]. Thanks to the usage of AWGN-equivalent SNR in frequency-selective OFDM transmissions it is possible to obtain a single-valued quality measure representing "average" channel quality of all considered subcarriers. Between the most common averaging strategies belong Mutual Information Effective SINR Mapping (MIESM) and Exponential Effective SINR Mapping (EESM).

In MIESM and EESM, AWGN-equivalent SNR γ_{AWGN} is obtain via the following expression

$$\gamma_{\text{AWGN}} = \beta f^{-1} \left(\frac{1}{N_d} \sum_{d=1}^{N_d} f \left(\frac{\gamma_d}{\beta} \right) \right), \quad (\text{F.1})$$

where $f(\cdot)$ represents Bit-Interleaved Coded Modulation (BICM) capacity in case of MIESM and an exponential function in case of EESM, respectively [96]. Variable γ_d is the actual SINR at the subcarrier d . Coefficient β serves as a calibration parameter in order to match the mapping to various coding rates and modulation alphabets.

Acronyms

3GPP	3rd Generation Partnership Project
AMC	Adaptive Modulation and Coding
AMPS	Analogue Mobile Phone System
AWGN	Additive White Gaussian Noise
BEM	Basis Expansion Model
BER	Bit Error Ratio
BICM	Bit-Interleaved Coded Modulation
BLER	Block Error Ratio
BPSK	Binary Phase-Shift Keying
CDD	Cyclic Delay Diversity
CLSM	Closed Loop Spatial Multiplexing
CQI	Channel Quality Indicator
CP	Cyclic Prefix
CRC	Cyclic Redundancy Check
CSI	Channel State Information
DAB	Digital Audio Broadcasting
DFT	Discrete Fourier Transform
DPS	Discrete Prolate Spheroidal
DVB	Digital Video Broadcasting
EESM	Exponential Effective SINR Mapping

FFT	Fast Fourier Transform
GSM	Global System for Mobile communications
ICI	Intercarrier Interference
IFFT	Inverse Fast Fourier Transform
ISI	Inter-Symbol Interference
LMMSE	Linear Minimum Mean Squared Error
LS	Least Squares
LTE	Long Term Evolution
LTE-A	LTE-Advanced
MCS	Modulation and Coding Scheme
MIESM	Mutual Information Effective SINR Mapping
MIMO	Multiple-Input Multiple-Output
ML	Maximum Likelihood
MMSE	Minimum Mean Squared Error
MRC	Maximum Ratio Combining
MSE	Mean Squared Error
NMT	Nordic Mobile Telephone
OFDM	Orthogonal Frequency-Division Multiplexing
OLSM	Open Loop Spatial Multiplexing
QAM	Quadrature Amplitude Modulation
PAPR	Peak-to-Average Power Ratio
PHY	Physical
PMI	Precoding Matrix Indicator
PRC	Partial Response Coding
PSK	Phase-Shift Keying
RB	Resource Block
RI	Rank Indicator
RMS	Root Mean Square
SER	Symbol Error Ratio
SFBC	Space-Frequency Block Code
SINR	Signal to Interference and Noise Ratio

SISO	Single-Input Single-Output
SNR	Signal to Noise Ratio
TACS	Total Access Communication System
TxD	Transmit Diversity
UE	User Equipment
UMTS	Universal Mobile Telecommunications System
WCDMA	Wideband Code-Division Multiple Access
WLAN	Wireless Local Area Network
ZF	Zero Forcing

Bibliography

- [1] N. Tesla, “**On Light and Other High Frequency Phenomena,**” in *National Electric Light Association*, St. Louis, USA, Mar. 1893.
- [2] Ericsson, “**Ericsson Mobility Report: On the Pulse of the Networked Society,**” Feb. 2013.
- [3] S. Sesia, I. Toufik, and M. Baker, **LTE, The UMTS Long Term Evolution: From Theory to Practice.** John Wiley & Sons, Aug. 2009.
- [4] R. Chang, “**Orthogonal Frequency Multiplex Data Transmission System,**” Jan. 1970, US Patent 3,488,445.
- [5] S. Weinstein and P. Ebert, “**Data Transmission by Frequency-Division Multiplexing Using the Discrete Fourier Transform,**” *IEEE Transactions on Communication Technology*, vol. 19, no. 5, pp. 628–634, Oct. 1971.
- [6] A. Peled and A. Ruiz, “**Frequency Domain Data Transmission Using Reduced Computational Complexity Algorithms,**” in *Proc. of IEEE International Conference on Acoustics, Speech, and Signal Processing (ICASSP 1980)*, pp. 964–967, Denver, USA, Apr. 1980, doi: 10.1109/ICASSP.1980.1171076.
- [7] Technical Specification Group Radio Access Network, “**E-UTRA; physical channels and modulation,**” 3GPP, Tech. Rep. TS 36.211 Version 8.7.0, May 2009.
- [8] Technical Specification Group Radio Access Network, “**E-UTRA; multiplexing and channel coding,**” 3GPP, Tech. Rep. TS 36.212, March 2009.
- [9] Technical Specification Group Radio Access Network, “**E-UTRA; physical layer procedures,**” 3GPP, Tech. Rep. TS 36.213, March 2009.
- [10] E. Dahlman, S. Parkvall, and J. Sköld, **4G: LTE/LTE-Advanced for Mobile Broadband.** Academic Press, May 2011.
- [11] M. Rupp, S. Caban, C. Mehlführer, and M. Wrulich, **Evaluation of HSDPA and LTE: From Testbed Measurements to System Level Performance.** Wiley, Nov. 2012.
- [12] C. Mehlführer, M. Wrulich, J. C. Ikuno, D. Bosanska, and M. Rupp, “**Simulating the Long Term Evolution Physical Layer,**” in *Proc. of European Signal Processing Conference (EU-SIPCO 2009)*, Glasgow, Scotland, Aug. 2009, doi: 10.1.1.184.6145.
- [13] C. Mehlführer, J. C. Ikuno, M. Šimko, S. Schwarz, M. Wrulich, and M. Rupp, “**The Vienna LTE Simulators - Enabling Reproducibility in Wireless Communications Research,**” *EURASIP Journal on Advances in Signal Processing*, pp. 1–13, July 2011, doi: 10.1186/1687-6180-2011-29.
- [14] M. Barni and F. Perez-Gonzalez, “**Pushing Science into Signal Processing,**” *Signal Processing Magazine*, vol. 22, no. 4, pp. 120–119, July 2005, doi: 10.1109/MSP.2005.1458324.
- [15] P. Vandewalle, J. Kovačević, and M. Vetterli, “**Reproducible Research in Signal Processing,**” *IEEE Signal Processing Magazine*, vol. 26, no. 3, pp. 37–47, May 2009, doi: 10.1109/MSP.2009.932122.

- [16] M. Dohler, R. Heath Jr., A. Lozano, C. B. Papadias, and R. A. Valenzuela, “**Is the PHY Layer Dead?**” *IEEE Communications Magazine*, no. 4, pp. 159–165, Apr. 2011, doi: 10.1109/MCOM.2011.5741160.
- [17] J. C. Ikuno, S. Schwarz, and M. Šimko, “**LTE Rate Matching Performance with Code Block Balancing,**” in *Proc. of 11th European Wireless Conference (EW 2011)*, Vienna, Austria, Apr. 2011.
- [18] Members of ITU, “**Recommendation ITU-R M.1225: Guidelines for evaluation of radio transmission technologies for IMT-2000,**” International Telecommunication Union (ITU), Tech. Rep., 1997.
- [19] L. Hentilä, P. Kyösti, M. Käske, M. Narandzic, and M. Alatossava, “**MATLAB Implementation of the WINNER Phase II Channel Model ver1.1,**” Dec. 2007.
http://www.ist-winner.org/phase_2_model.html
- [20] M. Šimko, C. Mehlführer, M. Wrulich, and M. Rupp, “**Doubly Dispersive Channel Estimation with Scalable Complexity,**” in *Proc. of 14th International ITG Workshop on Smart Antennas (WSA 2010)*, pp. 251–256, Bremen, Germany, Feb. 2010, doi: 10.1109/WSA.2010.5456443.
- [21] M. Šimko, D. Wu, C. Mehlführer, J. Eilert, and D. Liu, “**Implementation Aspects of Channel Estimation for 3GPP LTE Terminals,**” in *Proc. of 11th European Wireless Conference (EW 2011)*, Vienna, Austria, Apr. 2011.
- [22] S. Schwarz, C. Mehlführer, and M. Rupp, “**Calculation of the Spatial Preprocessing and Link Adaption Feedback for 3GPP UMTS/LTE,**” in *Proc. of IEEE Wireless Advanced*, London, UK, June 2010, doi: 10.1109/WIAD.2010.5544947.
- [23] Q. Wang, C. Mehlführer, and M. Rupp, “**Carrier Frequency Synchronization in the Downlink of 3GPP LTE,**” in *Proc. of 21st Annual IEEE International Symposium on Personal, Indoor and Mobile Radio Communications (PIMRC 2010)*, Istanbul, Turkey, Sept. 2010, doi: 10.1109/PIMRC.2010.5671968.
- [24] M. Šimko, C. Mehlführer, T. Zemen, and M. Rupp, “**Inter Carrier Interference Estimation in MIMO OFDM Systems with Arbitrary Pilot Structure,**” in *Proc. of 73rd IEEE Vehicular Technology Conference (VTC2011-Spring)*, Budapest, Hungary, May 2011, doi: 10.1109/VETECS.2011.5956126.
- [25] I. Solutions, “**Iterative Solutions Coded Modulation Library (ISCML).**”
<http://www.iterativesolutions.com/>
- [26] T. Pircher, “**pycrc CRC calculator and C source code generator.**”
<http://www.tty1.net/pycrc/>
- [27] Q. Wang, C. Mehlführer, and M. Rupp, “**SNR Optimized Residual Frequency Offset Compensation for WiMAX with Throughput Evaluation,**” in *Proc. of 17th European Signal Processing Conference (EUSIPCO 2009)*, Glasgow, Scotland, UK, Aug. 2009.
- [28] Q. Wang, S. Caban, C. Mehlführer, and M. Rupp, “**Measurement Based Throughput Evaluation of Residual Frequency Offset Compensation in WiMAX,**” in *Proc. of 51st International Symposium ELMAR*, pp. 233–236, Zadar, Croatia, Sept. 2009.
- [29] L. Boher, R. Legouable, and R. Rabineau, “**Performance Analysis of Iterative Receiver in 3GPP/LTE DL MIMO OFDMA System,**” in *Proc. of IEEE 10th International Symposium on Spread Spectrum Techniques and Applications 2008 (ISSSTA 2008)*, pp. 103–108, Bologna, Italy, Aug. 2008, doi: 10.1109/ISSSTA.2008.26.
- [30] J. C. Ikuno, M. Wrulich, and M. Rupp, “**Performance and Modeling of LTE H-ARQ,**” in *Proc.*

-
- of *International ITG Workshop on Smart Antennas (WSA 2009)*, Berlin, Germany, Feb. 2009.
- [31] J. C. Ikuno, C. Mehlführer, and M. Rupp, “**A Novel Link Error Prediction Model for OFDM Systems with HARQ**,” in *Proc. of IEEE International Conference on Communications (ICC 2011)*, Kyoto, Japan, May 2011, doi: 10.1109/icc.2011.5962464.
- [32] M. Wrulich, S. Eder, I. Viering, and M. Rupp, “**Efficient Link-to-System Level Model for MIMO HSDPA**,” in *Proc. of 4th IEEE Broadband Wireless Access Workshop*, New Orleans, USA, Dec. 2008, doi: 10.1109/GLOCOMW.2008.ECP.83.
- [33] C. Mehlführer, M. Wrulich, and M. Rupp, “**Intra-Cell Interference Aware Equalization for TxAA HSDPA**,” in *Proc. of 3rd IEEE International Symposium on Wireless Pervasive Computing (ISWPC 2008)*, pp. 406–409, Santorini, Greece, May 2008, doi: 10.1109/ISWPC.2008.4556239.
- [34] A. Ibing and V. Jungnickel, “**Joint Transmission and Detection in Hexagonal Grid for 3GPP LTE**,” in *Proc. of International Conference on Information Networking (ICOIN 2008)*, Busan, South Korea, Jan. 2008, doi: 10.1109/ICOIN.2008.4472825.
- [35] V. Cadambe and S. Jafar, “**Interference Alignment and Degrees of Freedom of the K-user Interference Channel**,” *IEEE Transactions on Information Theory*, vol. 54, no. 8, pp. 3425–3441, Apr. 2008, doi: 10.1109/TIT.2008.926344.
- [36] R. Tresch and M. Guillaud, “**Cellular Interference Alignment with Imperfect Channel Knowledge**,” in *Proc. of IEEE International Conference on Communications Workshops (ICC Workshops 2009)*, Dresden, Germany, June 2009, doi: 10.1109/ICCW.2009.5208018.
- [37] F. Kadrija, M. Šimko, and M. Rupp, “**Iterative Channel Estimation in LTE Systems**,” in *Proc. of 17th International ITG Workshop on Smart Antennas 2013 (WSA 2013)*, Stuttgart, Germany, Mar. 2013.
- [38] M. Meidlinger, M. Šimko, Q. Wang, and M. Rupp, “**Channel Estimators for LTE-A Downlink Fast Fading Channels**,” in *Proc. of 17th International ITG Workshop on Smart Antennas 2013 (WSA 2013)*, Stuttgart, Germany, Mar. 2013.
- [39] Q. Wang, M. Šimko, and M. Rupp, “**Modified Symbol Timing Offset Estimation for OFDM over Frequency Selective Channels**,” in *Proc. of 74th IEEE Vehicular Technology Conference (VTC2011-Fall)*, pp. 1–5, San Francisco, USA, Sept. 2011, doi: 10.1109/VETEFCF.2011.6093032.
- [40] Q. Wang, M. Šimko, and M. Rupp, “**Performance Analysis of LTE Downlink under Symbol Timing Offset**,” in *Proc. of 16th International ITG Workshop on Smart Antennas (WSA 2012)*, pp. 41–45, Dresden, Germany, Mar. 2012, doi: 10.1109/WSA.2012.6181235.
- [41] M. Šimko, S. Pendl, S. Schwarz, Q. Wang, J. C. Ikuno, and M. Rupp, “**Optimal Pilot Symbol Power Allocation in LTE**,” in *Proc. of 74th IEEE Vehicular Technology Conference (VTC2011-Fall)*, San Francisco, USA, Sept. 2011, doi: 10.1109/VETEFCF.2011.6092929.
- [42] X. Dong, W.-S. Lu, and A. C. Soong, “**Linear Interpolation in Pilot Symbol Assisted Channel Estimation for OFDM**,” *IEEE Transactions on Wireless Communications*, vol. 6, no. 5, pp. 1910–1920, May 2007, doi: 10.1109/TWC.2007.360392.
- [43] M. Šimko, Q. Wang, and M. Rupp, “**Optimal Pilot Symbol Power Allocation under Time-variant Channels**,” *EURASIP Journal on Wireless Communications and Networking*, July 2012, doi: 10.1186/1687-1499-2012-225.
- [44] Y. Li and L. J. Cimini, “**Bounds on the Interchannel Interference of OFDM in Time-Varying Impairments**,” *IEEE Transactions on Communications*, vol. 49, no. 3, pp. 401–404, Mar. 2001,
-

- doi: 10.1109/26.911445.
- [45] J. H. Ni and Z. M. Liu, “**A Joint ICI Estimation and Mitigation Scheme for OFDM Systems over Fast Fading Channels,**” in *Proc. of Global Mobile Congress (GMC 2009)*, pp. 1–6, Shanghai, China, Oct. 2009, doi: 10.1109/GMC.2009.5295856.
- [46] W. G. Jeon, K. H. Chang, and Y. S. Cho, “**An Equalization Technique for Orthogonal Frequency-Division Multiplexing Systems in Time-Variant Multipath Channels,**” *IEEE Transactions on Communications*, vol. 47, no. 1, pp. 27–32, Jan. 1999, doi: 10.1109/26.747810.
- [47] Y. Mostofi and D. Cox, “**ICI Mitigation for Pilot-aided OFDM Mobile Systems,**” *IEEE Transactions on Wireless Communications*, vol. 4, no. 2, pp. 765–774, Mar. 2005, doi: 10.1109/TWC.2004.840235.
- [48] H. Hijazi and L. Ros, “**Polynomial Estimation of Time-Varying Multipath Gains with Inter-carrier Interference Mitigation in OFDM Systems,**” *IEEE Transactions on Vehicular Technology*, vol. 58, no. 1, pp. 140–151, Jan. 2009, doi: 10.1109/TVT.2008.923653.
- [49] J. C. Ikuno, S. Pendl, M. Simko, and M. Rupp, “**Accurate SINR Estimation Model for System Level Simulation of LTE Networks,**” in *Proc. of IEEE International Conference on Communications (ICC 2012)*, Ottawa, Canada, June 2012, doi: 10.1109/ICC.2012.6364098.
- [50] B. Hassibi and B. Hochwald, “**How much Training is needed in Multiple-Antenna Wireless Links?**” *IEEE Transactions on Information Theory*, vol. 49, no. 4, pp. 951–963, Apr. 2003, doi: 10.1109/TIT.2003.809594.
- [51] S. Omar, A. Ancora, and D. Slock, “**Performance Analysis of General Pilot-Aided Linear Channel Estimation in LTE OFDMA Systems with Application to Simplified MMSE Schemes,**” in *Proc. of IEEE 19th International Symposium on Personal, Indoor and Mobile Radio Communications (PIMRC 2008)*, pp. 1–6, Cannes, France, Sept. 2008, doi: 10.1109/PIMRC.2008.4699619.
- [52] M. Šimko, Q. Wang, P. S. R. Diniz, and M. Rupp, “**Inter-Carrier Interference Mitigation by Means of Precoding,**” in *Proc. of IX International symposium on Telecommunications (BIHTEL 2012)*, Sarajevo, Bosnia and Herzegovina, Nov. 2012, doi: 10.1109/BIHTEL.2012.6412070.
- [53] T. Zemen and C. Mecklenbräuker, “**Time-Variant Channel Estimation Using Discrete Prolate Spheroidal Sequences,**” *IEEE Transactions on Signal Processing*, vol. 53, no. 9, pp. 3597–3607, Sept. 2005, doi: 10.1109/TSP.2005.853104.
- [54] A. Sayeed, A. Sendonaris, and B. Aazhang, “**Multuser Detection in Fast-Fading Multipath Environments,**” *IEEE Journal on Selected Areas in Communications*, vol. 16, no. 9, pp. 1691–1701, Dec. 1998, doi: 10.1109/49.737638.
- [55] G. H. Golub and C. F. V. Loan, **Matrix Computations**, 3rd ed. Baltimore: The Johns Hopkins University Press, Oct. 1996.
- [56] A. Hedayat, A. Nosratinia, and N. Al-Dhahir, “**Linear Equalizers for Flat Rayleigh MIMO Channels,**” in *Proc. of International Conference on Acoustics, Speech, and Signal Processing (ICASSP 2005)*, Philadelphia, USA, Mar. 2005, doi: 10.1109/ICASSP.2005.1415742.
- [57] D. Gore, R. Heath Jr, and A. Paulraj, “**On Performance of the Zero Forcing Receiver in Presence of Transmit Correlation,**” in *Proc. of IEEE International Symposium on Information Theory (ISIT 2002)*, p. 159, Lausanne, Switzerland, July 2002, doi: 10.1109/ISIT.2002.1023431.
- [58] P. Li, D. Paul, R. Narasimhan, and J. Cioffi, “**On the Distribution of SINR for the MMSE MIMO Receiver and Performance Analysis,**” *IEEE Transactions on Information Theory*,

- vol. 52, no. 1, pp. 271–286, Jan. 2006, doi: 10.1109/TIT.2005.860466.
- [59] P. Suarez-Casal, J. Garcia-Naya, L. Castedo, and M. Rupp, “**KLT-Based Estimation of Rapidly Time-Varying Channels in MIMO-OFDM systems**,” in *Proc. of the 14th IEEE International Workshop on Signal Processing Advances in Wireless Communications (SPAWC 2013)*, Darmstadt, Germany, June 2013.
- [60] C. Novak and G. Matz, “**Low-Complexity MIMO-BICM Receivers with Imperfect Channel State Information: Capacity-based Performance Comparison**,” in *Proc. of IEEE 11th International Workshop on Signal Processing Advances in Wireless Communications (SPAWC 2010)*, Marrakech, Morocco, June 2010, doi: 10.1109/SPAWC.2010.5670872.
- [61] E. Alsusa, M. W. Baidas, and Y. Lee, “**On the Impact of Efficient Power Allocation in Pilot Based Channel Estimation Techniques for Multicarrier Systems**,” in *Proc. of IEEE 16th International Symposium on Personal, Indoor and Mobile Radio Communications (PIMRC 2005)*, pp. 706–710, Berlin, Germany, Sept. 2005, doi: 10.1109/PIMRC.2005.1651527.
- [62] J. Chen, Y. Tang, and S. Li, “**Pilot Power Allocation for OFDM Systems**,” in *Proc. of 57th IEEE Vehicular Technology Conference (VTC2003-Spring)*, vol. 2, pp. 1283–1287 vol.2, Seogwipo, South Korea, Apr. 2003, doi: 10.1109/VETECS.2003.1207834.
- [63] J. Wang, O. Y. Wen, H. Chen, and S. Li, “**Power Allocation between Pilot and Data Symbols for MIMO Systems with MMSE Detection under MMSE Channel Estimation**,” *EURASIP Journal on Wireless Communications and Networking*, Jan. 2011, doi: 10.1155/2011/785437.
- [64] M. Šimko and M. Rupp, “**Optimal Pilot Symbol Power Allocation in Multi-Cell Scenarios of LTE**,” in *Conference Record of the Fortyfifth Asilomar Conference on Signals, Systems and Computers*, Pacific Grove, USA, Nov. 2011.
- [65] Y. Chen, S. Zhang, and S. X. G. Li, “**Fundamental Trade-offs on Green Wireless Networks**,” *IEEE Communications Magazine*, vol. 49, no. 6, pp. 30–37, June 2011, doi: 10.1109/MCOM.2011.5783982.
- [66] D. Wu, F. Mkadem, and S. Boumaiza, “**Design of a Broadband and Highly Efficient 45W GaN Power Amplifier via Simplified Real Frequency Technique**,” in *Proc. of IEEE MTT-S International Microwave Symposium Digest (IMS 2010)*, pp. 1090–1093, Anaheim, USA, May 2010, doi: 10.1109/MWSYM.2010.5517636.
- [67] T. Quach, W. Okamura, A. Gutierrez-Aitken, T. Jenkins, E. Kaneshiro, L. Kehias, D. Sawdai, P. Watson, R. Welch, R. Worley, *et al.*, “**Ultra-efficient X-band and Linear-efficient Ka-band Power Amplifiers Using Indium Phosphide Double Heterojunction Bipolar Transistors**,” in *Proc. of IEEE International Conference On Indium Phosphide and Related Materials (IPRM 2001)*, pp. 501–504, Nara, Japan, May 2001, doi: 10.1109/ICIPRM.2001.929189.
- [68] C. Han, T. Harrold, S. Armour, I. Krikidis, S. Videv, P. Grant, H. Haas, J. Thompson, I. Ku, C. Wang, *et al.*, “**Green Radio: Radio Techniques to Enable Energy-Efficient Wireless Networks**,” *IEEE Communications Magazine*, vol. 49, no. 6, pp. 46–54, June 2011, doi: 10.1109/MCOM.2011.5783984.
- [69] Z. Niu, Y. Wu, J. Gong, and Z. Yang, “**Cell Zooming for Cost-efficient Green Cellular Networks**,” *IEEE Communications Magazine*, vol. 48, no. 11, pp. 74–79, Nov. 2010, doi: 10.1109/MCOM.2010.5621970.
- [70] ITU, “**Recommendation ITU-R M.1225: Guidelines for evaluation of radio transmission technologies for IMT- 2000 systems**,” International Telecommunication Union, Recommendation ITU-R M.1225, 1998.
- [71] S. Boyd, S. Kim, L. Vandenberghe, and A. Hassibi, “**A Tutorial on Geometric Programming**,”

- Optimization and Engineering*, vol. 8, no. 1, pp. 67–127, Apr. 2007.
- [72] I. CVX Research, “**CVX: Matlab software for disciplined convex programming, version 2.0 beta**,” <http://cvxr.com/cvx>, Sept. 2012.
- [73] M. Grant and S. Boyd, “**Graph Implementations for Nonsmooth Convex Programs**,” in *Recent Advances in Learning and Control*, ser. Lecture Notes in Control and Information Sciences, V. Blondel, S. Boyd, and H. Kimura, Eds. Springer-Verlag Limited, 2008, pp. 95–110, http://stanford.edu/~boyd/graph_dcp.html.
- [74] M. Šimko, P. S. R. Diniz, Q. Wang, and M. Rupp, “**Power Efficient Pilot Symbol Power Allocation under Time-Variant Channels**,” in *Proc. of 76th IEEE Vehicular Technology Conference (VTC2012-Fall)*, Quebec, Canada, Sept. 2011, doi: 10.1109/VTCFall.2012.6398991.
- [75] L. Tong, B. Sadler, and M. Dong, “**Pilot-Assisted Wireless Transmissions: General Model, Design Criteria, and Signal Processing**,” *IEEE Signal Processing Magazine*, vol. 21, no. 6, pp. 12–25, Nov. 2004, doi: 10.1109/MSP.2004.1359139.
- [76] R. Negi and J. Cioffi, “**Pilot Tone Selection for Channel Estimation in a Mobile OFDM System**,” *IEEE Transactions on Consumer Electronics*, vol. 44, no. 3, pp. 1122–1128, Aug. 1998, doi: 10.1109/ICCE.1998.678433.
- [77] I. Barhumi, G. Leus, and M. Moonen, “**Optimal Training Design for MIMO OFDM Systems in Mobile Wireless Channels**,” *IEEE Transactions on Signal Processing*, vol. 51, no. 6, pp. 1615–1624, June 2003, doi: 10.1109/TSP.2003.811243.
- [78] J. Choi and Y. Lee, “**Optimum Pilot Pattern for Channel Estimation in OFDM Systems**,” *IEEE Transactions on Wireless Communications*, vol. 4, no. 5, pp. 2083–2088, Sept. 2005, doi: 10.1109/TWC.2005.853891.
- [79] S. Adireddy, L. Tong, and H. Viswanathan, “**Optimal Placement of Training for Frequency-Selective Block-Fading Channels**,” *IEEE Transactions on Information Theory*, vol. 48, no. 8, pp. 2338–2353, Aug. 2002, doi: 10.1109/TIT.2002.800466.
- [80] W. Zhang, X. Xia, and P. Ching, “**Optimal Training and Pilot Pattern Design for OFDM Systems in Rayleigh Fading**,” *IEEE Transactions on Broadcasting*, vol. 52, no. 4, pp. 505–514, Dec. 2006, doi: 10.1109/TBC.2006.884001.
- [81] X. Cai and G. Giannakis, “**Error Probability Minimizing Pilots for OFDM with M-PSK Modulation over Rayleigh-Fading Channels**,” *IEEE Transactions on Vehicular Technology*, vol. 53, no. 1, pp. 146–155, Jan. 2004, doi: 10.1109/TVT.2003.819624.
- [82] O. Simeone and U. Spagnolini, “**Adaptive Pilot Pattern for OFDM Systems**,” in *Proc. of IEEE International Conference on Communications (ICC 2004)*, vol. 2, pp. 978–982, Paris, France, June 2004, doi: 10.1109/ICC.2004.1312647.
- [83] C.-H. Kim and Y.-H. Lee, “**Adaptive Pilot Signaling in the Uplink of OFDM-Based Wireless Systems**,” in *Proc. of 16th IST Mobile and Wireless Communications Summit (ISTMWC 2007)*, pp. 1–5, Budapest, Hungary, July 2007, doi: 10.1109/ISTMWC.2007.4299160.
- [84] J.-C. Guey and A. Osseiran, “**Adaptive Pilot Allocation in Downlink OFDM**,” in *Proc. of Wireless Communications and Networking Conference (WCNC 2008)*, pp. 840–845, Las Vegas, USA, Apr. 2008, doi: 10.1109/WCNC.2008.154.
- [85] P. Han, J. Wang, and P. Xu, “**Adaptive Pilot Design Based on Doppler Frequency Shift Estimation for OFDM System**,” in *Proc. of International Conference on Computer Design and Applications (ICCCA 2010)*, pp. V4–533–V4–536, Qinhuangdao, China, June 2010, doi: 10.1109/ICCCA.2010.5540707.

-
- [86] M. Šimko, P. S. R. Diniz, Q. Wang, and M. Rupp, “**New Insights in Optimal Pilot Symbol Patterns for OFDM Systems**,” in *Proc. of IEEE Wireless Communication and Networking Conference (WCNC 2013)*, Shanghai, China, Apr. 2013.
- [87] M. Šimko, Q. Wang, and M. Rupp, “**Optimal Pilot Pattern for Time Variant Channels**,” in *Proc. of IEEE International Conference on Communications (ICC 2013)*, Budapest, Hungary, June 2013.
- [88] C. Mehlführer, S. Caban, and M. Rupp, “**Cellular System Physical Layer Throughput: how far off are we from the Shannon bound?**” *IEEE Wireless Communications*, vol. 18, no. 6, pp. 54–63, Dec. 2011, doi: 10.1109/MWC.2011.6108334.
- [89] S. Schwarz, M. Šimko, and M. Rupp, “**On performance bounds for MIMO OFDM based wireless communication systems**,” in *Proceedings of IEEE Signal Processing Advances in Wireless Communications*, San Francisco, CA, June 2011.
- [90] M. Rupp, J. Garcia-Naya, C. Mehlführer, S. Caban, and L. Castedo, “**On Mutual Information and Capacity in Frequency Selective Wireless Channels**,” in *Proc. of IEEE International Conference on Communications (ICC 2010)*, Cape Town, South Africa, May 2010, doi: 10.1109/ICC.2010.5501942.
- [91] A. Forenza, M. McKay, A. Pandharipande, R. Heath, and I. Collings, “**Adaptive MIMO Transmission for Exploiting the Capacity of Spatially Correlated Channels**,” *IEEE Transactions on Vehicular Technology*, vol. 56, no. 2, pp. 619–630, Mar. 2007, doi: 10.1109/TVT.2007.891427.
- [92] S. Loyka and A. Kouki, “**New Compound Upper Bound on MIMO Channel Capacity**,” *IEEE Communications Letters*, vol. 6, no. 3, pp. 96–98, Mar. 2002, doi: 10.1109/4234.991144.
- [93] K. Hassan, T. Rahman, M. Kamarudin, and F. Nor, “**The Mathematical Relationship Between Maximum Access Delay and the RMS Delay Spread**,” in *Proc. of 7th International Conference on Wireless and Mobile Communications (ICWMC 2011)*, pp. 18–23, Luxembourg, June 2011.
- [94] M. Šimko, P. S. R. Diniz, Q. Wang, and M. Rupp, “**Adaptive Pilot-Symbol Patterns for MIMO OFDM Systems**,” *IEEE Transactions of Wireless Communications*, 2012, submitted.
- [95] M. Šimko, P. S. R. Diniz, and M. Rupp, “**Design Requirements of Adaptive Pilot-Symbol Patterns**,” in *Proc. of ICC Workshop: Beyond LTE-A*, Budapest, Hungary, June 2013.
- [96] S. Schwarz, C. Mehlführer, and M. Rupp, “**Calculation of the Spatial Preprocessing and Link Adaption Feedback for 3GPP UMTS/LTE**,” in *Proceedings of the 2010 6th Conference on Wireless Advanced (WiAD2010): London, UK; June, 2010*, doi: 10.1109/WIAD.2010.5544947.